Development of Highly Active and Reusable Niobium-Based Complex Oxide Catalysts for the Dehydration of Biomass-Derived Sugars

(バイオマス由来糖類の脱水反応に高活性かつ再利用可能な二オブ系複合酸化物触媒の開発)

Zijian Wang

Hokkaido University

北海道大学

2025

Table of Content

Chapter 1: Introduction

1.1 Research Background

The rapid growth in global energy demand has posed significant challenges to current energy supply and usage patterns. Fossil fuels, as traditional primary energy sources, have been instrumental in supporting industrialization, transportation, and daily life. However, the environmental issues associated with fossil fuels are increasingly evident.[1] To address the energy crisis and environmental degradation, new energy sources are increasingly valued as alternatives to fossil fuels. According to the International Energy Agency (IEA), the installed capacity of clean energy sources such as solar, wind, hydro, geothermal, and hydrogen has been steadily increasing, now comprising over 30% of the global energy mix.[2] Among these, biomass energy stands out as a renewable source with significant advantages in achieving carbon neutrality and reducing carbon footprints.[3–5] Biomass resources, including forestry and agricultural biomass as potential feedstocks for bioenergy,[6,7] absorbs CO_2 through photosynthesis during growth and releases the same amount during combustion or conversion, thereby maintaining a dynamic carbon balance. This unique carbon cycling characteristic plays a crucial role in combating climate change and reducing greenhouse gas emissions. Furthermore, biomass energy sources are highly diversified, including agricultural residues, forestry waste, and urban organic waste, ensuring the availability of suitable raw materials globally and promoting localized energy development and utilization (**Figure 1.1**).[5,8–10]

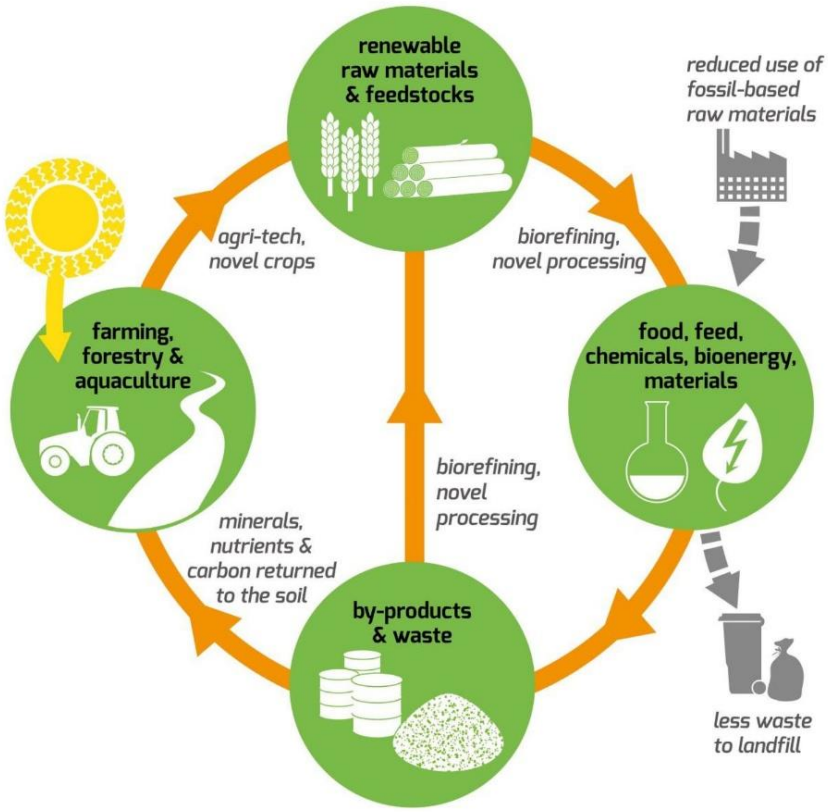

Figure 1.1. The schematic map of biomass resources recycling.[5]

1.2 Biomass-derived furfural and its applications

Biomass is an organic material capable of converting solar energy into chemical energy through photosynthesis, making it one of the most abundant renewable resources on Earth. It refers to organic material derived from living or recently living organisms, primarily plants and animals. In the context of energy and chemical production, biomass typically means plant-based materials that can be used as fuel or raw material for producing bio-based products.[5,8–10] Lignocellulosic biomass, especially as a renewable energy source, consists of various organic components, with the three primary constituents: cellulose, hemicellulose, and lignin. As shown in **Figure 1.2**, hemicellulose provides the main C5 sugar backbone for furfural.[11–13] These components collectively

form the fundamental structure of plant cell walls, accounting for the majority of plant dry weight, with cellulose, hemicellulose, and lignin comprising approximately 40–50%, 25–35%, and 15–20%, respectively.[12,13] The distinct chemical properties and application potentials of cellulose, hemicellulose, and lignin during biomass conversion are of significant importance for developing and utilizing energy and materials.[14,15]

Cellulose is the most abundant polysaccharide in biomass, characterized by a molecular structure of D-glucose units linked by β-1,4-glycosidic bonds, which confer high crystallinity and stability (**Figure 1.2**).[11–13] Cellulose can be degraded into glucose through enzymatic or acid hydrolysis, which can be further utilized to produce ethanol, organic acids, and other high-value-added chemicals. Additionally, cellulose can be mechanically and chemically modified to produce functional materials such as cellulose nanocrystals and cellulose fibers, which are used to manufacture textiles, composites, and biomedical materials.[12–16] Lignin, a high-molecular-weight aromatic compound, is composed of phenylpropane units irregularly linked by ether and carbon-carbon bonds, making it the most recalcitrant component in biomass. Lignin can undergo pyrolysis or oxidative cleavage to produce various aromatic compounds, including phenol, vanillin, and benzaldehyde, which have significant potential in the production of aromatic chemicals, plasticizers, antioxidants, and other high-value-added products.[17–21] Hemicellulose is a complex polysaccharide composed of various monosaccharides such as xylose, arabinose, galactose, glucose, and mannose, and it possesses a lower degree of polymerization and crystallinity compared to cellulose. Hemicellulose can be hydrolyzed into five-carbon and six-carbon sugars, which are utilized in the production of compounds such as furfural, xylitol, and arabinitol.[16,18–25] Xylose is obtained by acid hydrolysis using dilute acids (e.g., sulfuric acid) or enzymatic hydrolysis.[12] Acid hydrolysis is fast

and widely used industrially but has issues including equipment corrosion, waste generation, and side reactions reducing xylose yields (e.g., furfural formation). Enzymatic hydrolysis is more selective and environmentally friendly, but it's slower, costlier due to enzyme prices, and sensitive to reaction conditions.[23,24] These derivatives hold extensive application value in the food, pharmaceutical, and chemical industries.

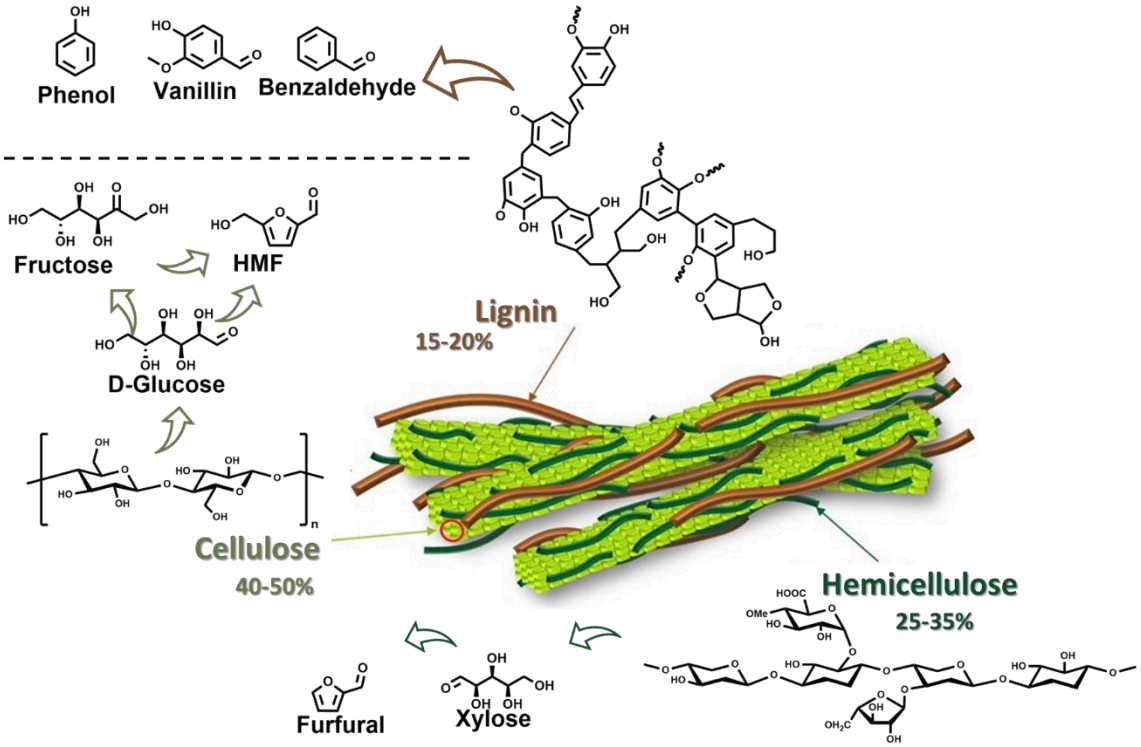

Figure 1.2. Chemical structure of lignocellulose and its distribution in plants.[11–13]

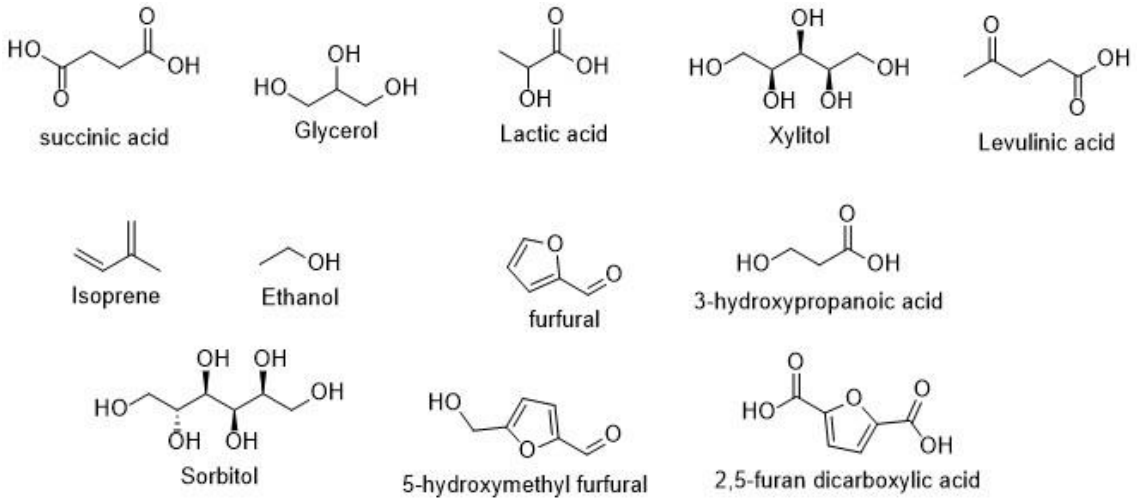

Figure 1.3. 12 top-value platform chemicals from biomass upgrading.

The U.S. Department of Energy (DoE) has identified twelve high-value-added chemicals derived from biomass as fundamental platform molecules. These include ethanol, glycerol, lactic acid, 3-hydroxypropionic acid, succinic acid, furfural, acetylpropionic acid, xylitol, isoprene, 2,5-furandicarboxylic acid, 5-hydroxymethylfurfural, and sorbitol (**Figure 1.3**).[18,26,27] Among the various conversion pathways of biomass components, the production and utilization of furfural have attracted widespread research interest. Furfural is a five-carbon heterocyclic compound produced from xylose, the main component of hemicellulose, through acid-catalyzed dehydration reactions, making it one of the most important primary platform molecules in biomass conversion processes. Due to its unique chemical structure and high reactivity, furfural is considered a key platform molecule for renewable chemicals.[28–30] The furfural molecule contains an aldehyde group and a furan ring, which together confer high reactivity in various organic reactions. These functional groups enable its participation in hydrogenation, condensation, oxidation, amination, and other reaction pathways, leading to the production of a wide range of high-value-added derivatives, including 2-methylfuran, 2-methyltetrahydrofuran, furan dicarboxylic acid, furanoic acid, and

tetrahydrofuranol. These furfural derivatives have extensive application potential in fuel additives, plastic precursors, solvents, pharmaceutical synthesis, and the preparation of high-performance materials. The following **Figure 1.4** summarizes the main applications of furfural.[31,32]

In summary, furfural, as a core platform molecule in biomass refining, plays a critical role in promoting the sustainable development of biomass energy and chemicals through its efficient production and in-depth utilization. The high-value utilization of furfural and its derivatives not only enhances the economic benefits of biomass resources but also provides new ideas and strategies for biomass conversion processes, playing a key role in the circular utilization of renewable resources and the achievement of carbon neutrality goals.

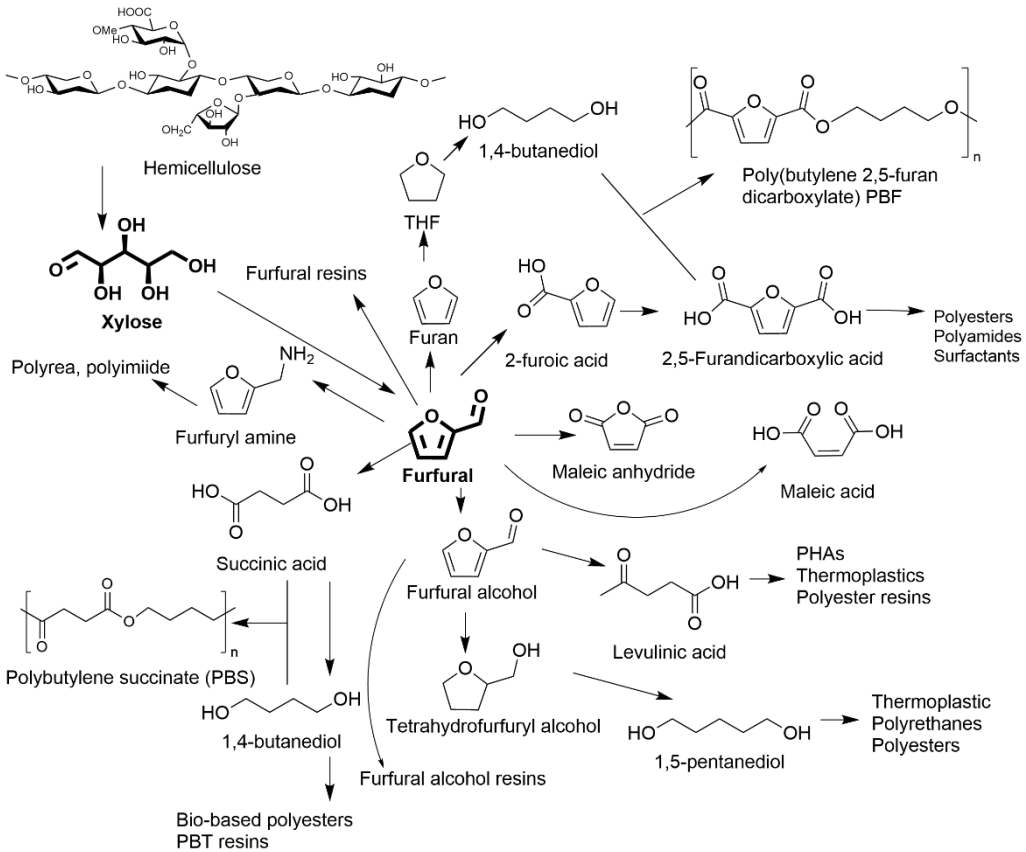

Figure 1.4. Production pathway of furfural derivatives from furfural as a platform molecule.[31,32]

1.3 Catalytic strategies for furfural production

1.3.1 An overview of the furfural production process

Furfural is primarily derived from the conversion of pentose sugars extracted from hemicellulose. Currently, two major approaches exist for furfural production: enzymatic hydrolysis and chemical methods.[33–36] The enzymatic route has attracted considerable attention due to its high selectivity, environmental friendliness, mild reaction conditions, low energy consumption, and adaptability to a wide range of feedstocks. Xylanases are considered the key enzymes for hemicellulose hydrolysis, often requiring synergistic action from multiple enzymes such as endoxylanases and β-xylosidases in specific ratios to efficiently produce xylose.[37,38] However, large-scale furfural production via enzymatic methods remains unfeasible due to high costs, low efficiency, challenges in scale-up, and the inherent toxicity of furfural to microorganisms, which prevents a fully biocatalytic process. A more practical strategy involves enzymatic hydrolysis for xylose release, followed by chemical dehydration to furfural, offering a green, efficient, and controllable conversion pathway.[39–42]

At present, the only approach capable of industrial-scale furfural production is the chemical method, which proceeds via two sequential stages. First, hemicellulose is hydrolyzed to xylose under acidic conditions. Then, the generated xylose undergoes dehydration to furfural, also catalyzed by acids. Brønsted acids directly convert xylose into furfural, while Lewis acids facilitate the isomerization of xylose to xylulose, which is subsequently dehydrated by Brønsted acids. The presence of Lewis acids significantly accelerates the conversion of xylose, whereas Brønsted acids tend to enhance furfural yield.[43–45] On the other hand, xylose can be directly dehydrated on the surface of Lewis

acid sites without prior isomerization to the ketose xylulose. Through the stepwise removal of water molecules, xylose forms key intermediates—such as α-dicarbonyl species—which ultimately lead to the formation of furfural (**Figure 1.5**).[46]

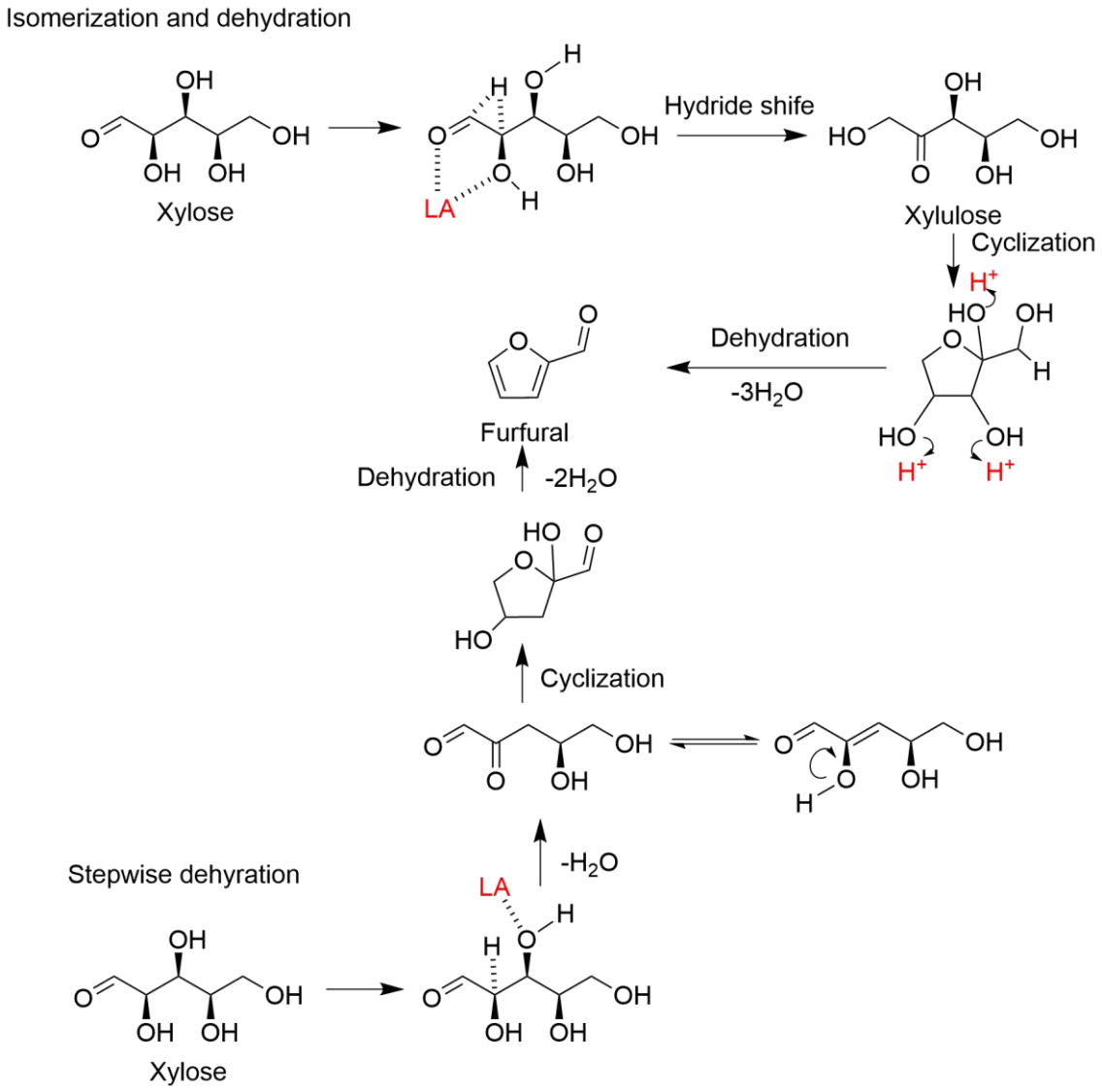

Figure 1.5. Reaction mechanism of furfural production from xylose by isomerization and stepwise dehydration.[46]

From a process engineering perspective, furfural production methods are classified into one-step and two-step processes. In the one-pot process, both xylan hydrolysis and xylose dehydration are conducted simultaneously in a single reactor. In contrast, the two-step process separates these reactions, optimizing each under different temperatures, durations, or even distinct reactors.[47] For example, Li et al. investigated a two-step process using corn stover in a water/γ-valerolactone (GVL) system: levulinic acid was produced at 190 °C in the first step, and furfural was generated at 140 °C in the second step, with yields of 57.7% and 70.7%, respectively.[48] Although modified one-step processes (e.g., steam-assisted catalysis coupled with online distillation) are still prevalent in industry, the two-step method is gaining attention in research and emerging technologies due to its high yield, improved selectivity, and better control over by-products—making it a promising core pathway for green and efficient furfural synthesis.[49,50]

Despite the long history of furfural industrialization, several critical issues remain. First, furfural is prone to side reactions under acidic and high-temperature conditions, including resinification, condensation, and cracking, which significantly reduce yields. This is particularly problematic in one-step processes, where furfural must be promptly removed to avoid degradation.[34] Second, energy consumption and process integration remain major challenges.[51,52] Traditional batch processes (e.g., the Quaker Oats method) require heating to 160 °C for several hours, resulting in high steam and condensation loads.[49,53] Complex separation steps such as distillation and extraction further increase energy demands. Although continuous-flow and online extraction systems (e.g., MTC, Suprayield) have been proposed, most are still at laboratory or pilot scales, limited by process scale-up difficulties and equipment complexity.[54,55]

Additionally, variability in raw material composition and incomplete biomass utilization remain pressing concerns. Catalyst-related issues also persist, particularly the use of mineral acids, which are corrosive, non-recyclable, and environmentally unfriendly. Common acids like H_2SO_4 and H_3PO_4 shorten equipment lifespan and generate acidic waste streams.[49,56,57] Although organic acids (e.g., formic, acetic acid) and solid acids (e.g., sulfonated carbon materials, metal oxides) are more environmentally benign, they generally lack the activity and stability compared to traditional mineral acids.[58] The following section will focus on recent advances in catalyst design and optimization for furfural production.

1.3.2 Innovation of acid catalysts

1.3.2.1 Homogeneous catalysts

Furfural production primarily relies on xylose derived from hemicellulose, which undergoes acid-catalyzed dehydration. Efficient catalysts can significantly lower the activation energy barrier and enhance reaction selectivity, thereby suppressing side reactions.[50] Historically, and still in most industrial applications, homogeneous catalysts—particularly mineral acids such as HCl, H_2SO_4, and H_3PO_4—have been widely used. Among them, HCl exhibits higher catalytic activity than H_2SO_4, and H_3PO_4 due to the Cl^- anion promoting the formation of 1,2-enediol intermediates, achieving yields of 38% from xylose and 34% from xylan.[59,60] H_2SO_4, under microwave-assisted conditions, can achieve up to 64% yield from xylose but tends to generate undesirable side reactions, including sulfonation and polymerization byproducts.[61]

Other homogeneous catalysts include organic acids and metal salts. For example, formic acid can achieve a maximum furfural yield of 74% with 78% selectivity under conditions of 180 °C, using 40 g/L xylose and 10 g/L formic acid.[33] Notably, formic acid can also be generated in situ during the reaction, reducing the need for additional feedstock and enhancing process sustainability. However, it generally requires higher concentrations or co-catalysts, and the reaction rate tends to be slower. Commonly used metal salts are mainly Lewis acids, such as $AlCl_3$, $FeCl_3$, and $CrCl_3$. These catalysts facilitate the isomerization of xylose to xylulose, a key intermediate in furfural formation. However, achieving high furfural yields typically requires the synergistic presence of Brønsted acids alongside Lewis acids.[43,61–64]

1.3.2.2 Heterogenous catalysts

Current research efforts are focused on developing catalytic systems that exhibit high selectivity, low energy consumption, and environmental sustainability. In addition, catalysts should possess properties such as reusability and ease of separation. As a result, heterogeneous catalysts have become the mainstream direction for furfural production and a core focus of future green catalysis.

Early investigations of heterogeneous catalysts were largely confined to the laboratory scale, involving carbon materials, natural minerals, and unmodified metal oxides (e.g., Al_2O_3, ZrO_2). However, these catalysts exhibited limited activity and selectivity.[50] Subsequently, the development of functional solid acid catalysts gained traction. For instance, Amberlyst 70, as reported by Agirrezabal-Telleria et al. (2011), achieved a furfural yield of 70% when combined with nitrogen (N_2) distillation, demonstrating enhanced performance after removal from an acidic medium.[65]

Amberlyst 15, when used in conjunction with the basic solid catalyst hydrotalcite (HT), enabled the conversion of a mixture of arabinose, rhamnose, and lactose, yielding 29–33% furfural.[66]

A common limitation of cheap heterogeneous catalysts, Amberlyst 70 for instance, is the occurrence of side reactions during reactions, which necessitates integration with flow systems to minimize polymerization.[65] Around 2010, zeolite-based catalysts such as H-ZSM-5, H-BEA, and H-Mordenite gained popularity due to their recyclability and catalytic stability. H-ZSM-5, for example, achieved a 46% furfural yield from xylose in aqueous phase at 200 °C, as reported by O'Neill et al., although issues such as pore blockage and catalytic deactivation were observed.[67] Similarly, H-Beta, HUSY, and H-MOR were employed by Dhepe and Sahu to directly convert hemicellulose into xylose and furfural, but furfural yields remained low (12–18%) due to competing side reactions arising from simultaneous hydrolysis and dehydration steps.[68]

Recent advances have also focused on modifying the surface electronic structure and acidity of metal oxides by introducing heteroatoms or functional groups, aiming to enhance acid-site distribution and catalytic pathway selectivity. For example, Chareonlimkun et al. utilized ZrO_2–TiO_2 composites for furfural production from corn cobs under subcritical water conditions, achieving a yield of 10.3%.[70] Shi et al. developed an ordered mesoporous SO_4^{2-}/ZrO_2–Al_2O_3/SBA-15 catalyst for aqueous-phase furfural synthesis. With increasing ZrO_2 content, both xylose conversion and furfural selectivity improved at 160 °C. The SO_4^{2-}/12% ZrO_2–Al_2O_3/SBA-15 catalyst exhibited the best performance, with 98.7% xylose conversion and 53.4% furfural selectivity, attributed to the increased number of acid sites introduced by ZrO_2.[71] **Table 1.1** summarizes representative catalysts reported in the literature review.

More research has shifted toward synergistic acid catalysis and structural regulation, particularly focusing on Lewis–Brønsted acid cooperative mechanisms. Among various materials, metal oxides have demonstrated considerable advantages, particularly due to their physical stability under high-temperature aqueous conditions, making them promising heterogeneous catalysts for furfural production.[46] Among the catalysts, Nb_2O_5 exhibited relatively high catalytic activity. García-Sancho et al. reported furfural yields exceeding 50% and xylose conversions over 90% using mesoporous Nb_2O_5 in a water–toluene biphasic system (170 °C, 90 min).[69] In contrast, homogeneous catalysts such as HCl, H_2SO_4, and $Sc(OTf)_3$ showed limited furfural yields under high-temperature aqueous conditions (180 °C), typically ranging from 20% to 40%.[46][59] Similarly, solid catalysts such as H-ZSM-5 and TiO_2 achieved furfural yields of only around 45% even at temperatures above 200 °C.[67][70] Gupta et al. compared multiple catalysts and found that Nb_2O_5 offered the lowest activation energy (83 kJ/mol) and the highest furfural selectivity (72%) under biphasic reaction conditions at 120 °C, an increase of 24% in furfural yield compared to the pure aqueous phase. While maintaining stable performance over four consecutive cycles.[46] **Table 1.2** presents selected catalysts that have been commonly reported in these studies.

Nonetheless, challenges remain. Metal oxides are prone to deactivation in aqueous media, especially under prolonged high-temperature conditions. In particular, the calcination temperature of Nb_2O_5 significantly affects its crystalline phase and thus its acidity. Furthermore, the synthesis of mixed metal oxides can be complex, and certain dopants, such as chromium, raise toxicity concerns.[72] Additionally, the use of microwave, ultrasound, and continuous-flow reactors has improved process efficiency. Controlling the distribution of active site and the structure of the catalyst remains a central theme,

particularly for addressing issues such as catalyst deactivation, regeneration efficiency, and long-term stability.[73–77]

Table 1.1. Summary of representative homogeneous and heterogeneous catalysts for furfural production.

Catalyst	Type	Pros and Cons	Ref.
HCl	Homogenous	High activity and low cost, but highly corrosive, polluting, low selectivity	[65]
Formic acid	Homogenous	Mild, renewable, greener, but activity depends on system compatibility	[76]
$CrCl_3$, $AlCl_3$	Homogenous	Effective synergy, but non-recyclable and system complexity	[43][63]
Amberlyst 15	Heterogeneous	Recyclable, flow-compatible, but unstable in hot aqueous media	[66]
H-ZSM-5	Heterogeneous	Thermally stable, but narrow pores may trap by-products	[67]
SO_4^{2-}/ZrO_2–TiO_2	Heterogeneous	Acid tuning flexibility, water-phase compatible; complex preparation	[70]
SBA-15–SO_3H	Heterogeneous	Excellent selectivity, tunable pores; relatively expensive synthesis	[71]
Nb_2O_5	Heterogeneous	High stability, low activation energy, and good selectivity, but requires structural optimization for broader efficiency	[46][69]

Table 1.2. Literature survey for different types of acid catalysts from xylose to furfural

Catalyst	Type	Solvent	Temp / °C	Furfural yield (%)	Ref.
HCl	Brønsted	H_2O	180	38	[46]
H_2SO_4	Brønsted	H_2O	180	33	[46]
$Sc(OTf)_3$	Lewis	H_2O	120	18	[59]
H-ZSM-5	Brønsted	H_2O	200	46	[67]
TiO_2	Lewis	H_2O	250	32	[70]
Amorphous Nb_2O_5	Main Lewis	H_2O	120	48	[59]
Amorphous Nb_2O_5	Main Lewis	H_2O/Toluene	120	72	[59]

1.3.2.3 Complex metal oxide catalysts

Complex metal oxides exhibit superior acidity regulation, thermal stability, and catalytic activity compared to single-component metal oxides due to the synergistic interactions among multiple metal species. These properties are particularly advantageous for furfural production, where fine-tuning of acid types and structural optimization are essential. Li et al. developed a multicomponent perovskite-type catalyst, Cr-$LaCo_{0.8}Cu_{0.2}O_3$, for the catalytic dehydration of xylan to furfural.[78] In this system, partial substitution of Co^{3+} with Cu^{2+} enhances electronic conductivity, while the introduction of Cr^{3+} as a secondary metal ion provides additional Lewis acidity. This combination facilitates strong metal–oxygen interactions on the catalyst surface, improving the adsorption and activation of substrate molecules. Dong et al. designed a bifunctional Zn–Sn–Beta zeolite catalyst via solid-state ion exchange, embedding Lewis acidic Sn^{4+} and weakly basic Zn^{2+} sites into the Beta framework. Sn^{4+} promotes sugar isomerization, while Zn^{2+} suppresses undesired side reactions.[79]

Furthermore, studies by Noma et al. and Li et al. revealed that Lewis acid–base interactions play a critical role in optimizing sugar conversion.[80,81] Lewis acids, such as Ti^{4+}, can coordinate with hydroxyl groups on glucose, particularly the C3–OH group, thereby facilitating molecular activation, which is shown in **Figure 1.6**. The high Lewis acidity of under-coordinated Ti^{4+} sites is closely related to defect structures. In contrast, Lewis bases assist in proton transfer and intermediate stabilization. Bridging oxygen atoms (Ob) or Ti–OH groups located near Lewis acid sites can act as proton acceptors or facilitate proton migration, which is crucial during the formation of intermediates such as 3-deoxyglucosone (3DG). Phosphate modification stabilizes surface TiO_4 Lewis acid configurations, preventing undesired side reactions.[80] This concept has inspired further

exploration into Lewis acid–base cooperative mechanisms within complex metal oxide systems.

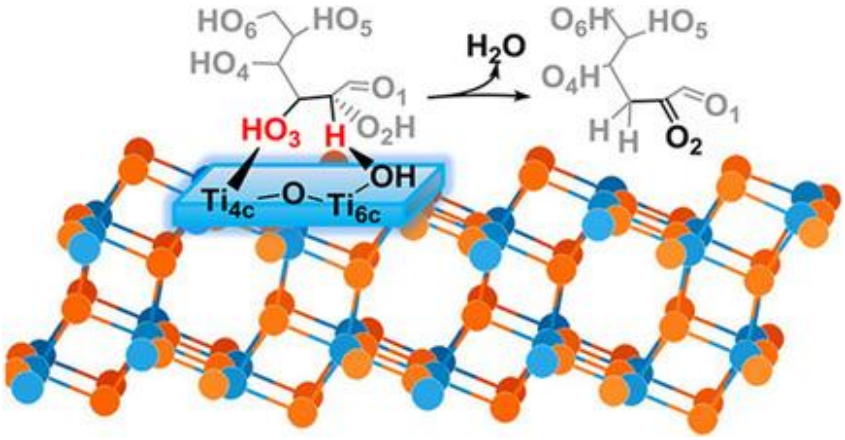

Figure 1.6. Proposed reaction mechanism of glucose dehydration over the TiO_2 surface.[81]

Nb_2O_5, as an acidic metal oxide, exhibits excellent catalytic performance for sugar conversion, particularly in its amorphous state, as discussed in **Section 1.3.2.2**. However, a key limitation of amorphous Nb_2O_5 is its poor structural stability. During the regeneration stage after reactions, high-temperature calcination often induces crystallization and structural reconstruction. For instance, Nb_2O_5 can be synthesized at low temperatures (<400 °C). Other typical crystalline phases include the TT-phase (pseudohexagonal) at 500 °C, the T-phase (orthorhombic) at 700 °C, the M-phase (tetragonal) or B-phase (monoclinic) at 800–1000 °C, and the H-phase (monoclinic) at 1100 °C.[82–85] Among these, the H-phase is the most thermodynamically stable; however, due to its high degree of crystallinity, it contains almost no defects and exhibits negligible acidic catalytic activity. To address the stability issues of amorphous Nb_2O_5, the synthesis of structurally stable niobium-based crystalline complex metal oxides has proven to be an effective strategy. Compared with pristine crystalline Nb_2O_5, modifying the local chemical environment (i.e., M–O–Nb linkages) alters the surface electronic structure and

active site density, thereby enhancing the catalytic performance for sugar conversion. Notably, Kim et al. reported acid-base catalysis of the crystalline $YNbO_4$ catalyst in sugar activation.[86] In **Figure 1.7(A)**, LAS (Lewis acid sites) (Nb) activate hydroxyl groups such as C3–OH and C1–OH of fructose to form carbocation intermediates or stabilized transition states, while LBS (Lewis base sites) (O^{2-}) provide lone-pair electrons to accept protons and facilitate water elimination. Crystalline $YNbO_4$ formed tetragonal phase after calcination at 700 °C (**Figure 1.7(B)**) and a monoclinic phase after calcination at 1000 °C (**Figure 1.7(C)**). Upon crystallization, $YNbO_4$ no longer exhibits the highly amount of acid–base active sites typically found in the amorphous state. Instead, it develops an ordered and stable metal–oxygen framework, which enhances its thermal stability and reusability. These properties make it particularly suitable for high-temperature reactions or post-treatment processes such as calcination for carbon removal. Padovan et al. showed that phosphate modification enhances the stability of Lewis acid sites while deactivating basic sites.[87] This suppresses undesired side reactions in glucose conversion, such as humin formation, and improves HMF selectivity. These findings underscore the importance of acid–base regulation in guiding reaction pathways and provide a theoretical basis for the design of multifunctional complex metal oxide catalysts.

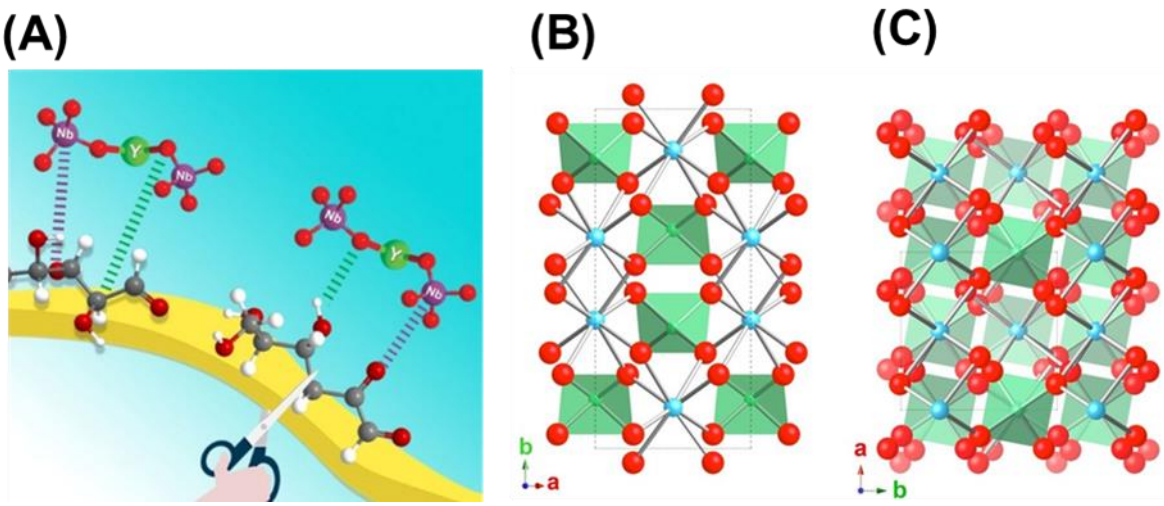

Figure 1.7. Schematic illustration of $YNbO_4$ interacting with sugar molecules via Lewis acidic Nb and Lewis basic O centers (A), and crystal structure models of tetragonal (B) and monoclinic $YNbO_4$(C).[86]

1.4 Thesis overview

While most studies focus on amorphous or low-crystallinity metal oxides, recent findings suggest that the crystalline phase and its atomic-level structure have profound impacts on high acidity, water tolerance, and catalytic selectivity. However, controlling acidity in T-phase niobium oxide remains challenging due to its inherently low surface reactivity. This thesis explores the problem of low acidity in T-phase niobium oxide formed from calcined amorphous niobium oxide, which diminishes catalytic efficiency in the conversion of xylose to furfural. Prior research has demonstrated that introducing the transition metal yttrium into crystalline niobium oxide, followed by phosphoric acid treatment, enhances the acidity and boosts catalytic activity for converting glucose to 5-hydroxymethylfurfural (HMF). Building upon these findings, the current study focuses on modifying crystalline niobium oxide with different elements. Alkaline earth metals and phosphates are incorporated into crystalline niobium oxide using the Amorphous Metal Complex (AMC) method to synthesize Nb-based complex metal oxides and

phosphate metal oxides. A range of characterization techniques are utilized to thoroughly examine the structures and active sites of the modified crystalline niobium oxides, and the catalytic mechanisms are analyzed. Synthesizing with alkaline earth metals and phosphates leads to different site modifications

In **Chapter 2**, the physical properties and active sites of $CaNb_2O_6$, which incorporates calcium as a secondary element, are analyzed. Through various characterizations and experiments on the conversion of xylose to furfural in a biphasic reaction system, the roles of calcium and the effects of phosphate treatment are examined and summarized. A comprehensive comparative analysis is conducted with Nb_2O_5 and P-Nb_2O_5 to assess the scientific significance.

Chapter 3 extends the research to other alkaline earth metals, magnesium, strontium, and barium, into crystalline niobium oxide. By employing various characterization methods and conducting experiments on the conversion of xylose to furfural in a biphasic reaction system, the physical properties and active sites of all the complex metal oxide catalysts are summarized. The experimental results are used to deduce the systematic changes resulting from different alkaline earth metals into crystalline niobium oxide, and the underlying scientific principles are analyzed.

Chapter 4 presents a comprehensive summary of the thesis's content and envisions the potential research value to be explored, laying the groundwork for future studies.

1.5 References

[1] R. Hannah, R. Pablo, *OurWorldinData.org, https://ourworldindata.org/fossil-fuels* **2017**.

[2] IEA (2024), *Clean Energy Transitions Programme 2023*, Paris, **2024**.

[3] J. E. Bell, C. L. Brown, K. Conlon, S. Herring, K. E. Kunkel, J. Lawrimore, G. Luber, C. Schreck, A. Smith, C. Uejio, *Journal of the Air & Waste Management Association* **2018**, *68*, 265–287.

[4] P. Achakulwisut, P. Erickson, C. Guivarch, R. Schaeffer, E. Brutschin, S. Pye, *Nat Commun* **2023**, *14*, 5425.

[5] A. Tursi, *Biofuel Res. J.* **2019**, *6*, 962–979.

[6] M. Hoogwijk, A. Faaij, R. Van Den Broek, G. Berndes, D. Gielen, W. Turkenburg, *Biomass and Bioenergy* **2003**, *25*, 119–133.

[7] H. Haberl, T. Beringer, S. C. Bhattacharya, K.-H. Erb, M. Hoogwijk, *Current Opinion in Environmental Sustainability* **2010**, *2*, 394–403.

[8] S. V. Vassilev, D. Baxter, L. K. Andersen, C. G. Vassileva, *Fuel* **2010**, *89*, 913–933.

[9] C. Field, J. Campbell, D. Lobell, *Trends in Ecology & Evolution* **2008**, *23*, 65–72.

[10] Y. Pan, R. A. Birdsey, O. L. Phillips, R. B. Jackson, *Annu. Rev. Ecol. Evol. Syst.* **2013**, *44*, 593–622.

[11] C. U. Jensen, J. K. Rodriguez Guerrero, S. Karatzos, G. Olofsson, S. B. Iversen, *Biomass Conv. Bioref.* **2017**, *7*, 495–509.

[12] V. Pasangulapati, K. D. Ramachandriya, A. Kumar, M. R. Wilkins, C. L. Jones, R. L. Huhnke, *Bioresource Technology* **2012**, *114*, 663–669.

[13] P. Giudicianni, G. Cardone, R. Ragucci, *Journal of Analytical and Applied Pyrolysis* **2013**, *100*, 213–222.

[14] S. D. Stefanidis, K. G. Kalogiannis, E. F. Iliopoulou, C. M. Michailof, P. A. Pilavachi, A. A. Lappas, *Journal of Analytical and Applied Pyrolysis* **2014**, *105*, 143–150.

[15] D. Chen, A. Gao, K. Cen, J. Zhang, X. Cao, Z. Ma, *Energy Conversion and Management* **2018**, *169*, 228–237.

[16] Z. Ma, Y. Yang, Y. Wu, J. Xu, H. Peng, X. Liu, W. Zhang, S. Wang, *Journal of Analytical and Applied Pyrolysis* **2019**, *140*, 195–204.

[17] A. M. Abdel-Hamid, J. O. Solbiati, I. K. O. Cann, in *Advances in Applied Microbiology*, Elsevier, **2013**, pp. 1–28.

[18] M. Al-Naji, F. Brandi, M. Drieß, F. Rosowski, *Chemie Ingenieur Technik* **2022**, *94*, 1611–1627.

[19] S.-J. Jung, S.-H. Kim, I.-M. Chung, *Biomass and Bioenergy* **2015**, *83*, 322–327.

[20] W. Cao, J. Li, T. Martí-Rosselló, X. Zhang, *Journal of the Energy Institute* **2019**, *92*, 1303–1312.

[21] G. Dorez, L. Ferry, R. Sonnier, A. Taguet, J.-M. Lopez-Cuesta, *Journal of Analytical and Applied Pyrolysis* **2014**, *107*, 323–331.

[22] P. Gallezot, *Chem. Soc. Rev.* **2012**, *41*, 1538–1558.

[23] H. Yang, R. Yan, H. Chen, D. H. Lee, C. Zheng, *Fuel* **2007**, *86*, 1781–1788.

[24] P. Zong, Y. Jiang, Y. Tian, J. Li, M. Yuan, Y. Ji, M. Chen, D. Li, Y. Qiao, *Energy Conversion and Management* **2020**, *216*, 112777.

[25] D. Díez, A. Urueña, R. Piñero, A. Barrio, T. Tamminen, *Processes* **2020**, *8*, 1048.

[26] P. R.D., S. B.J., *U.S. Billion-Ton Update: Biomass Supply for a Bioenergy and Bioproducts Industry*, U.S. Department Of Energy. Oak Ridge National Laboratory, Oak Ridge, TN., **2011**.

[27] T. Werpy, G. Petersen, *Top Value Added Chemicals from Biomass: Volume I -- Results of Screening for Potential Candidates from Sugars and Synthesis Gas*, **2004**.

[28] K. J. Yong, T. Y. Wu, C. B. T. L. Lee, Z. J. Lee, Q. Liu, J. M. Jahim, Q. Zhou, L. Zhang, *Biomass and Bioenergy* **2022**, *161*, 106458.

[29] C. M. Cai, T. Zhang, R. Kumar, C. E. Wyman, *J of Chemical Tech & Biotech* **2014**, *89*, 2–10.

[30] E. Cousin, K. Namhaed, Y. Pérès, P. Cognet, M. Delmas, H. Hermansyah, M. Gozan, P. A. Alaba, M. K. Aroua, *Science of The Total Environment* **2022**, *847*, 157599.

[31] C. Chang, H. Wu, S. Zhao, X. Zhao, Q. Ma, P. Li, G. Xu, in *Advances in Bioenergy*, Elsevier, **2023**, pp. 1–91.

[32] Y. Lee, E. E. Kwon, J. Lee, *Rev Environ Sci Biotechnol* **2019**, *18*, 317–334.

[33] W. Yang, P. Li, D. Bo, H. Chang, *Carbohydrate Research* **2012**, *357*, 53–61.

[34] Q. Jing, X. Lü, *Chinese Journal of Chemical Engineering* **2007**, *15*, 666–669.

[35] X. Gu, X. Fu, S. Chen, *Industrial Crops and Products* **2021**, *162*, 113268.

[36] H. Chen, Z. Liu, *Engineering in Life Sciences* **2017**, *17*, 489–499.

[37] J. M. Corrêa, D. Christi, C. L. D. Torre, C. Henn, J. L. Da Conceição-Silva, M. K. Kadowaki, R. D. C. G. Simão, *Brazilian Journal of Microbiology* **2016**, *47*, 680–690.

[38] M. Taha, M. Foda, E. Shahsavari, A. Aburto-Medina, E. Adetutu, A. Ball, *Current Opinion in Biotechnology* **2016**, *38*, 190–197.

[39] R. Lin, C. Deng, J. Cheng, J. D. Murphy, *Renewable Energy* **2020**, *150*, 23–30.

[40] A. S. Matharu, K. Lokesh, in *Green Chemistry Series* (Eds.: R. Höfer, A.S. Matharu, Z. Zhang), Royal Society Of Chemistry, Cambridge, **2019**, pp. 1–17.

[41] S. Sun, S. Sun, X. Cao, R. Sun, *Bioresource Technology* **2016**, *199*, 49–58.

[42] B. C. Saha, *Journal of Industrial Microbiology and Biotechnology* **2003**, *30*, 279–291.

[43] V. Choudhary, S. I. Sandler, D. G. Vlachos, *ACS Catal.* **2012**, *2*, 2022–2028.

[44] H. Zhang, X. Liu, M. Lu, X. Hu, L. Lu, X. Tian, J. Ji, *Bioresource Technology* **2014**, *169*, 800–803.

[45] K. Wang, C. Liang, Q. Zhang, F. Zhang, *ACS Omega* **2019**, *4*, 1053–1059.

[46] N. K. Gupta, A. Fukuoka, K. Nakajima, *ACS Catal.* **2017**, *7*, 2430–2436.

[47] Y. Hayashi, *Chem. Sci.* **2016**, *7*, 866–880.

[48] M. Li, W. Li, Q. Liu, H. Jameel, H. Chang, S. An, L. Ma, *BioResources* **2016**, *11*, 8239–8256.

[49] H. J. Brownlee, *Ind. Eng. Chem.* **1927**, *19*, 422–424.

[50] E. Cousin, K. Namhaed, Y. Pérès, P. Cognet, M. Delmas, H. Hermansyah, M. Gozan, P. A. Alaba, M. K. Aroua, *Science of The Total Environment* **2022**, *847*, 157599.

[51] J. F. L. Silva, M. A. Selicani, T. L. Junqueira, B. C. Klein, S. Vaz Júnior, A. Bonomi, *Braz. J. Chem. Eng.* **2017**, *34*, 623–634.

[52] M. J. Antal, T. Leesomboon, W. S. Mok, G. N. Richards, *Carbohydrate Research* **1991**, *217*, 71–85.

[53] L. C. Nhien, N. V. D. Long, M. Lee, *Energies* **2021**, *14*, 1152.

[54] A. Mandalika, T. Runge, *Green Chem.* **2012**, *14*, 3175.

[55] S. B. Gadewar, M. F. Malone, M. F. Doherty, *Ind. Eng. Chem. Res.* **2000**, *39*, 1565–1575.

[56] In *Sugar Series*, Elsevier, **2000**, pp. 36–74.

[57] B. Kamm, M. Gerhardt, G. Dautzenberg, in *New and Future Developments in Catalysis*, Elsevier, **2013**, pp. 91–113.

[58] A. S. Mamman, J. Lee, Y. Kim, I. T. Hwang, N. Park, Y. K. Hwang, J. Chang, J. Hwang, *Biofuels Bioprod Bioref* **2008**, *2*, 438–454.

[59] O. Yemiş, G. Mazza, *Bioresource Technology* **2011**, *102*, 7371–7378.

[60] S. Vaz Jr., P. M. Donate, *BioResources* **2015**, *10*, 8168–8180.

[61] G. Marcotullio, W. De Jong, *Green Chem.* **2010**, *12*, 1739.

[62] W. Wang, J. Ren, H. Li, A. Deng, R. Sun, *Bioresource Technology* **2015**, *183*, 188–194.

[63] L. Zhang, H. Yu, P. Wang, H. Dong, X. Peng, *Bioresource Technology* **2013**, *130*, 110–116.

[64] W. Wang, H. Li, J. Ren, R. Sun, J. Zheng, G. Sun, S. Liu, *Chinese Journal of Catalysis* **2014**, *35*, 741–747.

[65] I. Agirrezabal-Telleria, A. Larreategui, J. Requies, M. B. Güemez, P. L. Arias, *Bioresource Technology* **2011**, *102*, 7478–7485.

[66] J. Tuteja, S. Nishimura, K. Ebitani, *Bulletin of the Chemical Society of Japan* **2012**, *85*, 275–281.

[67] R. O'Neill, M. N. Ahmad, L. Vanoye, F. Aiouache, *Ind. Eng. Chem. Res.* **2009**, *48*, 4300–4306.

[68] P. L. Dhepe, R. Sahu, *Green Chem.* **2010**, *12*, 2153.

[69] C. García-Sancho, J. M. Rubio-Caballero, J. M. Mérida-Robles, R. Moreno-Tost, J. Santamaría-González, P. Maireles-Torres, *Catalysis Today* **2014**, *234*, 119–124.

[70] A. Chareonlimkun, V. Champreda, A. Shotipruk, N. Laosiripojana, *Bioresource Technology* **2010**, *101*, 4179–4186.

[71] X. Shi, Y. Wu, P. Li, H. Yi, M. Yang, G. Wang, *Carbohydrate Research* **2011**, *346*, 480–487.

[72] S. Xu, D. Pan, Y. Wu, X. Song, L. Gao, W. Li, L. Das, G. Xiao, *Fuel Processing Technology* **2018**, *175*, 90–96.

[73] M. Li, W. Li, Q. Liu, H. Jameel, H. Chang, S. An, L. Ma, *BioResources* **2016**, *11*, 8239–8256.

[74] D. M. Alonso, S. G. Wettstein, M. A. Mellmer, E. I. Gurbuz, J. A. Dumesic, *Energy Environ. Sci.* **2013**, *6*, 76–80.

[75] R. Weingarten, J. Cho, Wm. C. Conner, Jr., G. W. Huber, *Green Chem.* **2010**, *12*, 1423.

[76] F. Delbecq, Y. Wang, C. Len, *Journal of Molecular Catalysis A: Chemical* **2016**, *423*, 520–525.

[77] J.-H. Kim, S.-M. Cho, J.-H. Choi, H. Jeong, S. M. Lee, B. Koo, I.-G. Choi, *Applied Sciences* **2020**, *11*, 163.

[78] H.-L. Li, S.-Y. Wang, W.-J. Wang, J.-L. Ren, F. Peng, R.-C. Sun, L. Liang, *BioResources* **2013**, *8*, 3200–3211.

[79] W. Dong, Z. Shen, B. Peng, M. Gu, X. Zhou, B. Xiang, Y. Zhang, *Sci Rep* **2016**, *6*, 26713.

[80] R. Noma, K. Nakajima, K. Kamata, M. Kitano, S. Hayashi, M. Hara, *J. Phys. Chem. C* **2015**, *119*, 17117–17125.

[81] G. Li, E. A. Pidko, E. J. M. Hensen, K. Nakajima, *ChemCatChem* **2018**, *10*, 4084–4089.

[82] S. M. A. H. Siddiki, Md. N. Rashed, Md. A. Ali, T. Toyao, P. Hirunsit, M. Ehara, K. Shimizu, *ChemCatChem* **2019**, *11*, 383–396.

[83] R. A. Rani, A. S. Zoolfakar, A. P. O'Mullane, M. W. Austin, K. Kalantar-Zadeh, *J. Mater. Chem. A* **2014**, *2*, 15683–15703.

[84] C. Valencia-Balvín, S. Pérez-Walton, G. M. Dalpian, J. M. Osorio-Guillén, *Computational Materials Science* **2014**, *81*, 133–140.

[85] M. Yang, S. Li, J. Huang, *ACS Appl. Mater. Interfaces* **2021**, *13*, 39501–39512.

[86] M. Kim, S. Ronchetti, B. Onida, N. Ichikuni, A. Fukuoka, H. Kato, K. Nakajima, *ChemCatChem* **2020**, *12*, 350–359.

[87] D. Padovan, K. Endo, T. Matsumoto, T. Yokoi, A. Fukuoka, H. Kato, K. Nakajima, *Small Structures* **2023**, *4*, 2200224.

Chapter 2

Lewis Acid Catalysis of Phosphate-Modified $CaNb_2O_6$ for Xylose Dehydration to Furfural

Abstract

Phosphate-modified $CaNb_2O_6$ (P-$CaNb_2O_6$) was synthesized via an amorphous metal complex (AMC) method and evaluated as a solid catalyst for the dehydration of xylose to furfural. Characterization revealed that orthorhombic $CaNb_2O_6$ features NbO_6 octahedra and CaO_8 square antiprisms, providing coordinatively unsaturated Lewis acid sites (LAS) and Brønsted acid sites (BAS). P-treatment further enhanced the LAS density and stability. Compared to Nb_2O_5, P-$CaNb_2O_6$ exhibited superior furfural yield and selectivity, attributed to the suppression of humin formation and the promotion of efficient dehydration pathways. Additionally, P-$CaNb_2O_6$ demonstrated excellent thermal stability and reusability, maintaining high catalytic performance over multiple cycles without structural degradation. These findings highlight the potential of P-$CaNb_2O_6$ as a durable and efficient catalyst for biomass valorization.

2.1 Introduction

The effective use of biomass-derived sugars, such as glucose and xylose, as renewable carbon resources can contribute to achieving carbon neutrality.[1] Xylose is a pentose sugar obtained via acid-catalyzed hydrolysis of xylan, the main component of hemicellulose.[2,3] The dehydration of xylose yields furfural, which is reported as one of the top-listed biobased products by the US Department of Energy due to its high potential applications as a green solvent, fuel additive, organic fertilizer, and valuable biopolymer precursor.[4–7] Previously, we demonstrated the water-tolerant Lewis acid catalysis of amorphous Nb_2O_5 is effective for xylose dehydration, with unsaturated coordination Nb^{5+} centers serving as pivotal active sites.[8–10] However, catalyst reusability remains a significant challenge.[11–13] In catalytic sugar conversion, insoluble polymers, called humin, are usually formed via the polymerization of the substrate, intermediates, and/or products. These by-products are deposited on the surface, leading to severe deactivation. Catalyst regeneration requires calcination (>500 °C) in the presence of oxygen to remove organic deposits, which induces the crystallization of amorphous Nb_2O_5, thereby reducing its intrinsic activity by a decrease in the number of unsaturated Nb^{5+} centers, i.e., catalytic active sites.[14–16] To overcome such thermal instability, it is essential to develop a crystalline Nb-based metal oxide catalyst that retains its activity even after the thermal post-treatment. The incorporation of additional elements into Nb_2O_5 to form Nb-based complex oxides changes its Lewis acidity and enhances its catalytic performance.[15,16] Similarly, phosphate treatment (P-treatment) effectively tunes catalyst surface properties.[8] Here, we report the catalysis of $CaNb_2O_6$, an alkaline earth metal niobate, for xylose dehydration. Orthorhombic $CaNb_2O_6$ consists of octahedral NbO_6 and square antiprismatic CaO_8 with an edge-sharing structure, while orthorhombic Nb_2O_5 features

edge-shared NbO_6 and pentagonal bipyramidal NbO_7 (**Figure 2.1**). In crystalline niobium oxides, niobium atoms that contain oxygen vacancies within NbO_6 or NbO_7 polyhedra can act as Lewis acid sites. In $CaNb_2O_6$, the situation is more complex, and several structural motifs may contribute to Lewis acidity. Because Ca^{2+} has a fully occupied electron configuration with no low-energy vacant orbitals, it can scarcely accept electron pairs and cannot function as a Lewis acid. Consequently, only the niobium atoms in Nb–O–Nb and Nb–O–Ca linkages can be regarded as Lewis acid sites (**Figure 2.2**). We hypothesized that the unstable edge-sharing structure of $CaNb_2O_6$ facilitates the formation of coordinatively unsaturated Lewis acid sites, enhancing the activity in xylose dehydration. Such a structural future is specific to $CaNb_2O_6$ compared to other alkaline earth metal niobates. Furthermore, phosphate group can exist on the crystal surface in three possible forms: (A) coordinated with Nb; (B) anchored to lattice oxygen; and (C) functioning as Brønsted acid sites. The effects of phosphoric acid treatment (P-treatment) on crystalline Nb_2O_5 and $CaNb_2O_6$ were also investigated to enhance their catalytic activity, as presented in **Figure 2.3**

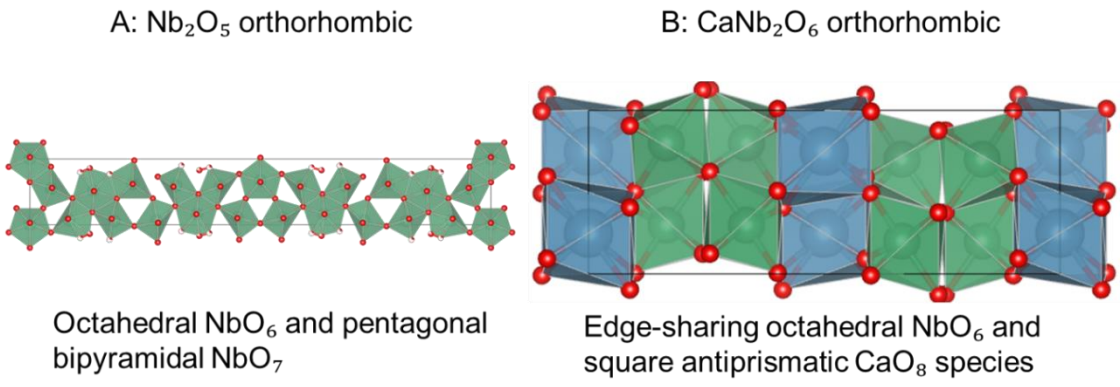

Figure 2.1. Crystalline structures of (A) Nb_2O_5 and (B) $CaNb_2O_6$. Red, blue and green balls indicate O, Nb and Ca, respectively.

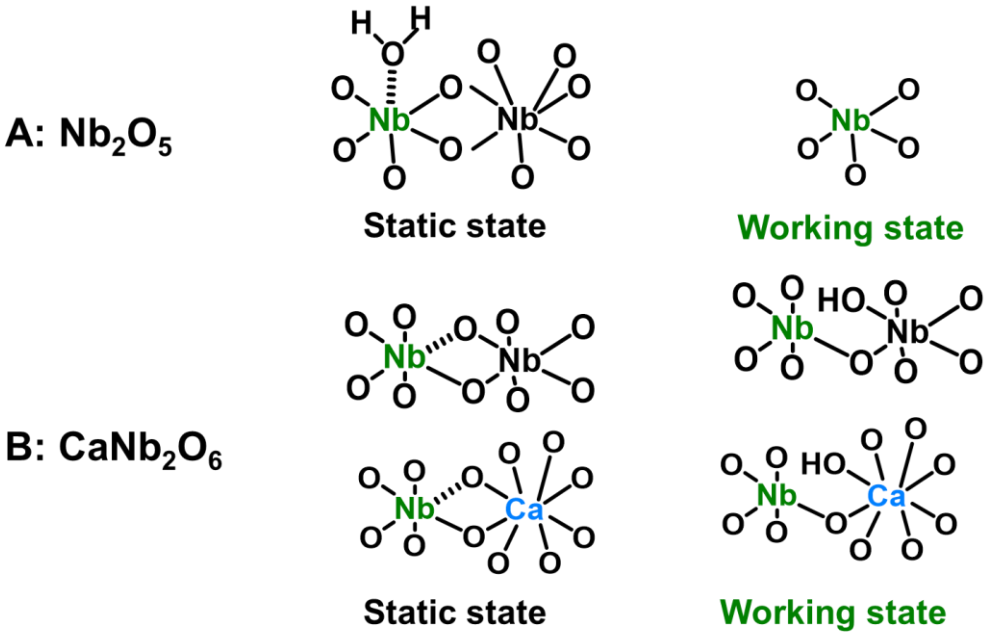

Figure 2.2. Possible Lewis acid sites situations in (A) Nb_2O_5 and (B) $CaNb_2O_6$

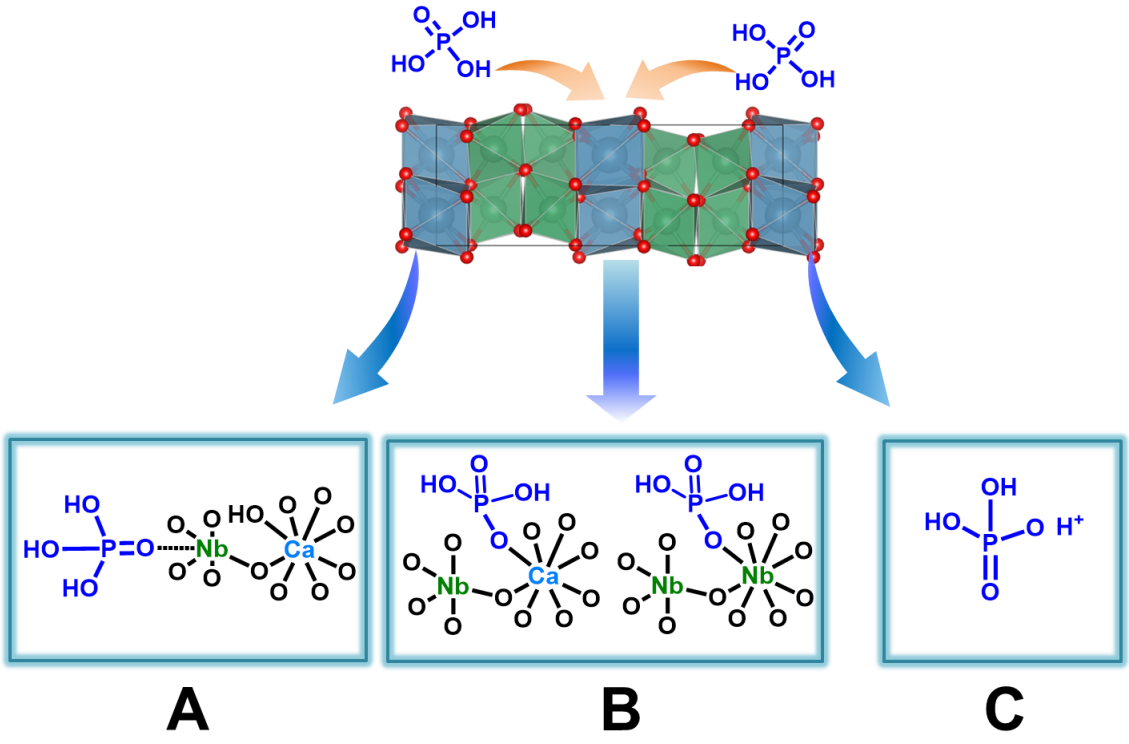

Figure 2.3. Possible phosphate group immobilization situations. (A) coordinated with Nb; (B) anchored to lattice oxygen; and (C) functioning as Brønsted acid sites.

2.2 Experimental section

2.2.1 Chemical reagents

$NbCl_5$ was purchased from HIGH PURITY CHEMICALS. Hydrogen peroxide (30–35 wt%), phosphoric acid (>85 wt%), toluene, and chloroform were supplied by KANTO CHEMICAL CO., INC. Ammonia aqueous solution (28 wt%), L-lactic acid, calcium nitrate tetrahydrate, sulfuric acid (>95 wt%), D(+)-xylose, and pyridine (dehydrated) were obtained from FUJIFILM Wako Pure Chemical Corporation. Scandium trifluoromethanesulfonate, furfural, and chlorobenzene were received from Tokyo Chemical Industry (TCI). Amberlyst-15 was supplied by Sigma-Aldrich. H-Beta was provided by the Catalysis Society of Japan (JRC-Z-HB150).

2.2.2 Catalysts preparation

$CaNb_2O_6$ was synthesized by the amorphous metal complex (AMC) method using water-soluble niobium lactate ($Nb(CH_3CH(OH)COO)(CH_3CH(O)COO)_2$ denoted as Nb-LA).[17,18] $NbCl_5$ (25 g) was slowly added to 300 mL of distilled water, after which the pH was adjusted to 7.0 using ammonia aqueous solution. The mixture was then stirred at 600 rpm for 3 h. After adjusting the pH to 7.0, the precipitate was recovered by filtration and washed with distilled water to remove Cl^- ions, obtaining wet paste of amorphous Nb_2O_5. The amorphous Nb_2O_5 (10 mmol) was added to a mixture of lactic acid (80 mmol) and hydrogen peroxide (200 mmol). After adjustment of the pH to 4.5 with ammonia aqueous solution, the mixture was stirred at 60 °C for 1 h and at 90 °C overnight to obtain Nb-LA. The mixture of calcium nitrate tetrahydrate (10 mmol) and lactic acid (30 mmol) and 5 mL of distilled water was sonicated until the solid was completely dissolved. After the

addition of an aqueous Nb-LA solution (20 mmol), the solution was gelled at 110 °C for 1 h and heated stepwise (250 °C for 1 h, 450 °C for 3 h) with a slow ramping rate to form a black powder. Carbonaceous species derived from lactic acid were then removed by high-temperature calcination in a muffle oven at 700 °C for 5 h to obtain $CaNb_2O_6$. The same preparation processes were applied to T-phase Nb_2O_5 simply using 10 mmol of Nb precursor without calcium nitrate tetrahydrate. $CaNb_2O_6$ and Nb_2O_5 were treated with phosphoric acid to immobilize phosphate moiety on their surfaces. Typically, the sample (1 g) was added to an aqueous phosphoric acid solution (1M, 200 mL) and stirred at room temperature for two days. The solid was recovered by filtration and washed with water until the pH of the filtrate became neutral and then dried overnight in an oven to obtain a phosphate-immobilized sample (P-$CaNb_2O_6$ and P-Nb_2O_5).

2.2.3 Characterization

X-ray diffraction (XRD) measurement was performed on an Ultima IV Rigaku diffractometer set at 40 kV and 40 mA using Cu Kα radiation (λ = 1.5418 Å). Nitrogen adsorption experiment was conducted at 77 K using a Micromeritics 3-Flex instrument after the sample was degassed at 150 °C for 1 h. Brunauer-Emmett-Teller (BET) surface area was calculated over a relative pressure (P/P0) range from 0.05 to 0.30. X-ray photoelectron spectroscopy (XPS) was performed using a JEOL JPS-9010MC. Data analysis was carried out using CasaXPS software. Fourier transform (FT) infrared (IR) spectra were obtained using a JASCO FT/IT-4100 with a mercury cadmium telluride (MCT) detector. The self-supported disk (20 mm, 40–90 mg) was placed in an IR cell connected to a closed gas-circulation system and pretreated at 300 °C for 1 h under vacuum to remove physisorbed water. Pyridine or chloroform was used as a probe

molecule for characterizing acidity. The spectra were recorded with 4 cm-1 resolution and 64 scans. Thermogravimetric analysis (TGA) was performed on a Rigaku Thermo plus Evo2 instrument. Samples (10 mg) were heated from 30 to 800 °C with the ramping rate of 10 °C min^{-1} at a constant airflow of 50 mL min^{-1}.

2.2.4 Furfural production from xylose dehydration

The catalytic reaction was typically conducted in a pressure-resistant spherical glass reactor using 75 mg of xylose in 2 mL of water and 8 mL of toluene with 300 mg of catalyst. In this system, toluene functions as an extraction solvent for furfural, and contributes to improving the selectivity of furfural.[8] The reaction mixture was heated in an oil bath. After the reaction, the reactor was completely cooled in the ice bath, and the reaction mixture was separated by centrifugation. The aqueous phase was analyzed using a Shimadzu LC-2030C Plus high-performance liquid chromatograph. The mobile phase consisted of a 5 mmol L^{-1} sulfuric acid solution. The reactants were separated using a BIO-RAD Aminex HPX-87H column and detected by a refractive index detector (RID-20A) and an ultraviolet detector (245 nm). The organic phase was quantified using chlorobenzene as an internal standard and analyzed by a gas chromatograph (GC, Shimadzu, GC-2025AF) equipped with a flame ionization detector (FID). Conversion, yields and selectivity were calculated based on the following equations. In this study, the detectable product is limited only to furfural, meaning that by-products are defined as "humin-type undetectable species".

$$\boldsymbol{Conversion} = \mathbf{100\%} * \frac{\boldsymbol{Moles\ of\ xylose_{initial} - Moles\ of\ sylose_{final}}}{\boldsymbol{Moles\ of\ xylose_{initial}}} \quad \textit{(1)}$$

$$\boldsymbol{Yield_{fufural}} = \mathbf{100\%} * \frac{\boldsymbol{Moles\ of\ furfural_{final}}}{\boldsymbol{Moles\ of\ xylose_{initial}}} \quad \textit{(2)}$$

$$Yield_{by-products} = Moles\ of\ xylose_{initial} - Yield_{fufural} \quad (3)$$

$$Selectivity_{furfural} = 100\% * \frac{Yield_{fufural}}{Conversion} \quad (4)$$

2.3 Results and discussion

2.3.1 Surface acidity modification of $CaNb_2O_6$ and Nb_2O_5 by phosphate incorporation

The amorphous metal complex (AMC) method using a water-soluble niobium peroxo complex was employed to prepare high surface area catalysts.[17,18] The P-treatment was performed by the procedure reported in our previous papers using a 1 M H_3PO_4 aqueous solution.[8] X-ray diffraction (XRD) measurements (**Figure 2.4**) revealed that the orthorhombic phases of both $CaNb_2O_6$ and Nb_2O_5 are retained after P-treatment. N_2 adsorption-desorption measurements (**Table 2.1**) showed that $CaNb_2O_6$ has a larger Brunauer–Emmett–Teller (BET) surface area than Nb_2O_5, likely due to the incorporation of the light Ca element. The P content of the catalysts was estimated using an X-ray photoelectron spectroscopy (XPS) (**Figure 2.5**) as 3.9 atom% for P-Nb_2O_5 and 2.6 atom% for P-$CaNb_2O_6$ (**Table 2.1**).

The acid properties of the catalysts were characterized by in-situ infrared (IR) spectroscopy with pyridine as a basic probe molecule to quantify Brønsted acid site (BAS) and Lewis acid site (LAS).[19,20] **Figure 2.6** displays the difference IR spectra of adsorbed pyridine molecules on Nb_2O_5 and $CaNb_2O_6$ before and after P-treatment (**Figure 2.9** for O-H and C-H stretching vibrations). Both Nb_2O_5 and P-Nb_2O_5 have two specific bands at 1605 and 1444 cm^{-1} corresponding to typical vibrational modes of the pyridine coordinated on LAS. The P-treatment for Nb_2O_5 reduced LAS density (**Table 2.1**),

indicating that phosphate molecules deactivate some LASs (**Figure 2.8**). The active LAS of amorphous Nb_2O_5 has been proposed as the tetrahedrally coordinated NbO_4 in our previous study[8,9] and they are fully stabilized with weakly coordinated and exchangeable H_2O ligand(s). The active LAS of crystalline Nb_2O_5 is likely associated with the octahedrally coordinated but oxygen-defective NbO_6, and a portion of these LASs lose their Lewis acidity upon reaction with phosphoric acid. In contrast, $CaNb_2O_6$ has two apparent differences compared to Nb_2O_5: 1) variations in band frequency around 1600 cm^{-1} and 2) the presence of BAS. Two distinct bands were observed at 1608 and 1602 cm^{-1} for $CaNb_2O_6$ and P-$CaNb_2O_6$, which are well-known vibrational modes sensitive to metal type, coordination environment, and acid strength.[19,21,22] For instance, the vibrational frequency of adsorbed pyridine on octahedrally coordinated AlO_6 in γ-Al_2O_3 appears at a lower frequency than that of tetrahedrally coordinated AlO_4.[23] In the case of $CaNb_2O_6$ and P-$CaNb_2O_6$, as shown in **Figure 2.7**, differences in the coordination environment between defects in Nb-O-Nb and in Nb-O-Ca suggest that the two observed bands can be assignable to distinct LASs. This contrasts with Nb_2O_5, which contains only Nb–O–Nb linkages and exhibits a single band at 1605 cm^{-1}. For P–$CaNb_2O_6$, four possible types of Lewis acid sites may exist; however, FTIR may not be able to distinguish between the states before and after the loading of phosphate groups onto the catalyst surface. As a result, only two peaks at 1608 and 1602 cm^{-1} are observed. Since the vibrational band for liquid-phase pyridine is present at 1580 cm^{-1}, the higher frequencies observed for $CaNb_2O_6$ indicate stronger interactions, i.e., stronger LASs. Consequently, $CaNb_2O_6$ has both slightly stronger and weaker LASs compared to Nb_2O_5. According to Pauling's principles, the edge-sharing structure is less stable than the corner-sharing structure, leading to a preferential formation of defect sites at Nb-O-Ca bonds. Another

notable difference is the presence of BAS in $CaNb_2O_6$ and P-$CaNb_2O_6$. A weak band at 1542 cm^{-1}, assignable to the vibrational mode of the pyridinium cation,[19,20] was observed in $CaNb_2O_6$ and became pronounced in P-$CaNb_2O_6$. The numbers of BASs are summarized in **Table 2.1**. The Brønsted acidic nature of $CaNb_2O_6$ probably originates from the polarized Nb-O-Ca bond, where a proton is formed on a negatively charged oxygen atom to satisfy charge compensation. Still, the amount of BAS is negligibly small. P-treatment enhances the hydrolysis of polarized Nb-O-Ca bonds, resulting in the formation of Ca-O-$PO(OH)_2$ and unsaturated coordination Nb sites, as illustrated in **Figure 2.8**. The process explains the increase in BASs, which can be attributed to the immobilization of phosphate molecule. The formation of LAS can be supported by the increased band intensity at 1602 cm^{-1}. The unsaturated coordination Nb formed by P-treatment are stabilized with weakly coordinated and exchangeable H_2O ligand(s) and serve as LASs in acid-catalyzed reactions.

Table 2.1. Surface properties of prepared catalysts

Catalyst	Surface area (m^2 g^{-1})[a]	Lewis acid sites (μmol g^{-1})[b]	Brønsted acid sites (μmol g^{-1})[b]	Surface P ratio (%)[c]
P-$CaNb_2O_6$	23	37	10	2.6
$CaNb_2O_6$	23	32	<10	-
P-Nb_2O_5	9	14	-	3.9
Nb_2O_5	9	23	-	-

Determined by [a] N_2 adsorption, [b] FTIR-pyridine adsorption and [c] XPS

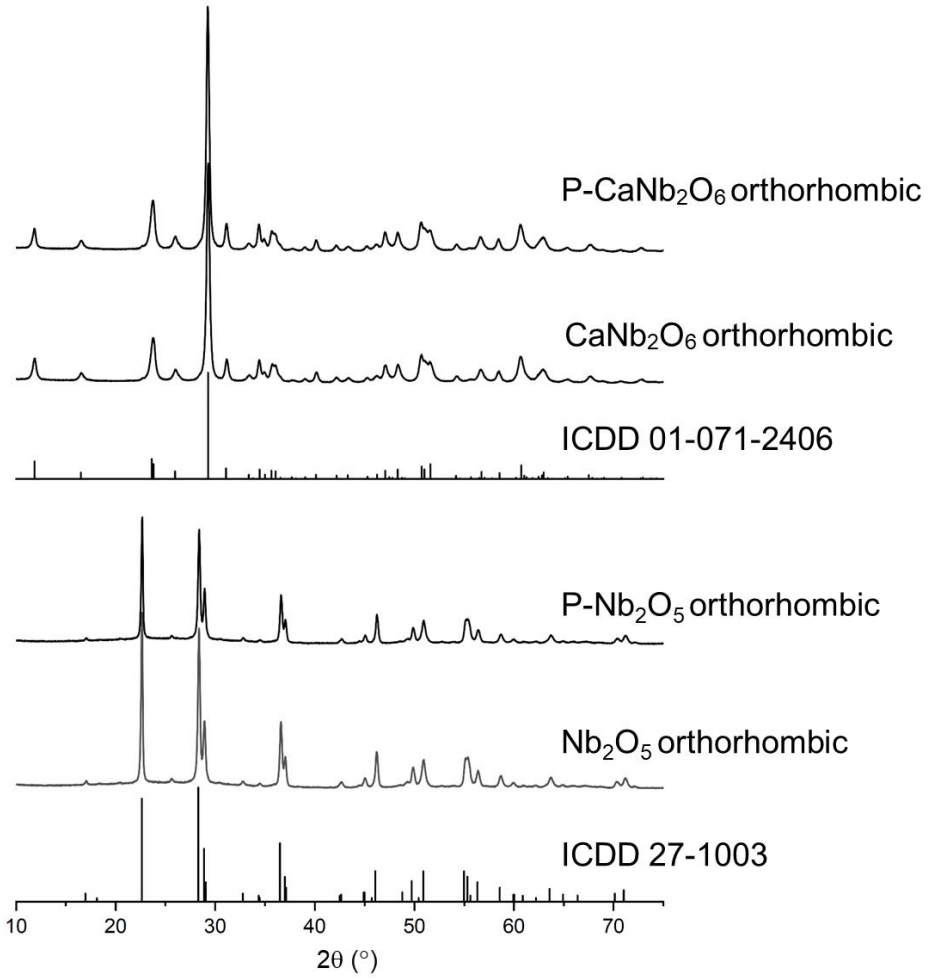

Figure 2.4. XRD patterns for prepared samples.

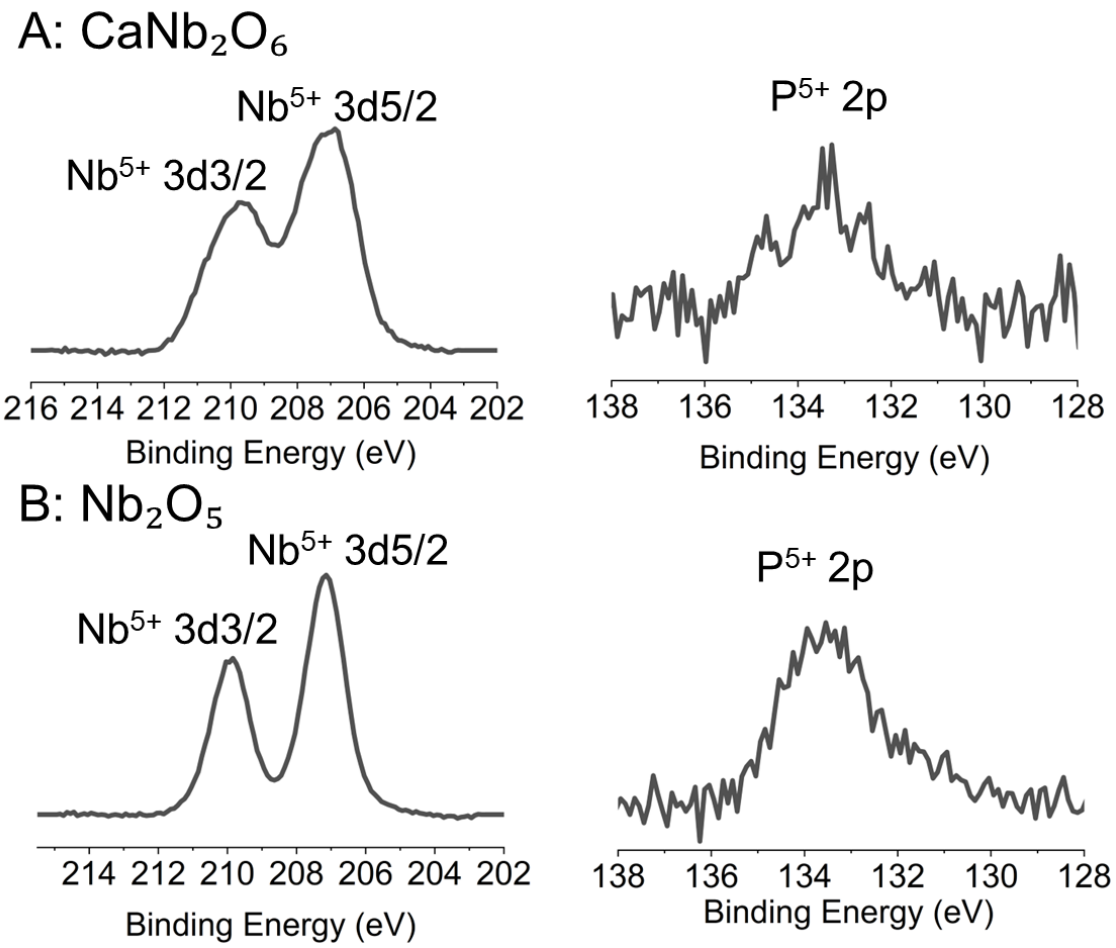

Figure 2.5. XPS data of (A) P-$CaNb_2O_6$ and (B) P-Nb_2O_5.

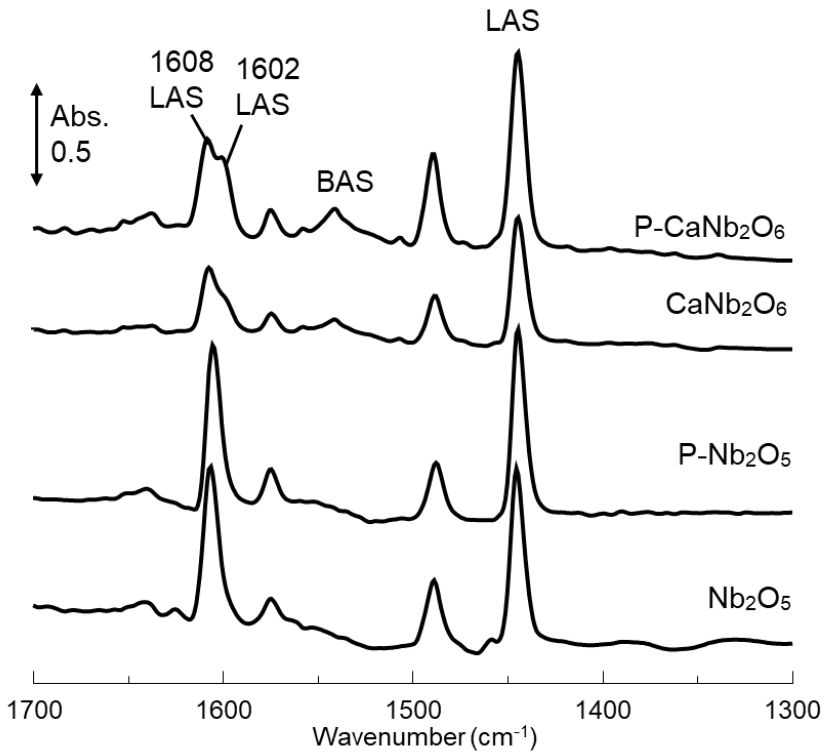

Figure 2.6. Difference IR spectra of adsorbed pyridine molecules on the prepared catalysts.at 30 °C.

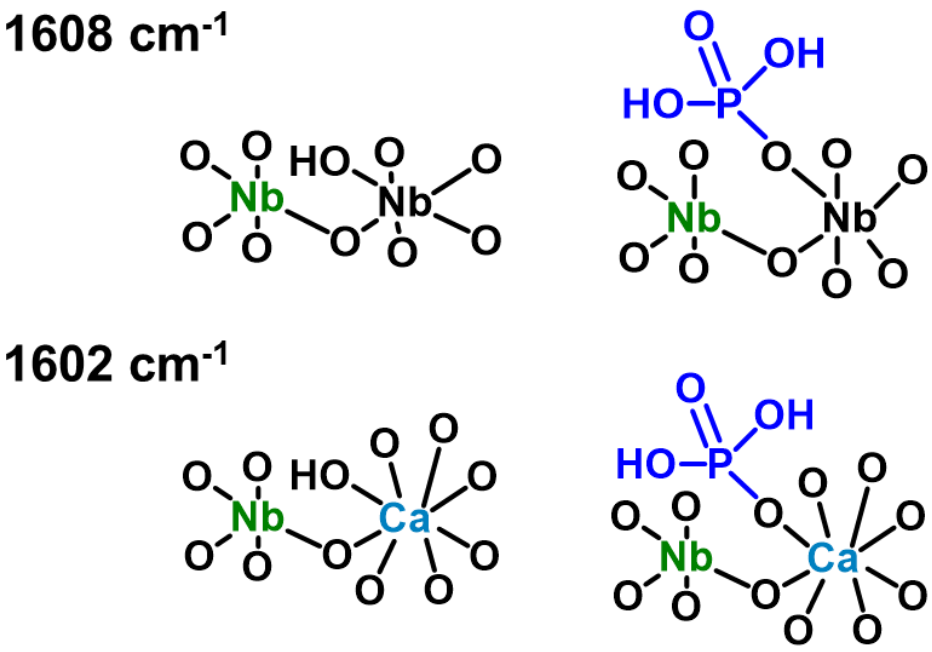

Figure 2.7. The possible types of Lewis acid sites in P–$CaNb_2O_6$ at 1608 and 1602 cm^{-1}

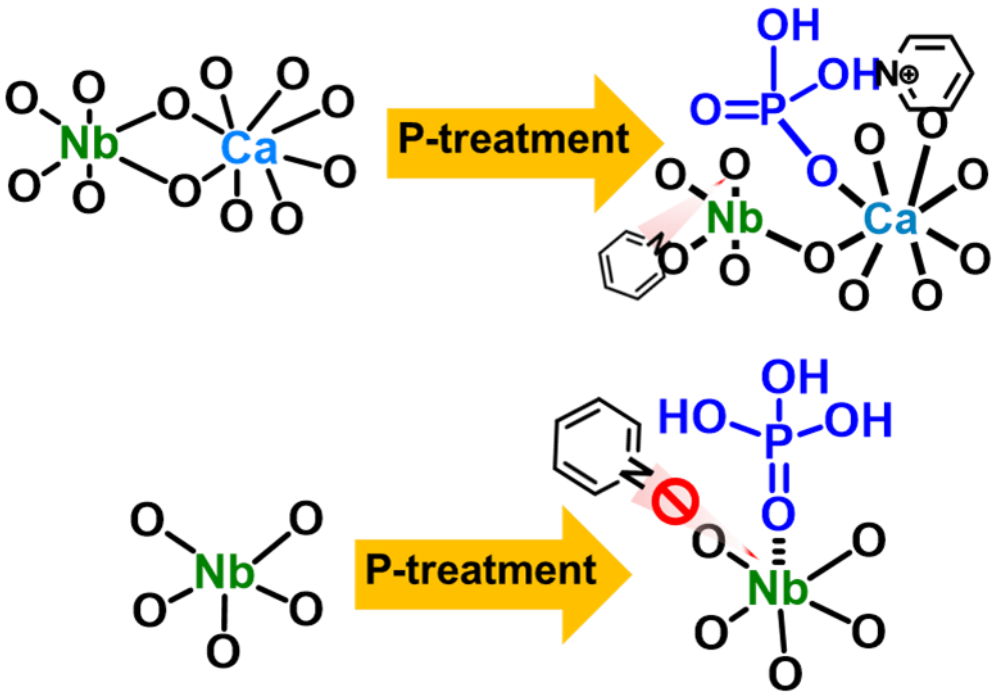

Figure 2.8. Plausible structures of acid sites on Nb_2O_5 and $CaNb_2O_6$ before and after P-treatment. White circles indicate oxygen defect sites.

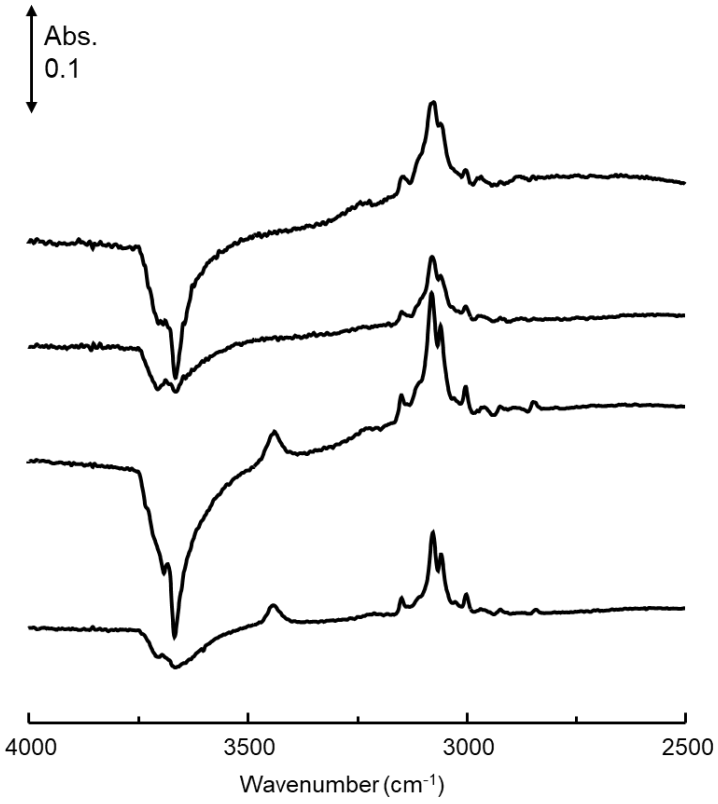

Figure 2.9. Difference IR spectra in O-H and C-H stretching vibrations of adsorbed pyridine molecules on each catalyst at 30 °C.

2.3.2 Catalytic performance for furfural production

The catalytic performance of Nb_2O_5 and $CaNb_2O_6$ was evaluated in the dehydration of xylose (**Figure 2.10**). While $CaNb_2O_6$ showed almost the same furfural yield as Nb_2O_5, its furfural selectivity was low. This low furfural selectivity indicates the formation of polymerized by-product so-called humin, which is most likely catalyzed by relatively stronger LASs derived from the octahedrally coordinated Nb^{5+} centers in $CaNb_2O_6$. The P-treatment improved the catalytic performance of both $CaNb_2O_6$ and Nb_2O_5. Notably, P-$CaNb_2O_6$ exhibited higher furfural yield and selectivity compared to the parent $CaNb_2O_6$, even at almost the same levels of xylose conversion. This improvement suggests an increased rate of furfural formation accompanied by a decreased rate of humin formation. On the contrary, P-Nb_2O_5 showed enhanced furfural selectivity without a significant increase in furfural yield. This behavior suggests that the LAS responsible for humin formation is deactivated by the formation of phosphate moieties on the surface. The effect of P-treatment on crystalline Nb_2O_5 was consistent with that observed for amorphous Nb_2O_5, but the enhanced activity of $CaNb_2O_6$ after P-treatment cannot be explained by the deactivation of LAS that causes side reactions.

Our previous study on amorphous Nb_2O_5 revealed that LAS produces furfural through the stepwise dehydration of xylose, and intrinsic BAS does not participate in furfural formation (**Figure 2.11**).[8] Assuming that crystalline Nb_2O_5 and $CaNb_2O_6$ follow the same reaction pathway, the high activity of P-CaNb2O6 is unlikely to result from the increased BAS after the P-treatment. Instead, the improved furfural selectivity of CaNb2O6 is primarily interpreted by the decrease of LAS that causes humin formation. In addition, the increased furfural yield is mainly attributed to an increase in LAS effectiveness for furfural formation (**Table 2.1**). We speculate that the increase in both

LAS and BAS to the hydrolysis of polar Ca-O-Nb bond generating phosphate-based BAS and Nb-based LAS during the P-treatment (**Figure 2.8**). To investigate the effect of phosphate loading on the activity of the resulting P-$CaNb_2O_6$, we synthesized several P-$CaNb_2O_6$ samples by both a conventional wet-impregnation method and an equilibrium adsorption method. In the wet-impregnation method, the samples were denoted as X % P-$CaNb_2O_6$ where X represents the weight percentage of phosphate molecules impregnated onto $CaNb_2O_6$. In the equilibrium adsorption method, phosphoric acid solutions with two different concentrations (0.5 M and 1.0 M) were employed to prepare P-$CaNb_2O_6$. The samples prepared with 0.5 M and 1 M solutions were denoted as P-$CaNb_2O_6$ and 0.5M P-$CaNb_2O_6$, respectively. No significant difference in the activity between P-Nb_2O_5 and 0.5M P-$CaNb_2O_6$ suggests that the $CaNb_2O_6$ surface is saturated to a similar extent with phosphate groups in both treatments, affording comparable sample. In contrast, the impregnated catalysts exhibited similar activity to bare $CaNb_2O_6$, meaning that phosphate molecules immobilized via the equilibrium adsorption method are essential for enhancing the acid properties and, consequently, improving the catalytic activity. The effect of phosphate loading on the activity of the resulting P-$CaNb_2O_6$ revealed that phosphate molecules immobilized via the equilibrium adsorption method are essential for enhancing the acid properties and improving the catalytic activity (**Table 2.1 and Figure 2.12**).

Control reactions were performed using reference catalysts to confirm the unique catalysis of P-$CaNb_2O_6$. A mixture of $CaNb_2O_6$ and H_3PO_4 improves the target product yield compared to $CaNb_2O_6$ alone. However, the product yield remained lower than that of P-$CaNb_2O_6$, which evidences that the catalysis of P-$CaNb_2O_6$ is not merely derived from the simple combination of $CaNb_2O_6$ and H_3PO_4. P-$CaNb_2O_6$ demonstrated a higher

furfural yield than conventional homogeneous Lewis acid catalyst, $Sc(OTf)_3$. Since Brønsted acid catalysts are known for high furfural selectivity,[24,25] we compared the catalytic activity of typical homogeneous and heterogeneous Brønsted acid catalysts, such as H_2SO_4, a sulfonated polystyrene resin (Amberlyst-15) and H-Beta zeolite. Although the selectivity of P-$CaNb_2O_6$ was slightly lower than that of these Brønsted acid catalysts, it still showed a higher furfural yield, highlighting its great potential as a solid acid catalyst for xylose dehydration. The time-course experiments (**Figure 2.13**) showed no significant difference in furfural selectivity between the two catalysts during the reaction, but the reaction rate for furfural formation with P-$CaNb_2O_6$ was larger than that with P-Nb_2O_5, likely due to the large amounts of LAS. Hot filtration experiments (**Figure 2.14**) indicate that the reaction completely stopped after the catalyst was removed, implying no obvious leaching of the phosphate molecules during the reaction.

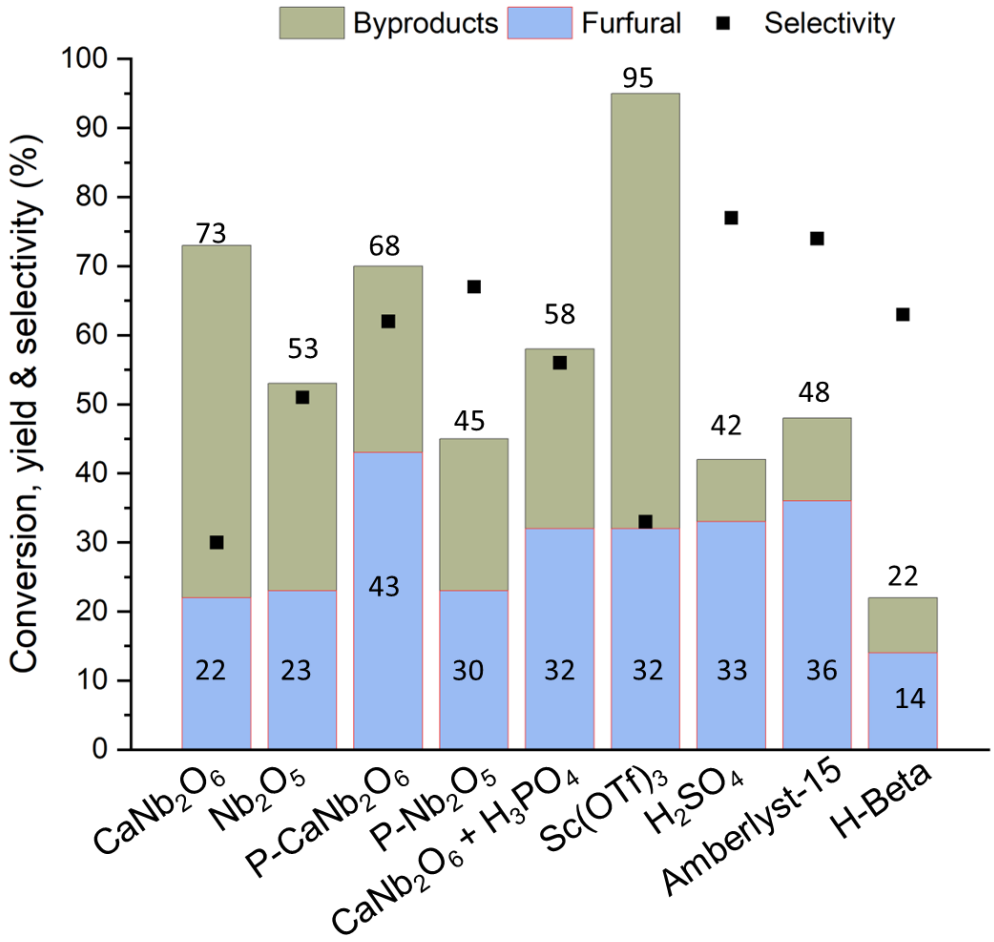

Figure 2.10. Catalytic activity of various catalysts for xylose conversion. Reaction conditions: Xylose, 75 mg; catalyst, 300 mg; toluene, 8 mL; water, 2 mL, temperature, 120 °C; time, 5 h. 0.01 mol% of H_3PO_4, 80 mol% of H_2SO_4, and 20 mol% of $Sc(OTf)_3$ to substrate were used for the reaction.

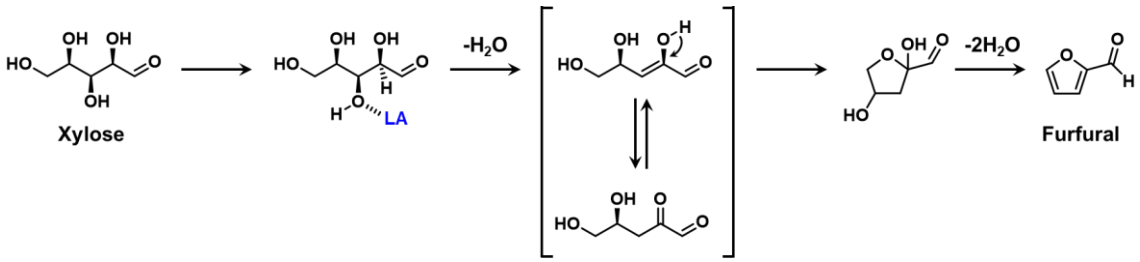

Figure 2.11. Proposed reaction mechanism for xylose dehydration over Lewis acidic metal oxides via stepwise dehydration.[8]

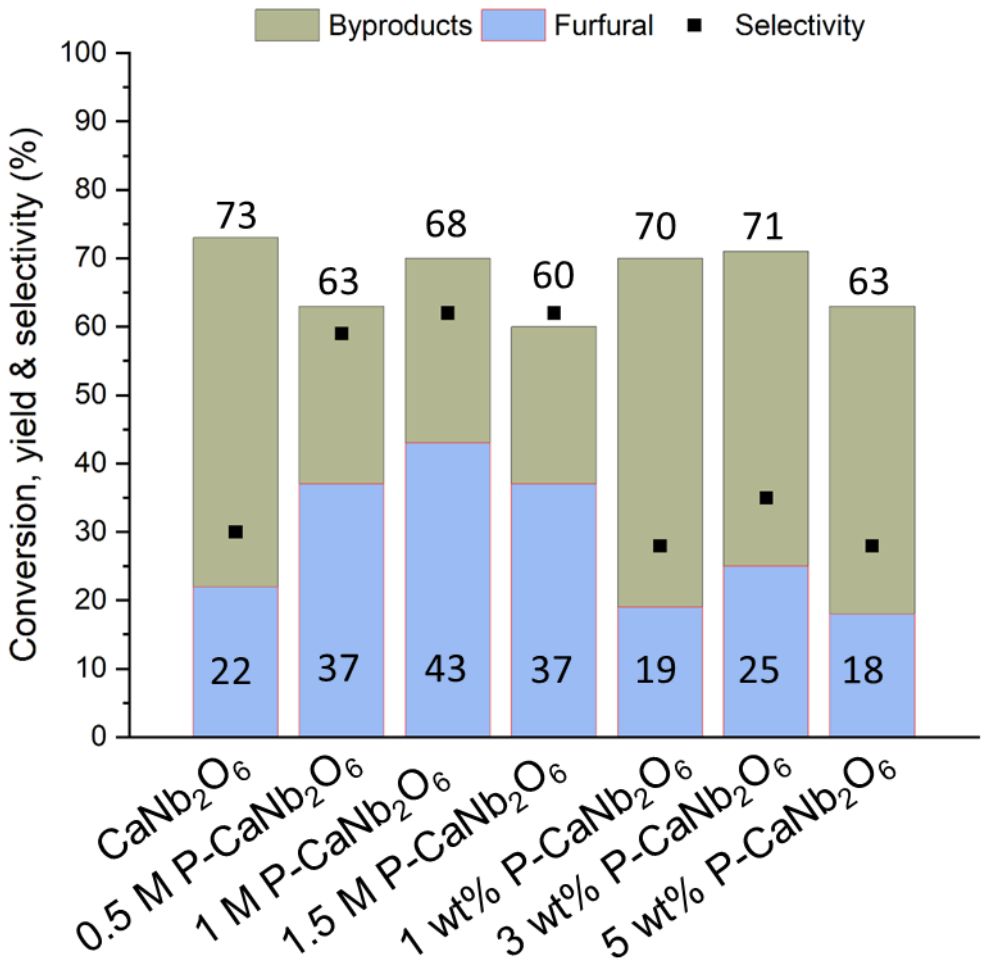

Figure 2.12. Effect of phosphate loading (wet-impregnation vs equilibrium adsorption) on the catalytic activity of the resulting $CaNb_2O_6$. Reaction conditions: xylose, 75 mg; catalyst, 300 mg; toluene, 8 mL; water, 2 mL, temperature, 120 °C, time, 5 h. By-products indicate undetectable products, calculated by subtracting the total yield of detectable products (only furfural in this study) from the xylose conversion. The sum of the blue and gray bars means the xylose conversion.

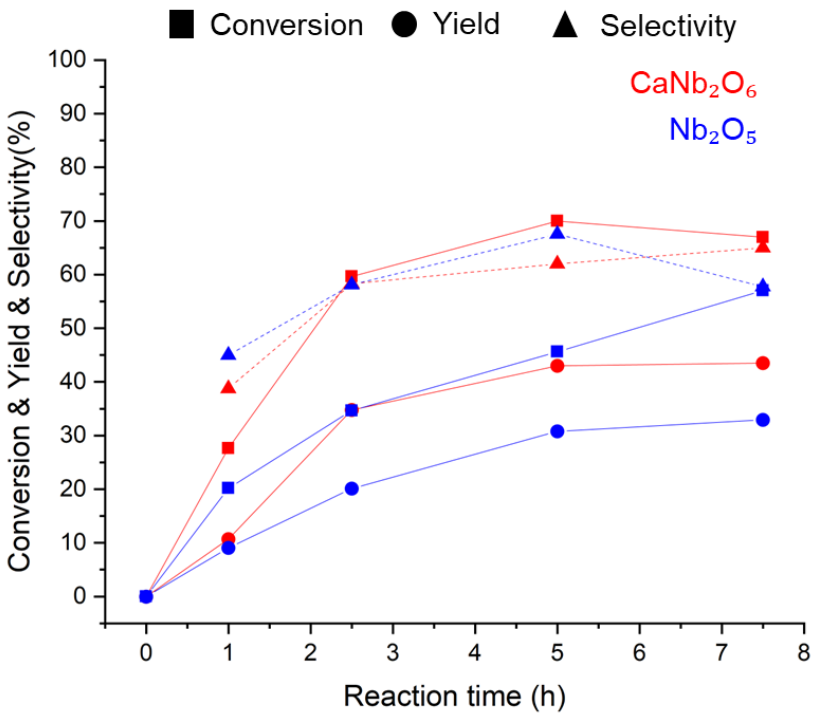

Figure 2.13. Time course for xylose dehydration with P-$CaNb_2O_6$ and P-Nb_2O_5. Reaction conditions: Xylose, 75 mg; catalyst, 300 mg; toluene, 8 mL; water, 2 mL, temperature, 120 °C.

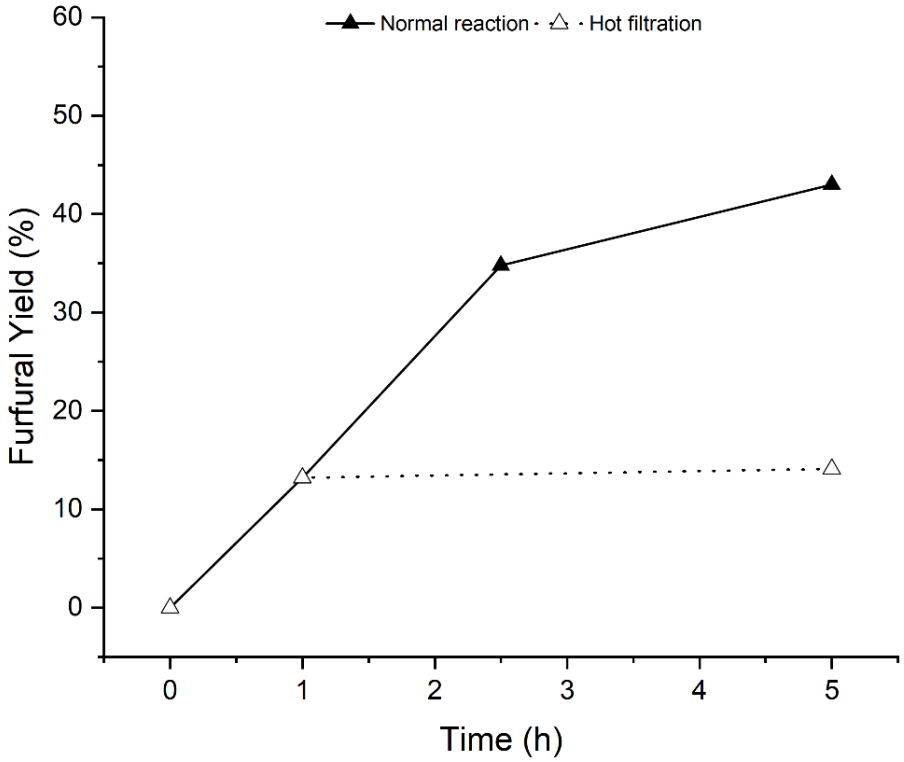

Figure 2.14. Leaching test for P-$CaNb_2O_6$. Reaction conditions: Xylose, 75 mg; catalyst, 300 mg; toluene, 8 mL; water, 2 mL, temperature, 120 °C.

2.3.3 Reusability

The reusability of heterogeneous catalysts is crucial for industrial applications and serves as a key indicator of catalyst performance. Amorphous Nb_2O_5 (Nb_2O_5-am) is a promising catalyst for xylose dehydration. To highlight the advantages of the crystalline material, the reusability of Nb_2O_5-am and P-$CaNb_2O_6$ was evaluated. Prior to the reusability test, thermogravimetric-differential thermal analysis (TG-DTA) of fresh and spent P-$CaNb_2O_6$ was performed to determine the optimal regeneration temperature (**Figure 2.15**). Continuous weight loss was detected up to 500 °C in the spent catalyst, accompanied by a slight exothermic peak due to the deposited humin species, while there was almost no weight loss in the fresh catalyst. Therefore, the spent catalyst was calcined at 500 °C for 5 h in air to remove the organic deposits before reuse. Nb_2O_5-am decreased steeply its original activity for the first and second reuse tests (**Figure 2.16**), This deactivation is caused by the crystallization of the amorphous Nb_2O_5 phase during the calcination process, because the strong acidity of Nb_2O_5-am is derived from its amorphous nature.[15] The calcination treatment of Nb_2O_5-am formed orthorhombic Nb2O5 (**Figure 2.17**) and also decreased the BET surface area from 120 to 67 m2 g-1. In contrast, P-$CaNb_2O_6$ retained its original activity even after five cycles (**Figure 2.18**). XRD measurements revealed no difference between fresh and spent P-$CaNb_2O_6$ (**Figure 2.19**), evidencing its high thermal stability during regeneration treatment.

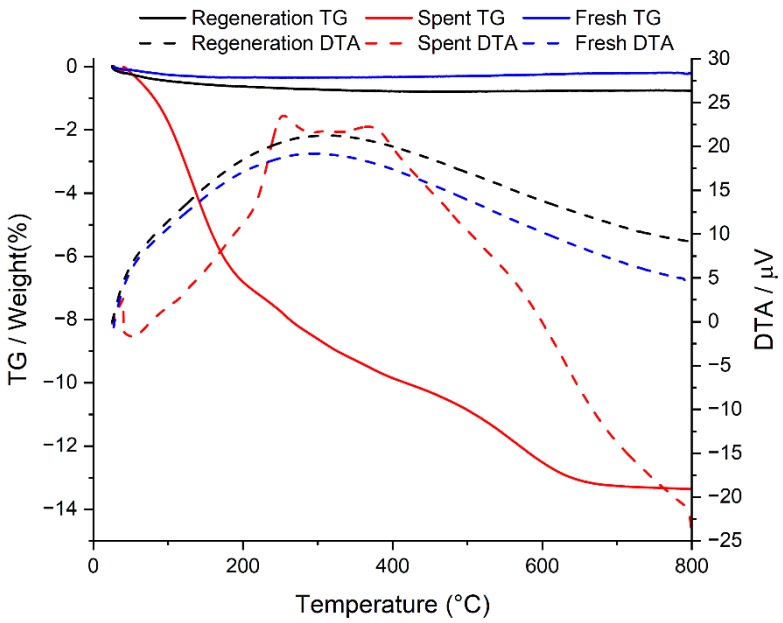

Figure 2.15. TG-DTA profiles for P-$CaNb_2O_6$ before (blue) and after (red) the reaction.

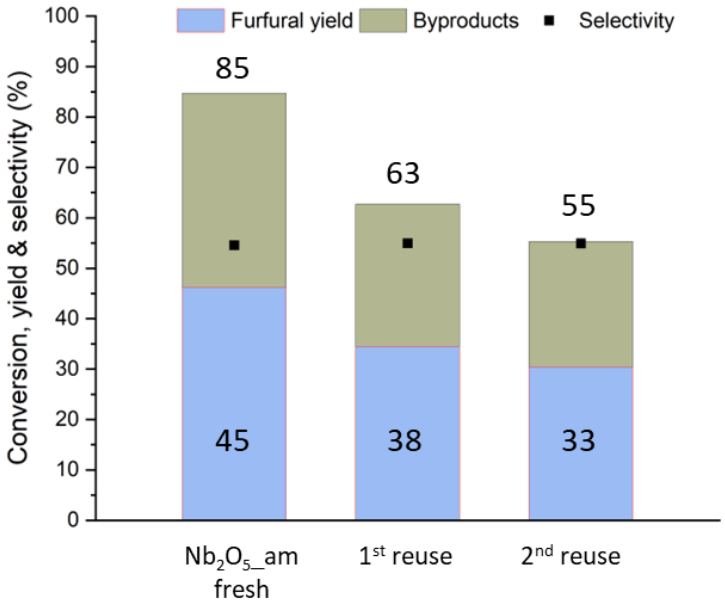

Figure 2.16. The reusability test of Nb_2O_5-am for xylose dehydration. Reaction conditions: Xylose, 75 mg; catalyst, 300 mg; toluene, 8 mL; water, 2 mL, temperature, 120 °C; time, 5 h. By-products indicate undetectable products, calculated by subtracting the total yield of detectable products (only furfural) from the xylose conversion. The sum of the blue and gray bars means the xylose conversion.

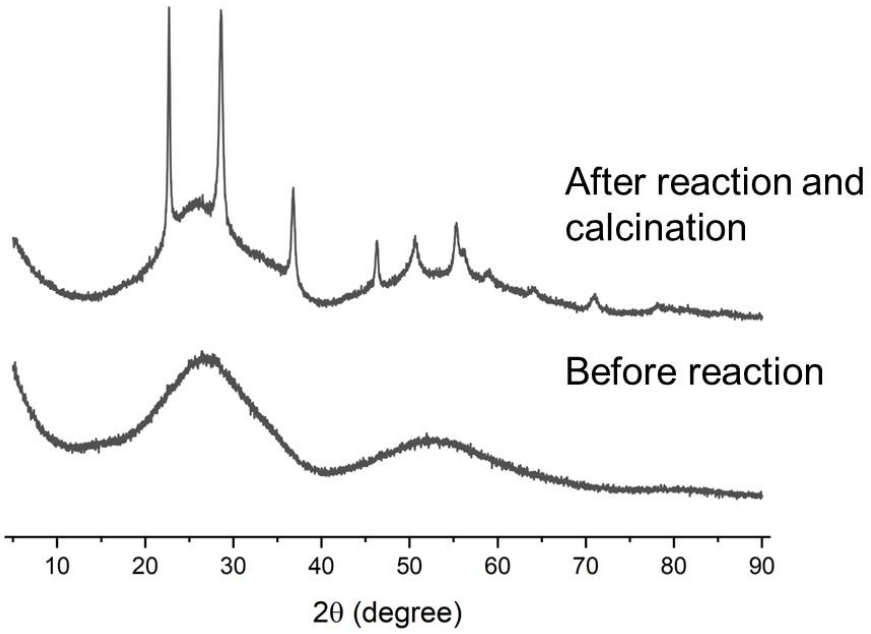

Figure 2.17. XRD patterns of Nb_2O_5-am before and after reaction.

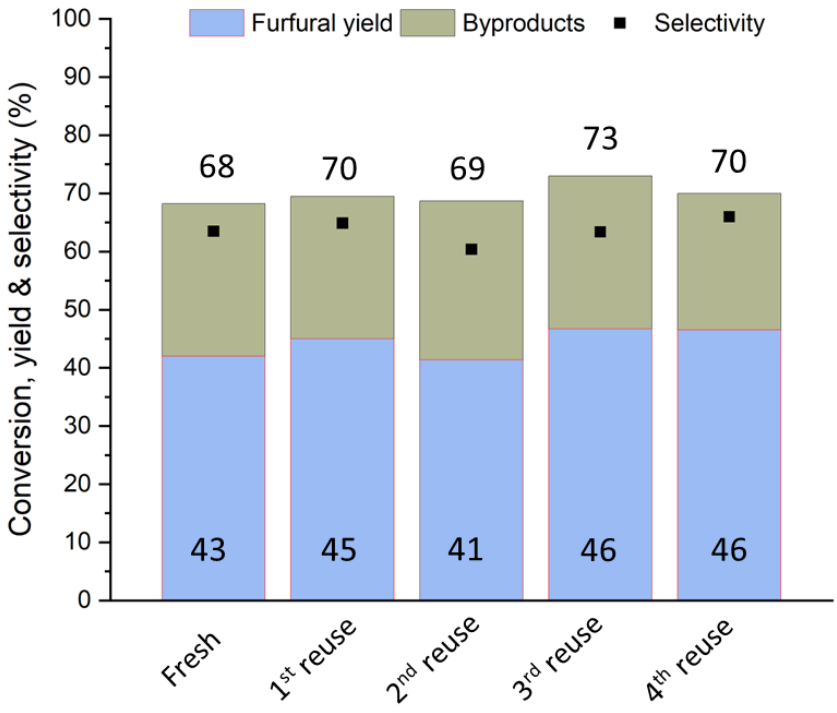

Figure 2.18. Reusability test of P-$CaNb_2O_6$. Reaction conditions are the same as **Figure 2.13**. Reused catalysts were calcined at 500 °C for 5 h in air before each reaction. Gray bars represent total yield of undetectable by-products including humin. The sum of the blue and gray bars means the xylose conversion.

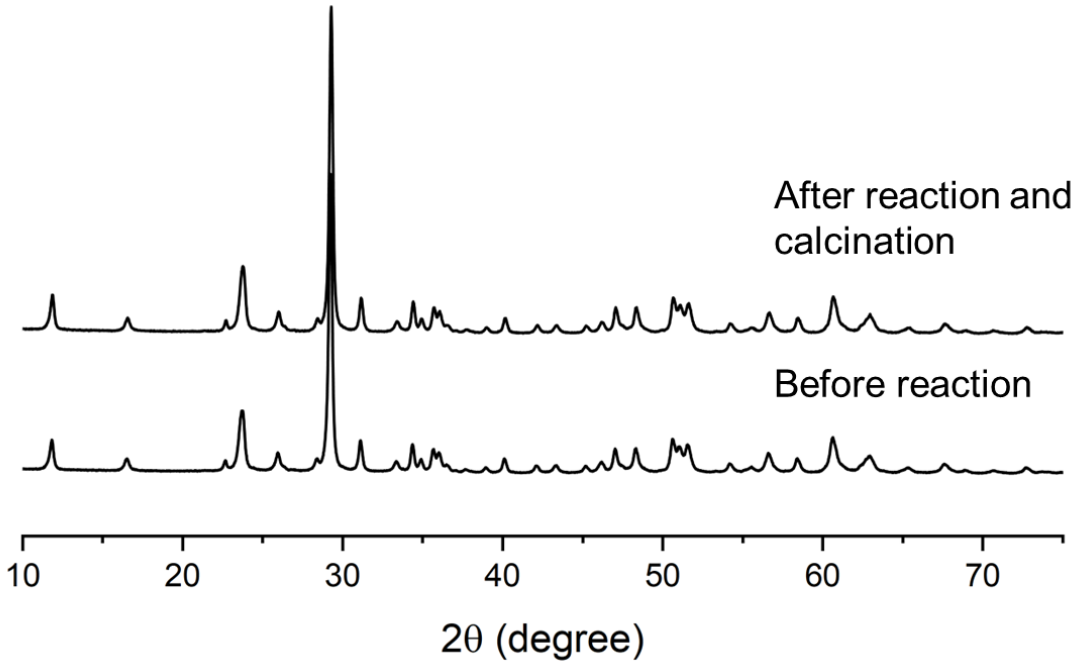

Figure 2.19. XRD patterns of $CaNb_2O_6$ before and after reaction.

2.4 Conclusions

Orthorhombic phosphate-modified $CaNb_2O_6$ (P-$CaNb_2O_6$) has been developed as an efficient catalyst for the dehydration of xylose to furfural. Surface characterization by in-situ IR spectroscopy using pyridine as a probe molecule revealed the formation of abundant and stronger Lewis acid sites (LAS) upon phosphate treatment (P-treatment). Phosphate treatment was shown to hydrolyze polarized Nb–O–Ca bonds, resulting in the formation of Ca–O–$PO(OH)_2$ surface species and coordinatively unsaturated Nb sites that enhance Lewis acid sites. This modification significantly improved furfural yield. P-$CaNb_2O_6$ demonstrated excellent thermal stability and reusability, maintaining high catalytic activity over at least five regeneration cycles without noticeable structural degradation, as confirmed by XRD analysis. The strategy of selecting appropriate metal oxide frameworks and modified surface properties via P-treatment provides a promising pathway for designing durable and high-performance catalysts for biomass conversion and other acid-catalyzed transformations.

2.5 References

[1] K. J. Yong, T. Y. Wu, C. B. T. L. Lee, Z. J. Lee, Q. Liu, J. M. Jahim, Q. Zhou, L. Zhang, *Biomass and Bioenergy* **2022**, *161*, 106458.

[2] P. Mäki-Arvela, T. Salmi, B. Holmbom, S. Willför, D. Yu. Murzin, *Chem. Rev.* **2011**, *111*, 5638–5666.

[3] D. S. Naidu, S. P. Hlangothi, M. J. John, *Carbohydrate Polymers* **2018**, *179*, 28–41.

[4] J. J. Bozell, G. R. Petersen, *Green Chem.* **2010**, *12*, 539.

[5] K. Yan, G. Wu, T. Lafleur, C. Jarvis, *Renewable and Sustainable Energy Reviews* **2014**, *38*, 663–676.

[6] C. B. T. L. Lee, T. Y. Wu, *Renewable and Sustainable Energy Reviews* **2021**, *137*, 110172.

[7] Z. Zhang, G. W. Huber, *Chem. Soc. Rev.* **2018**, *47*, 1351–1390.

[8] N. K. Gupta, A. Fukuoka, K. Nakajima, *ACS Catal.* **2017**, *7*, 2430–2436.

[9] K. Nakajima, Y. Baba, R. Noma, M. Kitano, J. N. Kondo, S. Hayashi, M. Hara, *J. Am. Chem. Soc.* **2011**, *133*, 4224–4227.

[10] K. Nakajima, R. Noma, M. Kitano, M. Hara, *Journal of Molecular Catalysis A: Chemical* **2014**, *388–389*, 100–105.

[11] K. Nakajima, R. Noma, M. Kitano, M. Hara, *J. Phys. Chem. C* **2013**, *117*, 16028–16033.

[12] R. Noma, K. Nakajima, K. Kamata, M. Kitano, S. Hayashi, M. Hara, *J. Phys. Chem. C* **2015**, *119*, 17117–17125.

[13] S. M. A. H. Siddiki, Md. N. Rashed, Md. A. Ali, T. Toyao, P. Hirunsit, M. Ehara, K. Shimizu, *ChemCatChem* **2019**, *11*, 383–396.

[14] M. Yang, S. Li, J. Huang, *ACS Appl. Mater. Interfaces* **2021**, *13*, 39501–39512.

[15] D. Padovan, K. Endo, T. Matsumoto, T. Yokoi, A. Fukuoka, H. Kato, K. Nakajima, *Small Structures* **2023**, *4*, 2200224.

[16] M. Kim, S. Ronchetti, B. Onida, N. Ichikuni, A. Fukuoka, H. Kato, K. Nakajima, *ChemCatChem* **2020**, *12*, 350–359.

[17] D. Dey, V. Petrykin, S. Sasaki, M. Kakihana, *J. Ceram. Soc. Japan* **2007**, *115*, 808–812.

[18] M. Kakihana, M. Kobayashi, K. Tomita, V. Petrykin, *Bulletin of the Chemical Society of Japan* **2010**, *83*, 1285–1308.

[19] M. Tamura, K. Shimizu, A. Satsuma, *Applied Catalysis A: General* **2012**, *433–434*, 135–145.

[20] M. I. Zaki, M. A. Hasan, F. A. Al-Sagheer, L. Pasupulety, *Colloids and Surfaces A: Physicochemical and Engineering Aspects* **2001**, *190*, 261–274.

[21] G. Busca, *Phys. Chem. Chem. Phys.* **1999**, *1*, 723–736.

[22] A. Travert, A. Vimont, A. Sahibed-Dine, M. Daturi, J.-C. Lavalley, *Applied Catalysis A: General* **2006**, *307*, 98–107.

[23] T. K. Phung, C. Herrera, M. Á. Larrubia, M. García-Diéguez, E. Finocchio, L. J. Alemany, G. Busca, *Applied Catalysis A: General* **2014**, *483*, 41–51.

[24] B. M. Matsagar, M. K. Munshi, A. A. Kelkar, P. L. Dhepe, *Catal. Sci. Technol.* **2015**, *5*, 5086–5090.

[25] B. M. Matsagar, S. A. Hossain, T. Islam, H. R. Alamri, Z. A. Alothman, Y. Yamauchi, P. L. Dhepe, K. C.-W. Wu, *Sci Rep* **2017**, *7*, 13508.

Chapter 3

Influence of Alkaline Earth Metal Type and Phosphate Modification on the Catalytic Activity of Niobates in Xylose Dehydration

Abstract

$CaNb_2O_6$, $SrNb_2O_6$, and $BaNb_2O_6$ were synthesized using an amorphous metal complex (AMC) method. This study explores phosphate-modified $CaNb_2O_6$, $SrNb_2O_6$, and $BaNb_2O_6$ catalysts to understand how alkaline earth metals affect acidity, basicity, and catalytic performance. Lewis acidity decreased and basicity increased from Ca to Ba. Phosphate treatment enhanced Lewis acid sites in P-$CaNb_2O_6$ by cleaving Nb–O–Ca bonds, while it suppressed strong basic sites in P-$SrNb_2O_6$ and P-$BaNb_2O_6$, improving selectivity. TOF and TON results showed P-$BaNb_2O_6$ ≈ P-$SrNb_2O_6$ > P-$CaNb_2O_6$. All catalysts showed stable performance and reusability over five cycles with minimal phosphate loss.

3.1 Introduction

$CaNb_2O_6$, as a complex metal oxide, has demonstrated great potential in the field of catalysis due to its unique crystal structure and physicochemical properties. In addition to its conventional role as a dielectric and optical material, it has recently emerged as a promising solid acid catalyst in the previous chapter.[7–10] Phosphate-modified $CaNb_2O_6$ (P-$CaNb_2O_6$) was developed as a stable and efficient catalyst for the dehydration of xylose to furfural. Structural characterization revealed that the introduction of phosphate molecules enhanced Lewis acid sites (LAS) while suppressing undesirable humin formation. Compared to Nb_2O_5, P-$CaNb_2O_6$ exhibited superior catalytic activity, higher furfural selectivity, and excellent thermal stability across multiple regeneration cycles. These results highlight the potential of metal oxide modification strategies for enhancing catalytic performance and lay the groundwork for further investigations into the incorporation of alkaline earth metals in crystalline Nb-based catalysts.[11–13]

However, other members of the alkaline earth metal family, such as Sr and Ba, exhibit significant differences in ionic radius, electronegativity, and electronic structure compared to Ca.[14] These differences may have important impacts on the crystal structure, surface acidity, and catalytic performance of niobates.[14–17] For instance, Mg, with its smaller ionic radius and higher electronegativity, may lead to the formation of different crystal phases and distributions of acid sites; whereas Ba, with its larger ionic radius, may cause lattice expansion, affecting the surface properties of the catalyst. According to the DFT calculations reported by Li *et al.*, the important role of the Lewis acid-base pair sites in anatase TiO_2 for the direct dehydration of glucose to HMF. This mechanism bypasses the isomerization to fructose and represents an efficient, green, and feasible new approach under aqueous conditions.[18] However, the effect of alkaline earth metal type on the

catalytic activity in xylose conversion has not been systematically studied to date. Moreover, P-treatment of complex metal oxides can reduce the catalyst's basicity and increase its acidity, thereby enhancing selectivity. Therefore, P-treatment offers certain advantages for complex metal oxide catalysts.[12,13]

Exploring the performance of $CaNb_2O_6$, $SrNb_2O_6$, and $BaNb_2O_6$, as well as their phosphate-modified counterparts as acid catalysts not only deepens the understanding of how alkaline earth metal substitution influences the crystal structure and acid characteristics of niobates but also holds the potential to identify superior catalytic systems. Systematic studies on the synthesis, structural characterization, and catalytic performance of different alkaline earth metal niobates are expected to elucidate the relationships among crystal structure, acidity characteristics, and catalytic activity, thereby providing a scientific basis for the design and optimization of efficient catalysts.

3.2 Experimental section

3.2.1 Chemical reagents

$NbCl_5$ was purchased from HIGH PURITY CHEMICALS. Hydrogen peroxide (30%~35%), phosphoric acid (>85%), toluene (>99.5%), chloroform (>99.0%), and Barium carbonate (>99.0%) were supplied by KANTO CHEMICAL CO., INC. Ammonia solution (28%), L-lactic acid, Calcium nitrate tetrahydrate (99.9%), strontium nitrate (98.0~102.0% mass/mass), D(+)-xylose, and pyridine (dehydrated) were obtained from FUJIFILM Wako Pure Chemical Corporation. Furfural (>98%) and chlorobenzene (>98%) were received by Tokyo Chemical Industry (TCI).

3.2.2 Catalysts preparation

$CaNb_2O_6$, $SrNb_2O_6$, and $BaNb_2O_6$ were synthesized as niobium-based complex metal oxide catalysts using the Amorphous Metal Complex (AMC) method.[19,20] Initially, 25 g of anhydrous $NbCl_5$ was gradually added to a beaker containing 300 mL of distilled water. The pH of the mixture was then adjusted to 7 using ammonia water, and the solution was stirred at 600 rpm for 3 hours. After confirming the pH remained at 7, the precipitate was thoroughly washed with distilled water over 20 cycles to remove Cl^- ions, resulting in a white $NbO_x \cdot mH_2O$ precipitate. A portion of $NbO_x \cdot mH_2O$ was calcined at 1000 °C for 10 hours to verify the niobium content.

Subsequently, $Nb(CH_3CH(OH)COO)(CH_3CH(O)COO)_2$ (referred to as Nb-La) was prepared by adding 80 mmol lactic acid and 200 mmol hydrogen peroxide relative to 20 mmol $NbO_x \cdot mH_2O$ to the precipitate. The pH was adjusted to 4.5 with ammonia water, and the mixture was stirred at 240 rpm and 60 °C for one hour before being heated to 90 °C overnight to obtain a yellow solid. This solid was then diluted with a measured amount of distilled water to produce Nb-La.

To synthesize $CaNb_2O_6$, 10 mmol calcium nitrate tetrahydrate was dissolved by adding three equivalent moles of lactic acid relative to the calcium nitrate tetrahydrate, followed by sonication until complete dissolution. Two molar equivalents of Nb-La were then added to the solution. The mixture was dried by heating below 100 °C to form a powder, which subsequently stabilized at 250 °C for 1 hour, gradually increased to 450 °C for 3 hours, and finally calcined in a muffle furnace at 700 °C for 5 hours to obtain $CaNb_2O_6$. The synthesis of T-phase Nb_2O_5 followed an identical procedure: Nb-La was added to a beaker, heated below 100 °C to form a powder, stabilized at 250 °C for 1 hour, increased to 450 °C for 3 hours, and finally calcined at 700 °C for 5 hours.

Phosphate treatment of $CaNb_2O_6$ and Nb_2O_5 involved adding 1 g of catalyst to 200 mL of 1 M phosphoric acid solution and stirring at 500 rpm at room temperature for two days. The catalysts were then washed and filtered four times, dried overnight in an oven, and labeled as P-$CaNb_2O_6$ and P-Nb_2O_5. The synthesis of $SrNb_2O_6$ and $BaNb_2O_6$ followed the same procedure, substituting strontium nitrate and barium carbonate for calcium nitrate tetrahydrate, respectively.

3.2.3 Characterization

X-ray diffraction (XRD) analysis was conducted using an Ultima IV Rigaku diffractometer operating at 40 kV and 40 mA with Cu Kα radiation (λ = 1.5418 Å) over a 2θ range of 10° to 80°. Nitrogen adsorption measurements were carried out on a Micromeritics 3-Flex instrument at 77 K, with samples being degassed at 150 °C for one hour prior to analysis. Brunauer-Emmett-Teller (BET) surface areas were calculated within a relative pressure (P/P_0) range of 0.05 to 0.30. X-ray photoelectron spectroscopy (XPS) was performed using a JEOL JPS-9010MC system, and data were analyzed with CasaXPS software. Fourier Transform Infrared (FTIR) spectroscopy was executed on a JASCO FT/IR-4100 spectrometer equipped with a cooled mercury cadmium telluride detector. Catalyst disks (20 mm diameter, 40–90 mg) were placed in an IR cell connected to a closed-loop circulation system and outgassed under vacuum at 300 °C for one hour prior to measurement. Pyridine and chloroform were utilized as probe molecules to assess acidity and basicity, respectively. Thermogravimetric analysis (TGA) was conducted on a Rigaku Thermo plus Evo2 instrument, where samples (10 mg) were heated from 30 °C to 800 °C at a rate of 10 °C per minute under a constant airflow of 50 $mL \cdot min^{-1}$.

3.2.4 Furfural production from xylose dehydration

The catalytic reactions were conducted in a pressure-resistant spherical glass reactor. Each reaction system comprised a biphasic mixture of 75 mg xylose in 2 mL aqueous solution and 8 mL toluene, combined with 300 mg of catalyst. The reactions were maintained for five hours in an oil bath set at 120 °C. Upon completion, the reactor was rapidly cooled in an ice bath, and the reaction mixture was separated by centrifugation. The aqueous phase was analyzed using a Shimadzu LC-2030C Plus high-performance liquid chromatograph with a mobile phase of 5 mmol L^{-1} sulfuric acid. Reactants were separated on a BIO-RAD Aminex HPX-87H column and detected using a refractive index detector (RID-20A) and an ultraviolet detector set at 245 nm. The organic phase was quantified by adding chlorobenzene as an internal standard and analyzed using a Shimadzu GC-2025AF gas chromatograph equipped with a flame ionization detector (FID). Conversion, yields, selectivity, turnover frequency (TOF) and turnover number (TON) were calculated based on the following equations. In this study, the detectable product is limited only to furfural, meaning that by-products are defined as “humin-type undetectable species”.

For reuse experiments, a similar biphasic system containing 75 mg xylose in 2 mL aqueous solution and 8 mL toluene was employed with 300 mg of P-$CaNb_2O_6$ as the catalyst. The reaction conditions were identical, running for five hours at 120 °C. After each reaction cycle, the catalyst was separated by centrifugation, washed twice, dried overnight at 110°C, and then calcined for five hours in a muffle oven at 500°C. The regenerated catalyst was ground for five minutes to prepare for the next cycle, with a total of five consecutive reactions performed. 300 mg of P-$SrNb_2O_6$, and P-$BaNb_2O_6$ underwent five consecutive reactions under identical conditions. For the phosphorus

leaching test, a similar biphasic system comprising 75 mg of xylose in 2 mL of aqueous solution and 8 mL of toluene was utilized with 300 mg of P-$CaNb_2O_6$, P-$SrNb_2O_6$ and P-$BaNb_2O_6$ as the catalyst. The reaction was conducted for one hour, after which the catalysts were removed. The reaction solution was retained in the reactor and allowed to proceed for an additional four hours.

$$\boldsymbol{Conversion} = \mathbf{100\%} * \frac{\boldsymbol{Moles\ of\ xylose_{initial} - Moles\ of\ xylose_{final}}}{\boldsymbol{Moles\ of\ xylose_{initial}}} \quad \textit{(1)}$$

$$\boldsymbol{Yield_{fufural}} = \mathbf{100\%} * \frac{\boldsymbol{Moles\ of\ furfural_{final}}}{\boldsymbol{Moles\ of\ xylose_{initial}}} \quad \textit{(2)}$$

$$\boldsymbol{Yield_{by-products}} = \boldsymbol{Moles\ of\ xylose_{initial}} - \boldsymbol{Yield_{fufural}} \quad \textit{(3)}$$

$$\boldsymbol{Selectivity_{furfural}} = \mathbf{100\%} * \frac{\boldsymbol{Yield_{fufural}}}{\boldsymbol{Conversion}} \quad \textit{(4)}$$

$$\boldsymbol{TOF_{furfural}} = \frac{\boldsymbol{Moles\ of\ furfural_{final}}}{\boldsymbol{Lewis\ acid\ amount{*}hour}} \quad \textit{(5)}$$

$$\boldsymbol{TON_{furfural}} = \frac{\boldsymbol{Moles\ of\ furfural_{final}}}{\boldsymbol{Lewis\ acid\ amount}} \quad \textit{(6)}$$

3.3 Results and discussion

3.3.1 Physical properties of $CaNb_2O_6$, $SrNb_2O_6$, and $BaNb_2O_6$ before and after phosphate treatment

$CaNb_2O_6$, $SrNb_2O_6$, and $BaNb_2O_6$ were synthesized using the AMC method, analogous to $CaNb_2O_6$, and characterized by X-ray diffraction (XRD) as illustrated in **Figures 3.1 and 3.2** Among these compounds, $CaNb_2O_6$ (ICDD: 01-071-2406) and $BaNb_2O_6$ (ICDD: 01-077-0589) exhibit orthorhombic crystal structures, whereas $SrNb_2O_6$ (ICDD: 01-072-2088) adopts a monoclinic structure. In contrast, $MgNb_2O_6$ tends to form multiple crystal phases rather than a single orthorhombic phase ($MgNb_2O_6$ ICDD: 00-033-0875). At 700 °C, characteristic peaks of the T-phase Nb_2O_5 remain observable and persist until approximately 900 °C, beyond which they largely disappear. However, starting at 800 °C, peaks corresponding to $Mg_4Nb_2O_9$ gradually emerged.[21] These impurity peaks significantly hinder further investigations into the catalyst application. Additionally, $MgNb_2O_6$ calcined at 700, 800, and 900 °C does not exhibit any apparent advantages in reaction performance under identical conditions compared to other catalysts and was thus not pursued further. No differences were observed in the catalysts before and after P-treatment. **Table 3.1** lists the BET specific surface areas measured by nitrogen physisorption before and after P-treatment for $CaNb_2O_6$, $SrNb_2O_6$, and $BaNb_2O_6$, which showed no significant changes, with values of 23, 17, and 8 $m^2 g^{-1}$, respectively. Nb_2O_5 exhibits a specific surface area of approximately 9 $m^2 g^{-1}$, similar to that of $BaNb_2O_6$. The surface phosphorus elemental ratios of the catalysts were determined using high-resolution XPS (**Figure 3.3**). The phosphate contents of $CaNb_2O_6$, $SrNb_2O_6$, $BaNb_2O_6$ and Nb_2O_5 were 2.6, 2.9, 3.1 and 3.9 atom%, respectively.

$SrNb_2O_6$ and $BaNb_2O_6$ share the same structural composition as $CaNb_2O_6$, specifically the edge-sharing arrangement of NbO_6 octahedra and MO_8 polyhedra (M = Ca, Sr and Ba) (**Figure 3.4**). However, $BaNb_2O_6$ exhibits edge-sharing with at least four NbO_6 octahedra, whereas $SrNb_2O_6$ and $CaNb_2O_6$ engage in edge-sharing with a maximum of two NbO_6 octahedra.[22] According to Pauling's third rule, edge and face-sharing polyhedra bring cations into closer proximity, thereby increasing cation-cation electrostatic repulsion.[23,24] Consequently, the polyhedra in $BaNb_2O_6$ may be less stable than those in $SrNb_2O_6$ and $CaNb_2O_6$. The ionic radii of Ca^{2+}, Sr^{2+}, and Ba^{2+} with a coordination number of eight increase in the order $Ca^{2+} < Sr^{2+} < Ba^{2+}$, with values of 1.18, 1.31, and 1.47 Å, respectively.[25,26] In accordance with Pauling's rules, electrostatic repulsion among neighboring cations influences the bond lengths between these cations and oxygen atoms coordinated to alkali earth metals. Larger ionic radii result in longer M–O bond lengths, thereby affecting the electron density distribution.[27–30] Among Ca^{2+}, Sr^{2+}, and Ba^{2+} in the same oxidation state, smaller cations possess higher charge densities and induce stronger polarization of neighboring oxygen ions. In particular, Ca^{2+} more strongly attracts the electron cloud of oxygen, reducing its electron density. Therefore, based on the crystal structure and ionic radii of the catalysts, the electron density of oxygen ions in $CaNb_2O_6$ is expected to be the lowest, diminishing its electron-donating capacity and resulting in the weakest Lewis basicity theoretically. Conversely, $SrNb_2O_6$ exhibits intermediate Lewis basicity, while $BaNb_2O_6$ displays the strongest. To validate this trend, the acid and base properties of the catalysts were investigated using FTIRwith $CHCl_3$ and pyridine as probe molecules.

Table 3.1. Surface properties of the complex metal oxides before and after P-treatment.

Catalyst	Surface area (m^2 g^{-1})[a]	Lewis acid sites (μmol g^{-1})[b]	Brønsted acid sites (μmol g^{-1})[b]	Surface P ratio (atom%)[c]
P-$CaNb_2O_6$	23	37	10	2.6
$CaNb_2O_6$	23	32	<10	-
P-$SrNb_2O_6$	17	21	<10	2.9
$SrNb_2O_6$	16	29	<10	-
P-$BaNb_2O_6$	8	22	<10	3.1
$BaNb_2O_6$	8	34	<10	-
P-Nb_2O_5	9	14	<10	3.9
Nb_2O_5	9	23	<10	-

Determined by [a] N_2 adsorption, [b] FTIR-pyridine adsorption and [c] XPS.

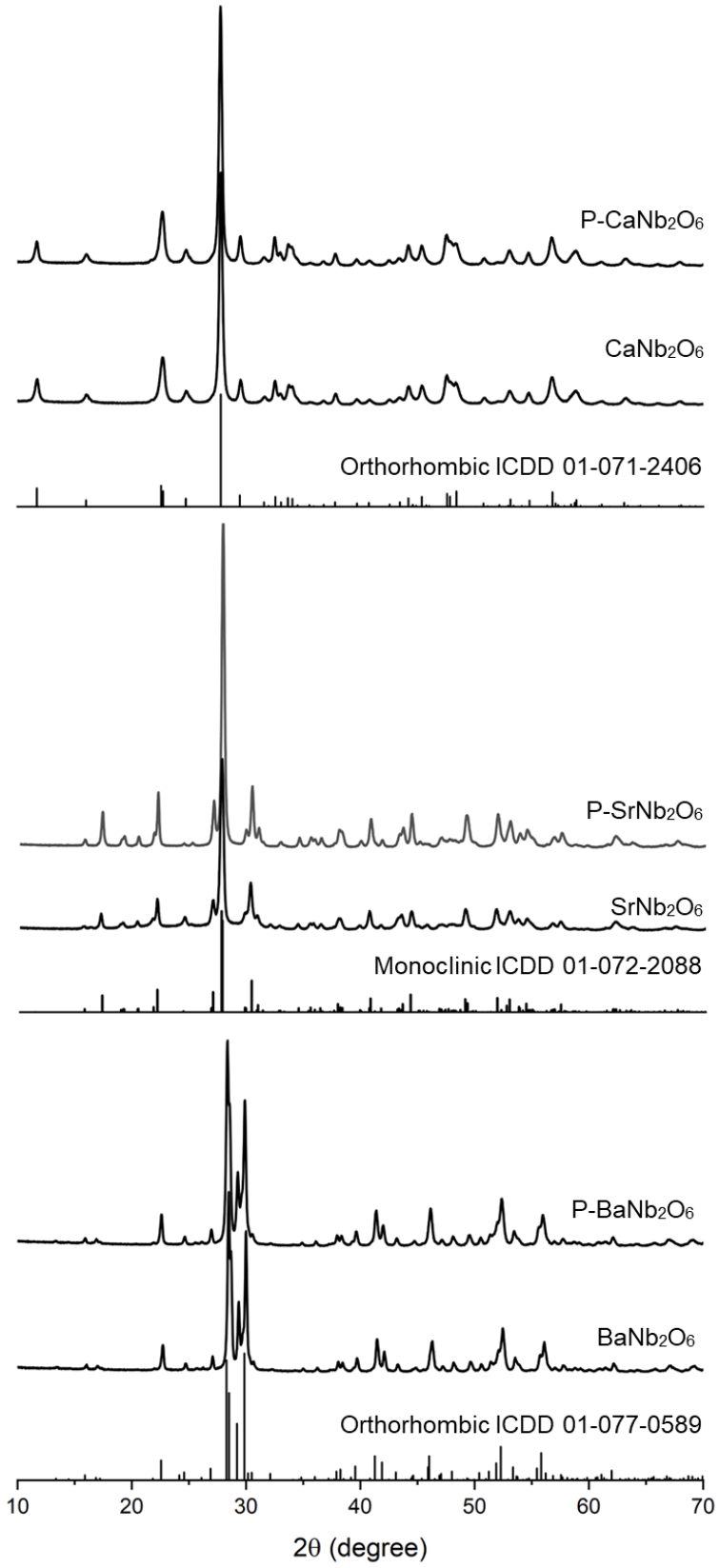

Figure 3.1. XRD patterns of complex metal oxides before and after P-treatment.

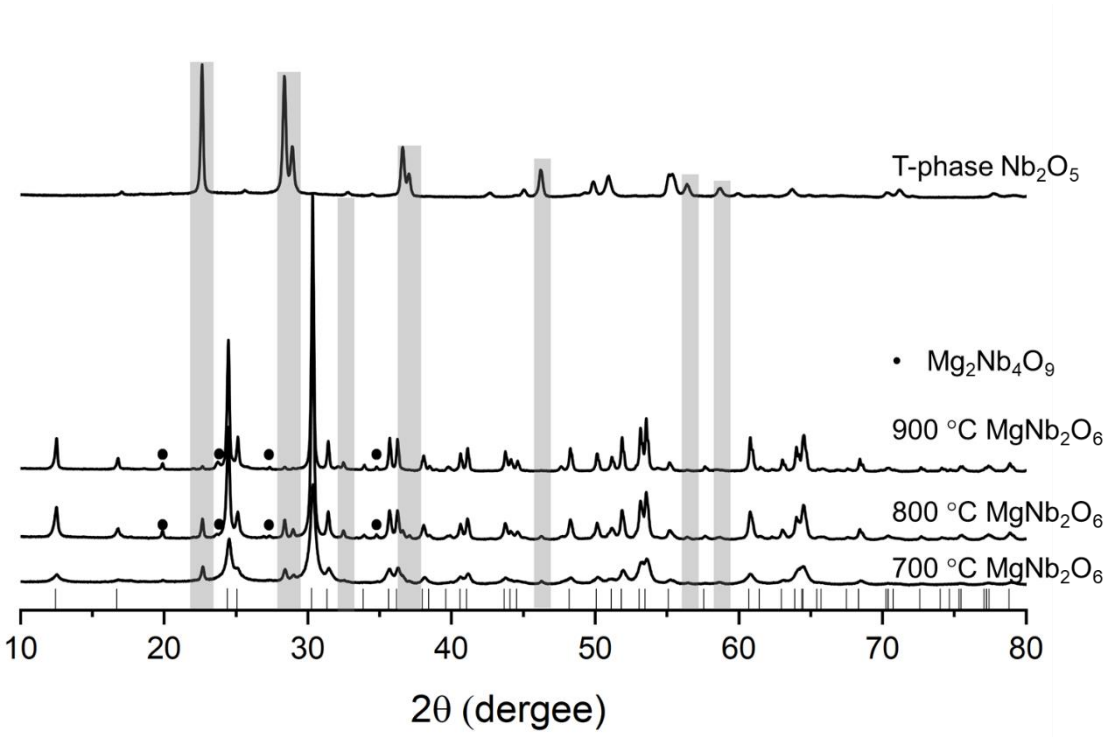

Figure 3.2. XRD patterns of $MgNb_2O_6$ calcinated at different temperatures.

A: P-$CaNb_2O_6$

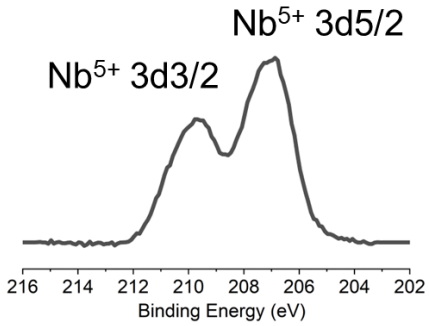

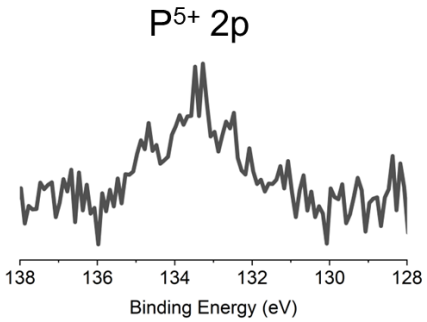

B: P-$SrNb_2O_6$

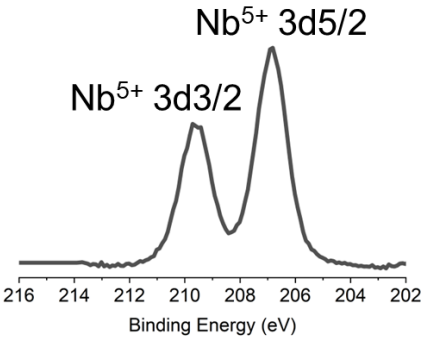

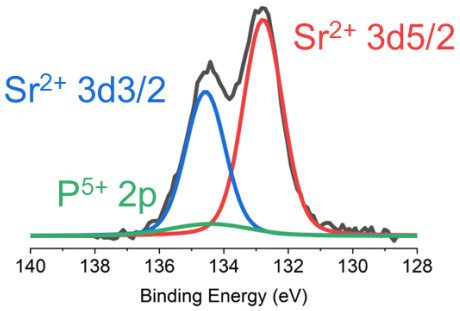

C: P-$BaNb_2O_6$

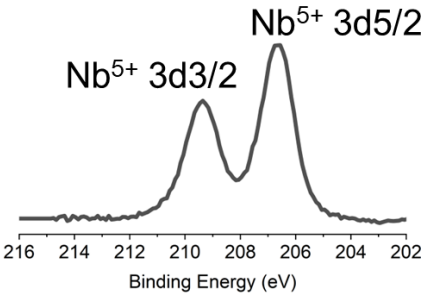

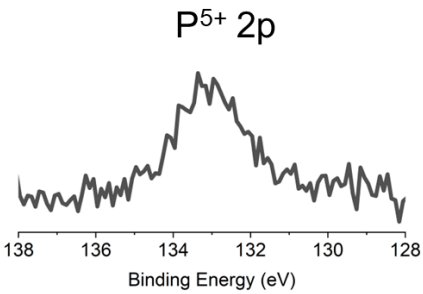

Figure 3.3. XPS data of (A) P-$CaNb_2O_6$ and (B) P-$SrNb_2O_6$ and (C) P-$BaNb_2O_6$.

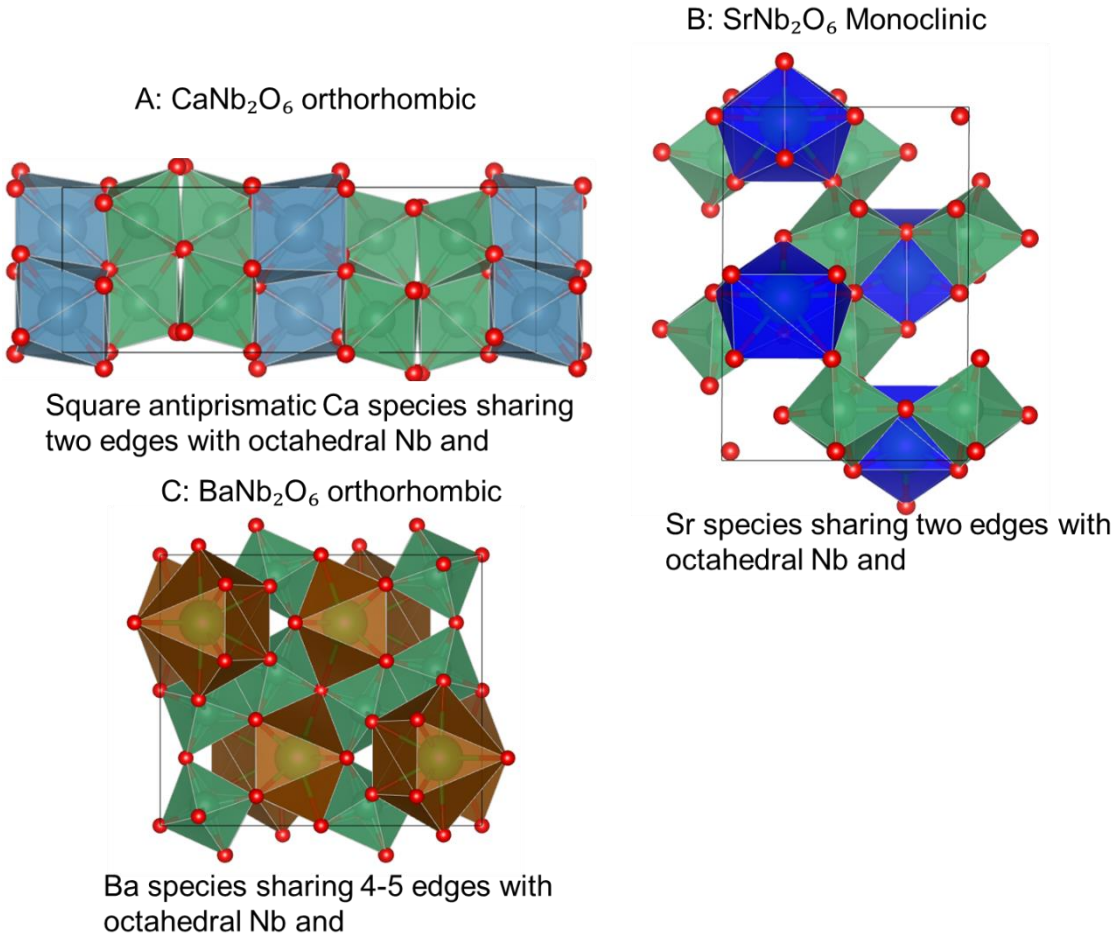

Figure 3.4. Crystalline structures of (A) $CaNb_2O_6$ (Red balls, green polygon and light blue polygon are oxygen, octahedral NbO_6 and CaO_8, respectively), (B) $SrNb_2O_6$ (Blue polygon is SrO_8) and (C) $BaNb_2O_6$ (Brown polygon is BaO_8).

3.3.2 Acidic properties of complex metal oxide catalysts by pyridine adsorption

FTIR analysis of pyridine adsorption on different catalyst surfaces is widely used to distinguish between BAS and LAS. **Figure 3.5** presents the FTIR spectra of pyridine adsorbed $CaNb_2O_6$, $SrNb_2O_6$, $BaNb_2O_6$ and Nb_2O_5 before and after P-treatment. Initially, all catalysts exhibited characteristic peaks of LAS (1444 cm^{-1}), confirming the presence of Lewis acid sites. Notably, $SrNb_2O_6$, $BaNb_2O_6$ and Nb_2O_5 exhibit almost no BAS (1540

cm^{-1}) before and after P-treatment, whereas $CaNb_2O_6$ displays characteristic peaks indicating a small number of BAS.[10,32–34] The specific values for LAS and BAS are summarized in **Table 3.1**. However, the number of LAS do not exhibit systematic variation and remains relatively similar ($CaNb_2O_6$: 32 μmol g^{-1}, $SrNb_2O_6$: 29 μmol g^{-1}, $BaNb_2O_6$: 34 μmol g^{-1}). After P-treatment, each catalyst displays different trends: P-$CaNb_2O_6$ shows a slight increase in the number of LAS (from 32 to 37 μmol g^{-1}), while P-$SrNb_2O_6$, P-$BaNb_2O_6$ and P-Nb_2O_5 experience a decrease in LAS density. Additionally, the bands around 1600 cm^{-1}, known as sensitive vibrational modes, influenced by metal type, coordination environment, and acid strength, reveal further differences.[35] All complex metal oxides display double peaks in this region, with the 1605 cm^{-1} band corresponding to pyridine coordinated to LAS in Nb_2O_5 (**Figure 3.5**). For all complex metal oxides, differences in the coordination environments, such as Nb–O–Nb versus Nb–O–M (e.g., Nb–O–Ca), suggest that the two observed bands can be attributed to distinct types of LASs.

Since liquid-phase pyridine exhibits a characteristic vibrational band at 1580 cm^{-1}, any shift to higher wavenumbers indicates stronger interactions with Lewis acid sites (LAS). For P-$CaNb_2O_6$, P-$SrNb_2O_6$, and P-$BaNb_2O_6$, distinct peaks were observed around 1600 cm^{-1}, corresponding to different types of LAS, as shown in **Figure 3.5**. The peaks at 1602, 1596, and 1594 cm^{-1} exhibit a clear trend that aligns with the periodic properties of Ca, Sr, and Ba, such as ionic radius and electronegativity. These bands are therefore attributed to Nb–O–M bonds (M = Ca, Sr, Ba). The types of LAS in these catalysts are illustrated in **Figure 3.6**.

FTIR analysis using pyridine adsorption revealed rich information about the catalysts, which is discussed individually below. In $CaNb_2O_6$, the bands at 1608 and

1602 cm^{-1} correspond to Nb–O–Nb and Nb–O–Ca, respectively. Deconvolution of these peaks reveals the changes before and after phosphate treatment. All results are summarized in **Table 3.2**. Although the total LAS amount in $CaNb_2O_6$ increased slightly, the enhancement was primarily in the 1602 cm^{-1} band (Nb–O–Ca), which doubled from 5.4 μmol g^{-1} to 11.9 μmol g^{-1}. The area ratio between the 1608 and 1602 cm^{-1} peaks shifted from 3.0 to 1.3 after treatment. XRD comparison with the ICDD database (01-071-2406) showed that the peak at 58.88° corresponding to the (8,2,0) plane was significantly intensified, suggesting this may be the dominant exposed facet. **Figure 3.7** indicates this surface is rich in Nb–O–Ca sites. It is speculated that the strong polarization ability of Ca^{2+} causes asymmetric electron density distribution in Nb–O–Ca, weakening the Nb–O bond. Upon phosphate loading, this weakened bond cleaves more readily, exposing unsaturated Nb atoms as LAS, thus increasing the overall LAS density.

For P-$SrNb_2O_6$, the bands at 1606 and 1596 cm^{-1} represent Nb–O–Nb and Nb–O–Sr, respectively (**Figure 3.6**). Deconvolution before and after phosphate treatment shows a significant reduction in the 1596 cm^{-1} band, dropping from 10.5 to 5.7 μmol g^{-1} (**Table 3.2**). XRD analysis revealed an increase in intensity at 53.88°, attributed to the (−1,1,6) plane, which is likely the exposed facet (**Figure 3.7**), dominated by Nb–O–Sr. In contrast to P-$CaNb_2O_6$, P-$SrNb_2O_6$ showed a reduction in total LAS from 29 to 21 μmol g^{-1}. This is attributed to Sr's weaker polarization ability compared to Ca, leading to a more stable Nb–O–Sr bond that resists cleavage. Excess phosphate groups coordinate with unsaturated Nb sites and surface hydroxyls, thereby passivating LAS.

In P-$BaNb_2O_6$, the peaks at 1606 and 1594 cm^{-1} correspond to Nb–O–Nb and Nb–O–Ba, respectively (**Figure 3.6**). Deconvolution showed the 1606 cm^{-1} peak intensity halved, decreasing from 14.6 to 7.3 μmol g^{-1}, while total LAS dropped from 34 to

22 μmol g^{-1} (**Table 3.2**). XRD analysis identified 34.11° as the likely exposed facet, corresponding to the (0,4,2) plane, which is primarily composed of Nb–O–Nb groups at the surface and Nb–O–Ba layers beneath (**Figure 3.7**). Upon phosphate treatment, phosphate groups tend to coordinate with surface Nb atoms, passivating the LAS and reducing total acidity. This result is consistent with the observations for P-Nb_2O_5. A summary of phosphate treatment effects on all catalysts is presented in **Figure 3.8**. $CaNb_2O_6$ shows an increase in LAS after P-treatment due to cleavage of Ca–O–Nb bonds and exposure of unsaturated Nb sites. In contrast, $SrNb_2O_6$ and $BaNb_2O_6$ exhibit a decrease in LAS after P-treatment, as phosphate species tend to form stable P–O–Nb linkages that mask the Nb centers.

Table 3.2. Lewis acid properties and peak deconvolution results around 1600 cm^{-1}

Catalyst	Total Lewis acid amount (μmol g^{-1})[a]	Nb-O-Nb (μmol g^{-1})[a]	Nb-O-M (M: Ca, Sr, Ba) (μmol g^{-1})[a]	Ratio (Nb-O-Nb/Nb-O-M)
P-$CaNb_2O_6$	37	23.3	13.7	1.3
$CaNb_2O_6$	32	24	8	3
P-$SrNb_2O_6$	21	14	7	2.0
$SrNb_2O_6$	29	15.8	13.2	1.2
P-$BaNb_2O_6$	22	7.6	14.4	0.5
$BaNb_2O_6$	34	16.2	17.8	0.9

Determined by [a] FTIR pyridine adsorption,

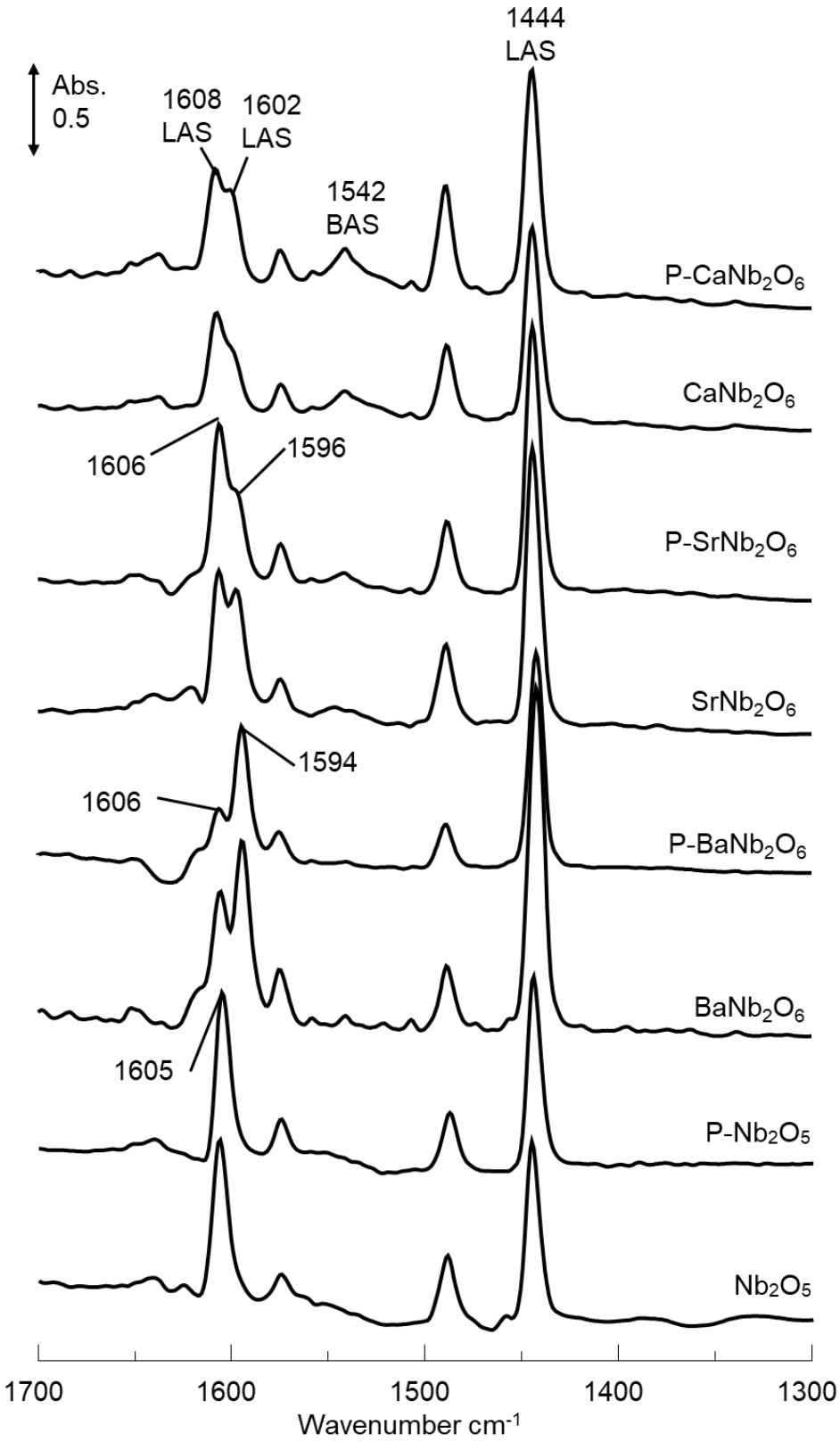

Figure 3.5. FTIR pyridine adsorption of P-$CaNb_2O_6$, $CaNb_2O_6$, P-$SrNb_2O_6$, $SrNb_2O_6$, P-$BaNb_2O_6$ and $BaNb_2O_6$.

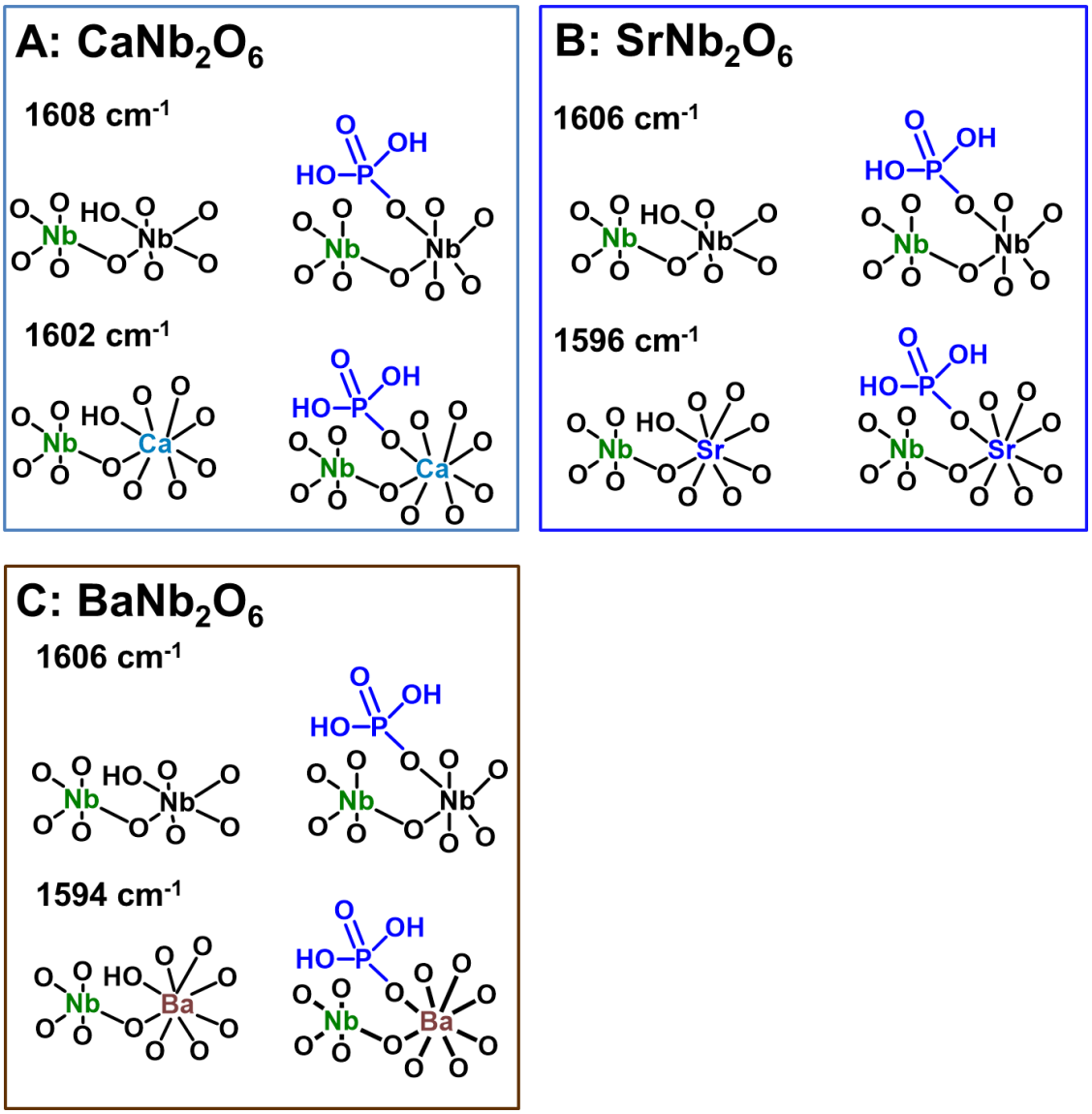

Figure 3.6. Possible LAS types around 1600 cm^{-1} for all catalysts: (A) P-$CaNb_2O_6$, (B) P-$SrNb_2O_6$ and (C) P-$BaNb_2O_6$.

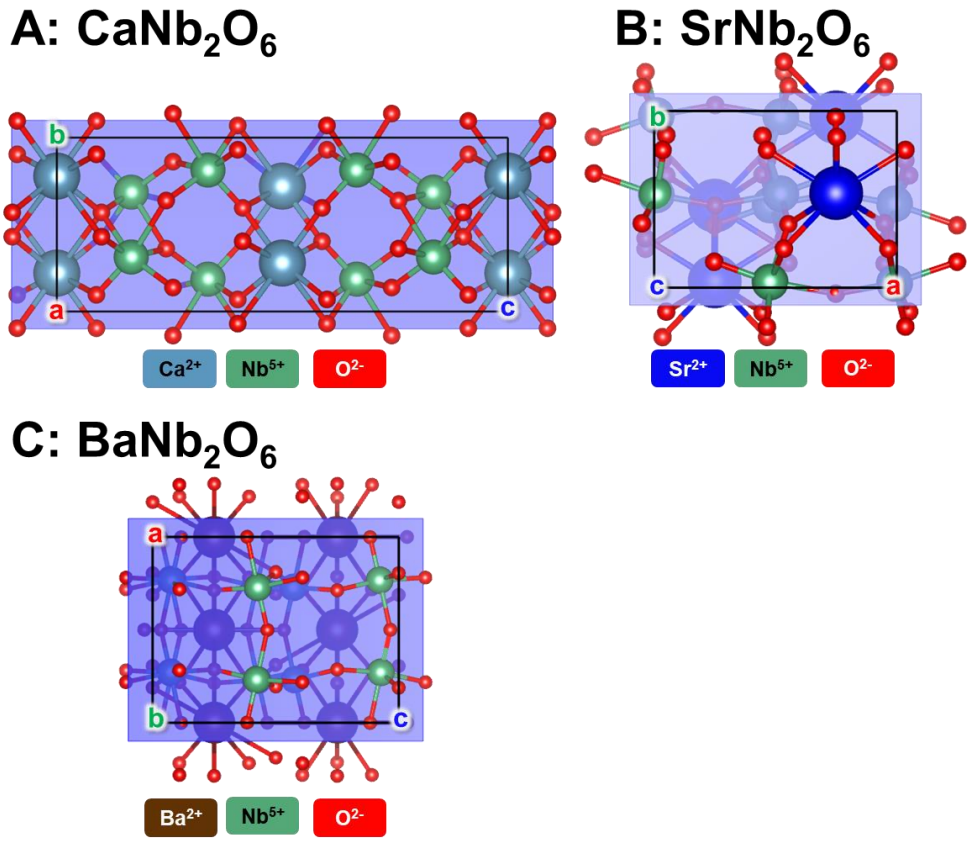

Figure 3.7. Types of LAS on exposed crystal facets of all catalysts: (A) P-$CaNb_2O_6$, (B) P-$SrNb_2O_6$, (C) P-$BaNb_2O_6$.

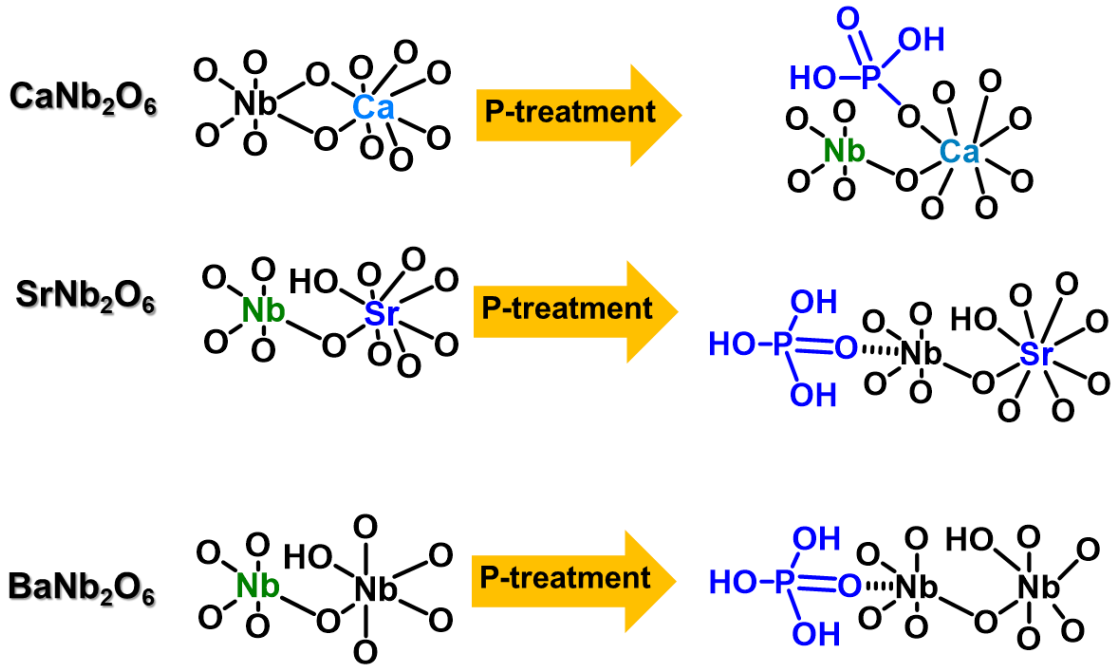

Figure 3.8. Main changes in LAS of all catalysts after phosphate treatment

3.3.3 Basic properties of complex metal oxide catalysts by $CHCl_3$ adsorption

When combined with P-treatment, the basicity of these complex metal oxide catalysts undergoes significant alterations. **Figure 3.9** presents the FTIR spectra of $CHCl_3$-adsored $CaNb_2O_6$, $SrNb_2O_6$, and $BaNb_2O_6$ before and after P-treatment. Due to the high polarity of $CHCl_3$, its hydrogen atoms exhibit a degree of acidity, making $CHCl_3$ an effective basic probe molecule.[31] $BaNb_2O_6$ possesses the highest basicity, as indicated by the largest red shift of the C–H vibrational absorption peak to 3008 cm^{-1}, followed by $SrNb_2O_6$ (3015 cm^{-1}) and $CaNb_2O_6$ (3019 cm^{-1}). This observation is consistent with the structural characteristics discussed in **Figure 3.4**. After P-treatment, all catalysts exhibited a comparable decrease in basicity. This consistent shift is attributed to the occupation of oxygen unsaturated sites by phosphate molecules, which reduces the electron density of surface oxygen atoms. Specifically, the peak for $SrNb_2O_6$ from 3015 to 3019 cm^{-1}, and $BaNb_2O_6$ from 3008 to 3012 cm^{-1}. These results indicate that the comparable shift in FTIR adsorption bands across P-$CaNb_2O_6$, P-$SrNb_2O_6$, and P-$BaNb_2O_6$ suggests that phosphate modification led to a similar extent of basicity reduction. However, the basic strength followed the same trend as in the unmodified samples. Nb_2O_5, generally not regarded as a strongly basic catalyst, exhibited negligible shift after P-treatment (3018 to 3019 cm^{-1}), suggesting that the phosphate groups introduced onto the Nb_2O_5 surface primarily interact with Lewis acid sites, as discussed in Chapter 2, rather than suppressing basicity. Metal oxides with strong and medium basicity reported in the literature, such as CeO_2 (2966 cm^{-1}), MgO (2979 cm^{-1}), Y_2O_3 (2986 cm^{-1}), Al_2O_3 (2991 cm^{-1}), TiO_2 (3003 cm^{-1}), and ZrO_2 (3008 cm^{-1}),[32] have C–H vibrational absorption peaks in the range of 2966 to 3008 cm^{-1}. Our metal oxide catalysts with weak basicity in the

range of 3008 to 3022 cm^{-1} contain both LAS and weak LBS (Lewis base sites) acting synergistically.

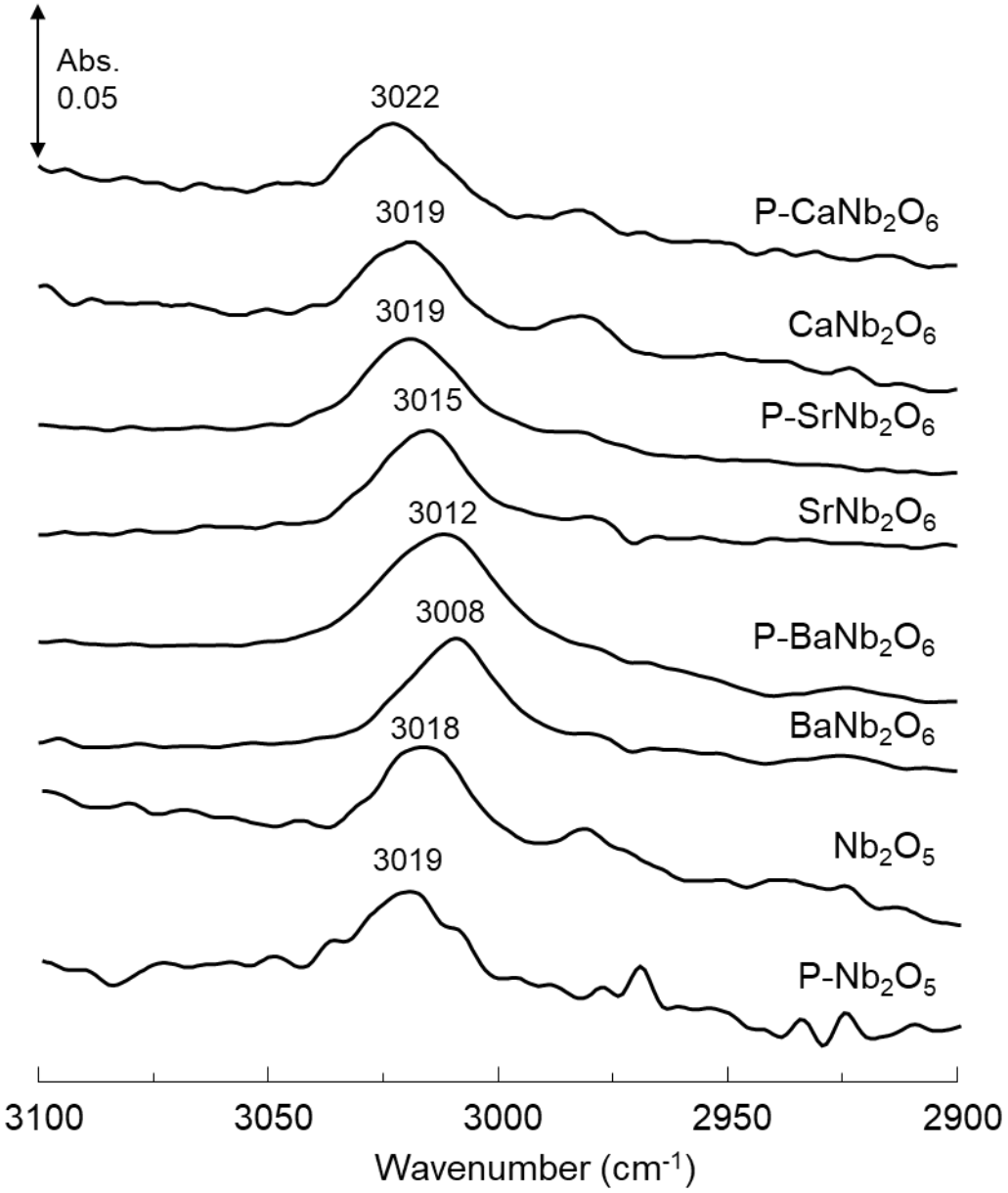

Figure 3.9. FTIR spectra of $CHCl_3$ adsorbed on P-$CaNb_2O_6$, $CaNb_2O_6$, P-$SrNb_2O_6$, $SrNb_2O_6$, P-$BaNb_2O_6$, $BaNb_2O_6$, Nb_2O_5 and P-Nb_2O_5.

3.3.4 Catalytic performance for furfural production

All catalysts were evaluated for converting xylose to furfural. All reactions were conducted in a glass round-bottom reactor containing both an aqueous phase and a toluene organic phase. As shown in **Figure 3.10**, the conversion for $CaNb_2O_6$, $SrNb_2O_6$, and $BaNb_2O_6$ were 72%, 70%, and 59%, respectively. However, selectivity was significantly enhanced due to the increased furfural yield after P-treatment. Another set of control experiments using CaO, SrO and BaO as the catalyst for xylose conversion achieved > 95%, but selectivity approached zero. As representative basic catalysts, CaO, SrO and BaO were unselective for this reaction. Although LAS promote furfural production, LBS are unable to dehydrate xylose effectively to furfural.[36–39] Based on the quantity of Lewis acid sites, the turnover frequency (TOF, after 1-hour reaction) and turnover number (TON, after 5-hour reaction) for P-$CaNb_2O_6$, P-$SrNb_2O_6$, and P-$BaNb_2O_6$ were calculated and summarized in **Table 3.3**. The results revealed a clearer trend: TOF and TON followed the order P-$CaNb_2O_6$ < P-$SrNb_2O_6$ ≈ P-$BaNb_2O_6$, suggesting that P-$CaNb_2O_6$ undergoes faster deactivation. This difference is attributed to the distinct types of Lewis acid sites present in each catalyst. While P-$BaNb_2O_6$ theoretically possesses the highest catalytic potential due to its larger number of acid sites, its performance is limited by its relatively low specific surface area.

Although the catalytic performance of P-$CaNb_2O_6$, P-$SrNb_2O_6$, and P-$BaNb_2O_6$ appear comparable, the number of acid sites in P-$SrNb_2O_6$ and P-$BaNb_2O_6$ is lower than that in P-$CaNb_2O_6$. Considering that CaO, SrO, and BaO are known to facilitate xylose conversion, it is reasonable to infer that LBS may also contribute to the catalytic activity.[36] Therefore, when evaluating both the potential higher intrinsic activity of the acid sites in P-$SrNb_2O_6$ and P-$BaNb_2O_6$ and the role of LBS, a plausible reaction scenario for the

three catalysts is proposed and summarized in the **Figure 3.11**. In the case of $CaNb_2O_6$, which possesses minimal basicity, the enhanced catalytic activity is attributed to the phosphate treatment-induced cleavage of Nb–O bonds within Nb–O–Ca linkages, leading to the exposure of unsaturated Nb species that serve as new Lewis acid sites. Conversely, $SrNb_2O_6$ and $BaNb_2O_6$ exhibit moderate intrinsic basicity. Although their Lewis acid site density decreased after phosphate treatment, a significant reduction in the stronger LBS was also observed. This suggests that the improved catalytic activity in P-$SrNb_2O_6$ and P-$BaNb_2O_6$ may result from the passivation of strong LBS, thereby suppressing undesired side reactions during xylose conversion.

Figure 3.12 illustrates the reaction time curves of P-$CaNb_2O_6$, P-$SrNb_2O_6$, and P-$BaNb_2O_6$. Among them, P-$SrNb_2O_6$ exhibited the highest initial reaction rate. However, as the reaction proceeded, the formation of side products and humin caused progressive catalyst deactivation, leading to a decrease in reaction rate. P-$CaNb_2O_6$, P-$SrNb_2O_6$, and P-$BaNb_2O_6$ exhibited comparable initial reaction rates during the early stage of the xylose dehydration reaction, suggesting that the intrinsic activity of the active sites was similar across the series. However, in all cases, a noticeable decline in catalytic activity was observed as the reaction progressed. This reduction in performance is likely attributable to catalyst deactivation, which may result from factors such as active site poisoning, structural changes, or accumulation of humin-like byproducts on the catalyst surface. These findings indicate that while initial activity is consistent among the phosphate-modified niobates, long-term stability remains a key factor influencing overall catalytic efficiency. Additionally, the furfural yield did not show a decreasing trend during the reaction process, indicating that toluene, as the organic phase, effectively extracted

furfural from the aqueous phase and prevented furfural from undergoing other side reactions and degradation.

Table 3.3. TOF (1-hour reaction) and TON (5-hour reaction) for all catalysts after P-treatment

	P-$CaNb_2O_6$	P-$SrNb_2O_6$	P-$BaNb_2O_6$
TOF	6	9	10
TON	22	30	29

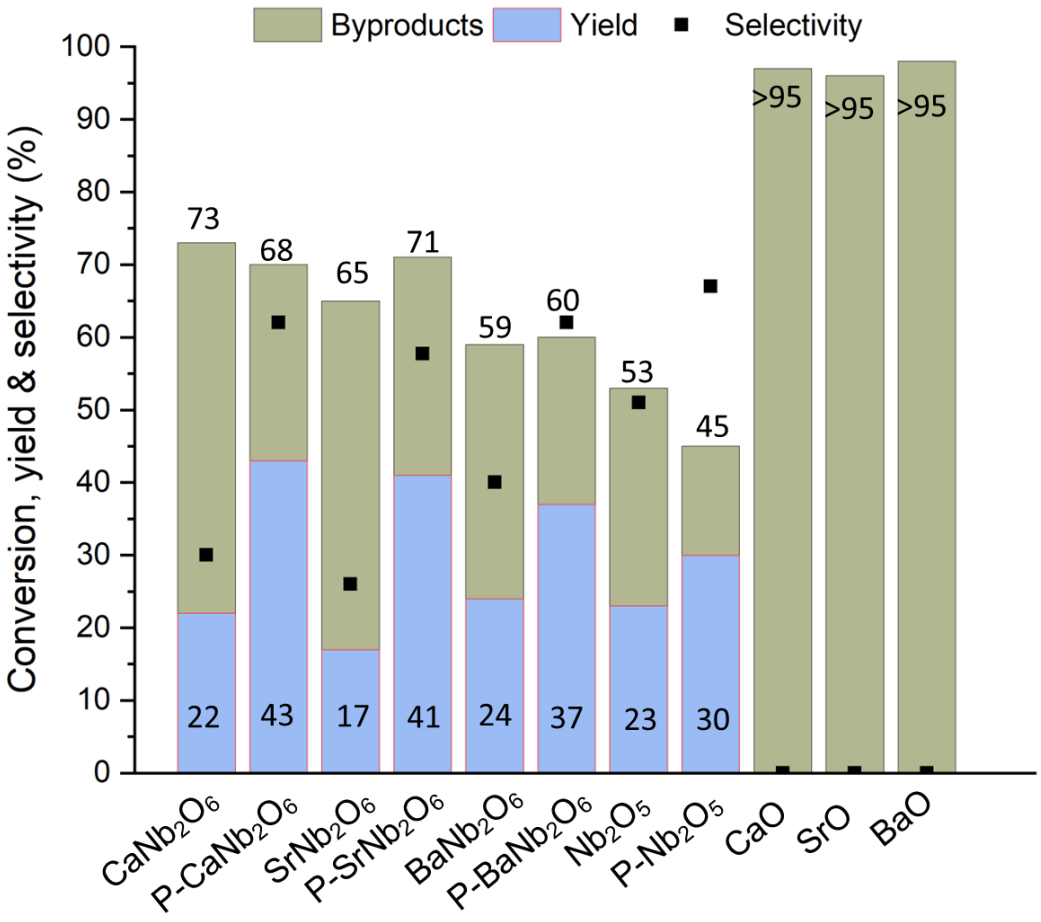

Figure 3.10. Catalytic performance in the dehydration of xylose to furfural. Reaction conditions: 300 mg of catalyst, 75 mg of xylose, 2 mL of aqueous phase, 8 mL of toluene at 120 °C for 5 hours.

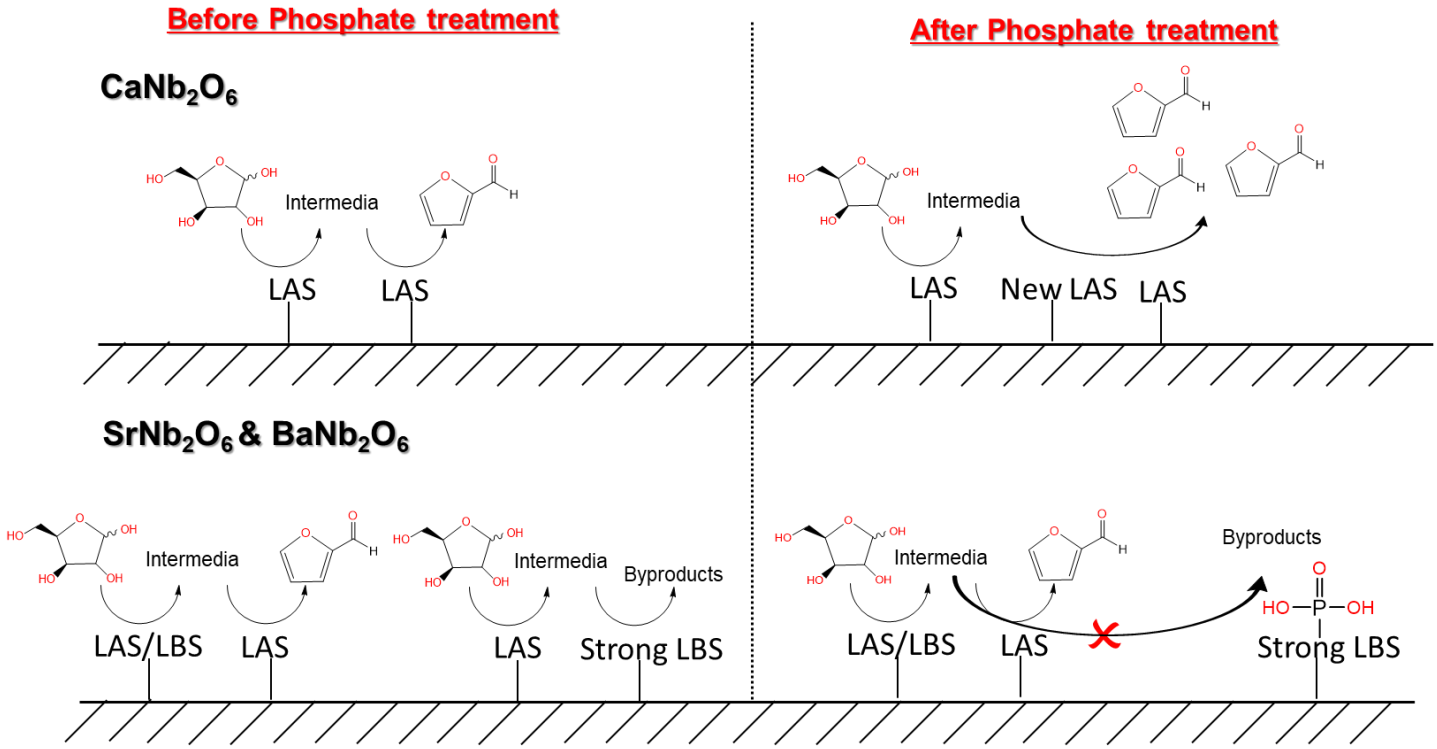

Figure 3.11. Mechanisms of xylose-to-furfural in catalysts based on active sites before and after P-treatment.

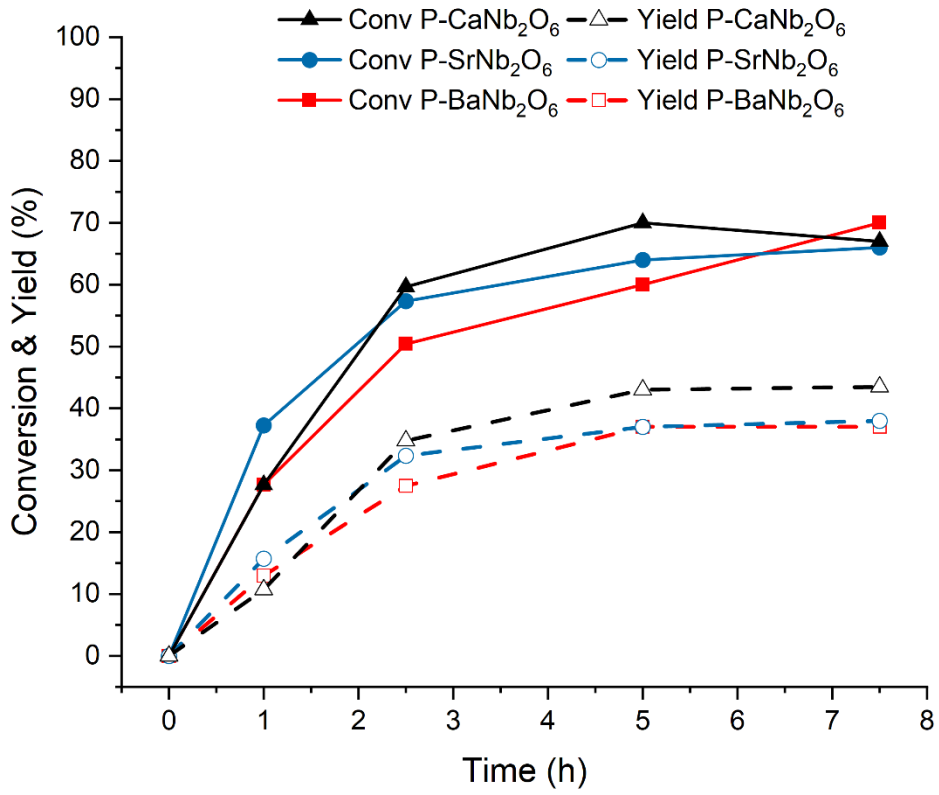

Figure 3.12. Time course curves of P-$CaNb_2O_6$, P-$SrNb_2O_6$, and P-$BaNb_2O_6$.

3.3.5 Stability of catalysts

To investigate whether phosphate molecules remain stably anchored on the surfaces of $CaNb_2O_6$, $SrNb_2O_6$, and $BaNb_2O_6$, a phosphate leaching test was conducted. The reaction was carried out under identical conditions (75 mg xylose and 300 mg catalyst in 2 mL aqueous phase and 8 mL toluene organic phase at 120 °C). After one hour of reaction, the catalyst was filtered out, and the reaction solution was retained to continue reacting for an additional four hours. As shown in **Figure 3.13**, no increase in furfural yield was observed in the absence of the catalyst. Under these conditions, the reaction itself proceeds very slowly under the conditions of 120 °C, and xylose conversion to furfural is minimal. This indicates that the phosphate molecules remain stably immobilized on the catalyst surfaces and do not leach into the solution. Additionally, P-$CaNb_2O_6$, P-$SrNb_2O_6$, and P-$BaNb_2O_6$ were subjected to five consecutive reaction cycles under the same conditions (**Figure 3.14**). After each reaction, the catalysts were filtered, dried, and calcined in an oven at 500°C before the next reaction cycle. The results showed that the conversion rate of xylose and the selectivity for furfural of P-$CaNb_2O_6$, P-$SrNb_2O_6$, and P-$BaNb_2O_6$ remained stable, thereby proving that all catalysts possess good thermal stability and reusability.

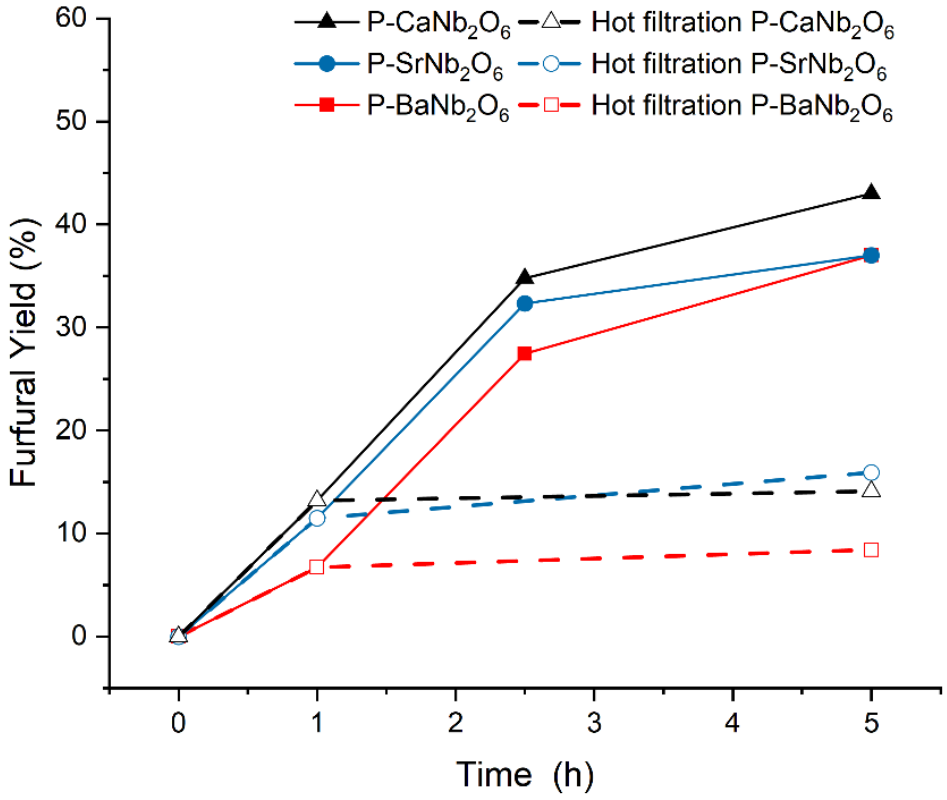

Figure 3.13. Phosphate leaching test. Reaction conditions: 300 mg of catalyst, 75 mg of xylose, 2 mL of aqueous phase, 8 mL of toluene at 120 °C. After one hour of reaction, the catalyst was removed, and the reaction continued for an additional four hours.

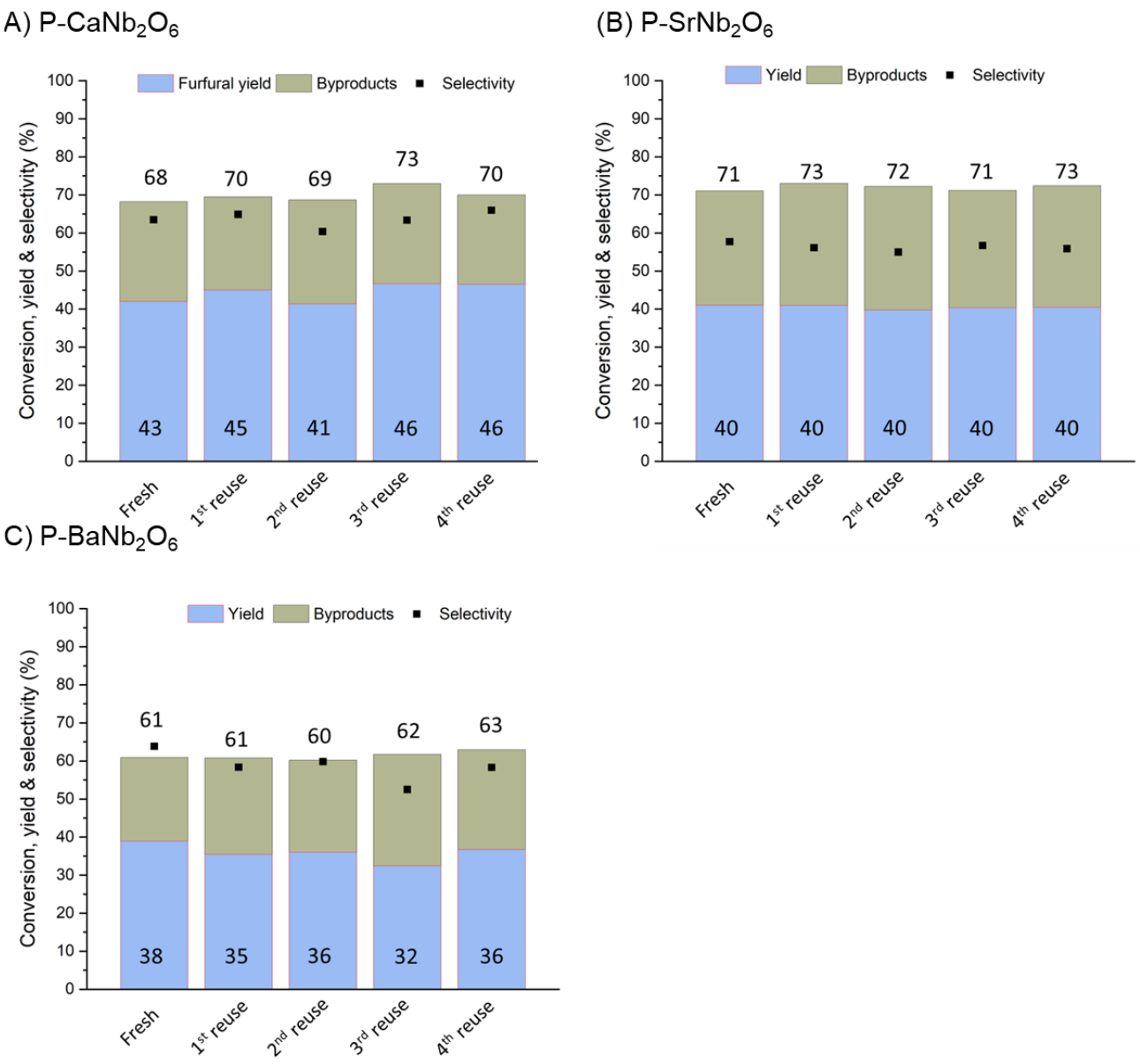

Figure 3.14. Reusability test of complex metal oxides after P-treatment: (A) P-$CaNb_2O_6$, (B) P-$SrNb_2O_6$, (C) P-$BaNb_2O_6$.

3.4 Conclusions

This study demonstrates that the influence of alkaline earth metals (Ca, Sr, Ba) as the secondary component and phosphate surface modification significantly influence the acidity, basicity, and catalytic behavior of complex niobates for xylose dehydration. The structure–property–performance relationships of phosphate-modified mixed metal oxide catalysts based on $CaNb_2O_6$, $SrNb_2O_6$, and $BaNb_2O_6$ were systematically investigated for the dehydration of xylose to furfural. The parent materials exhibited a clear trend in acid and base properties, with Lewis acidity decreasing in the order of $CaNb_2O_6$ > $SrNb_2O_6$ > $BaNb_2O_6$, while basicity followed the opposite trend ($CaNb_2O_6$ < $SrNb_2O_6$ < $BaNb_2O_6$). Phosphate modification exerted distinct effects depending on the metal species. In P-$CaNb_2O_6$, phosphate treatment cleaved Nb–O–Ca linkages and exposed unsaturated Nb species, significantly increasing the number of active Lewis acid sites and enhancing furfural selectivity. In contrast, for P-$SrNb_2O_6$ and P-$BaNb_2O_6$, phosphate groups were found to occupy both Lewis acid and base sites. Although this reduced the overall acid and base site densities, the suppression of strong Lewis base sites minimized side reactions and improved product selectivity. Catalytic evaluation revealed that all three phosphate-modified catalysts exhibited enhanced furfural selectivity. TOF and TON results showed a clear trend: P-$BaNb_2O_6$ ≈ P-$SrNb_2O_6$ > P-$CaNb_2O_6$, suggesting faster deactivation in P-$CaNb_2O_6$, likely due to differences in the nature of the Lewis acid sites. Despite its favorable acid-base properties, P-$BaNb_2O_6$'s catalytic performance was partially limited by its relatively low surface area. Finally, all phosphate-modified catalysts demonstrated excellent stability and reusability, maintaining consistent xylose conversion and furfural selectivity over five consecutive reaction cycles. The anchoring

of phosphate groups remained stable throughout, underscoring the robustness of the surface modification strategy.

3.5 References

[1] C. M. Cai, T. Zhang, R. Kumar, C. E. Wyman, *J of Chemical Tech & Biotech* **2014**, *89*, 2–10.

[2] A. Corma, S. Iborra, A. Velty, *Chem. Rev.* **2007**, *107*, 2411–2502.

[3] C. M. Cai, T. Zhang, R. Kumar, C. E. Wyman, *J of Chemical Tech & Biotech* **2014**, *89*, 2–10.

[4] P. Gan, K. Zhang, G. Yang, J. Li, Y. Zhao, J. Chen, *IJMS* **2024**, *25*, 11992.

[5] A. Pundir, M. Singh Thakur, S. Prakash, N. Kumari, N. Sharma, Z. He, S. Nam, S. Dhumal, K. Sharma, S. Saxena, S. Kumar, S. V. Deshmukh, M. Kumar, *Heliyon* **2024**, *10*, e35077.

[6] K. J. Yong, T. Y. Wu, C. B. T. L. Lee, Z. J. Lee, Q. Liu, J. M. Jahim, Q. Zhou, L. Zhang, *Biomass and Bioenergy* **2022**, *161*, 106458.

[7] Y. Konno, M. Hagiwara, S. Fujihara, *J. Ceram. Soc. Japan* **2014**, *122*, 12–16.

[8] Y. Zhang, C. Liu, G. Pang, S. Jiao, S. Zhu, D. Wang, D. Liang, S. Feng, *Eur J Inorg Chem* **2010**, *2010*, 1275–1282.

[9] I.-S. Cho, D. W. Kim, C. M. Cho, J.-S. An, H.-S. Roh, K. S. Hong, *Solid State Sciences* **2010**, *12*, 982–988.

[10] Z. Wang, R. Osuga, K. Endo, D. Padovan, S. Suganuma, A. Fukuoka, H. Kato, K. Nakajima, *Catal. Sci. Technol.* **2025**, 10.1039.D5CY00010F.

[11] N. K. Gupta, A. Fukuoka, K. Nakajima, *ACS Catal.* **2017**, *7*, 2430–2436.

[12] D. Padovan, K. Endo, T. Matsumoto, T. Yokoi, A. Fukuoka, H. Kato, K. Nakajima, *Small Structures* **2023**, *4*, 2200224.

[13] M. Kim, S. Ronchetti, B. Onida, N. Ichikuni, A. Fukuoka, H. Kato, K. Nakajima, *ChemCatChem* **2020**, *12*, 350–359.

[14] I.-S. Cho, S. T. Bae, D. H. Kim, K. S. Hong, *International Journal of Hydrogen Energy* **2010**, *35*, 12954–12960.

[15] M. P. Sena, S. P. D. Lima, L. S. Carvalho, D. Ruiz, A. Ballarini, A. R. Martins, *Matéria (Rio J.)* **2020**, *25*, e-12829.

[16] Z. Lin, Y. Lai, M. Li, J. He, M. Li, J. Zhou, S. Li, W. Qi, J. Han, Y. Zeng, **2024**, DOI 10.2139/ssrn.4936620.

[17] E. A. Moskvitina, V. A. Vorobiev, *J. Opt. Technol.* **2020**, *87*, 189.

[18] G. Li, E. A. Pidko, E. J. M. Hensen, K. Nakajima, *ChemCatChem* **2018**, *10*, 4084–4089.

[19] D. Dey, V. Petrykin, S. Sasaki, M. Kakihana, *J. Ceram. Soc. Japan* **2007**, *115*, 808–812.

[20] M. Kakihana, M. Kobayashi, K. Tomita, V. Petrykin, *Bulletin of the Chemical Society of Japan* **2010**, *83*, 1285–1308.

[21] X. Li, Z. Hu, S. Chen, J. Zhang, D. Pan, Z. Du, B. Wang, Y. Kong, *Journal of Alloys and Compounds* **2024**, *997*, 174886.

[22] K. Momma, F. Izumi, *J Appl Crystallogr* **2011**, *44*, 1272–1276.

[23] L. Pauling, *J. Am. Chem. Soc.* **1929**, *51*, 1010–1026.

[24] L. Pauling, *The Nature of the Chemical Bond and the Structure of Molecules and Crystals: An Introduction to Modern Structural Chemistry*, Cornell University Press, Ithaca New York, **1989**.

[25] L. H. Ahrens, *Geochimica et Cosmochimica Acta* **1952**, *2*, 155–169.

[26] Linus. Pauling, *J. Am. Chem. Soc.* **1931**, *53*, 1367–1400.

[27] R. Resta, D. Vanderbilt, in *Physics of Ferroelectrics*, Springer Berlin Heidelberg, Berlin, Heidelberg, **2007**, pp. 31–68.

[28] K. Fajans, *Naturwissenschaften* **1923**, *11*, 165–172.

[29] K. Fajans, G. Joos, *Z. Physik* **1924**, *23*, 1–46.

[30] K. Fajans, *Zeitschrift für Kristallographie - Crystalline Materials* **1924**, *61*, 18–48.

[31] S. Huber, *Journal of Molecular Catalysis A: Chemical* **1999**, *141*, 117–127.

[32] M. Tamura, K. Shimizu, A. Satsuma, *Applied Catalysis A: General* **2012**, *433–434*, 135–145.

[33] W. Song, H. Liu, J. Zhang, Y. Sun, L. Peng, *ACS Catal.* **2022**, *12*, 12833–12844.

[34] M. I. Zaki, M. A. Hasan, F. A. Al-Sagheer, L. Pasupulety, *Colloids and Surfaces A: Physicochemical and Engineering Aspects* **2001**, *190*, 261–274.

[35] In *Surface Enhanced Raman Vibrational Studies at Solid/Gas Interfaces*, Springer-Verlag, Berlin/Heidelberg, **1984**, pp. 26–58.

[36] I. Delidovich, *ACS Catal.* **2023**, *13*, 2250–2267.

[37] A. N. Simonov, L. G. Matvienko, O. P. Pestunova, V. N. Parmon, N. A. Komandrova, V. A. Denisenko, V. E. Vas'kovskii, *Kinet Catal* **2007**, *48*, 550–555.

[38] I. V. Delidovich, A. N. Simonov, O. P. Taran, V. N. Parmon, *ChemSusChem* **2014**, *7*, 1833–1846.

[39] I. V. Delidovich, A. N. Simonov, O. P. Pestunova, V. N. Parmon, *Kinet Catal* **2009**, *50*, 297–303.

Chapter 4

Summary and outlook

Lignocellulosic biomass, characterized by its abundant availability and vast reserves, has attracted significant attention for its research and commercial potential, particularly in the current fossil energy crisis. Composed primarily of cellulose, hemicellulose, and lignin, lignocellulosic biomass was initially regarded merely as a substitute for fossil fuels. However, recent research has increasingly focused on its decomposition into small molecules, which can serve as intermediates for producing a broad range of value-added chemicals. Among the twelve top-value platform chemicals identified by the U.S. Department of Energy, furfural stands out due to its wide applicability and considerable research value. In particular, developing efficient, green, and sustainable synthetic routes to furfural has become a key research objective.

Among the various conversion strategies, acid-catalyzed dehydration of xylose remains the most industrially viable route. While traditional homogeneous acid catalysts offer high activity, they suffer from drawbacks such as poor recyclability, corrosiveness, and environmental impact. As a result, heterogeneous catalysts featuring high stability and conversion efficiency have emerged as the next-generation candidates for industrial-scale furfural production. Among them, amorphous niobium oxide (Nb_2O_5) has received considerable attention for its unique catalytic properties and high furfural yields. Nevertheless, its structural instability limits practical applications. Although high-temperature calcination enhances its structural stability by inducing crystallinity, the accompanying loss of acidity and catalytic activity restricts its performance. To address the trade-off between stability and catalytic efficiency, complex metal oxides have been

developed as a promising solution, offering enhanced durability while maintaining or improving catalytic performance. In particular, niobium-based oxides (e.g., Nb_2O_5 and its crystalline derivatives) have emerged as promising catalysts owing to their unique acidity and structural adaptability. This research should focus on acid-catalyzed controlling, optimizing active site distributions, and integrating catalysts with advanced process intensification technologies (e.g., biphasic systems). These efforts will contribute to the development of efficient and sustainable catalytic systems for biomass valorization and furfural-based chemical production.

In Chapter 2, a phosphate-modified $CaNb_2O_6$ (P-$CaNb_2O_6$) catalyst was developed using the amorphous metal complex (AMC) method and investigated for its performance in the dehydration of xylose to furfural. The catalyst structure, consisting of NbO_6 octahedra and CaO_8 polyhedra, offers a favorable framework for the generation of Lewis acid sites (LAS) and minor Brønsted acid sites (BAS). Phosphate surface modification not only suppressed undesirable side reactions by deactivating overly strong LAS but also enhanced the population of catalytically active LAS, leading to improved furfural yield and selectivity. Compared to both untreated $CaNb_2O_6$ and phosphate-treated Nb_2O_5, P-$CaNb_2O_6$ displayed superior catalytic efficiency and structural resilience. Furthermore, P-$CaNb_2O_6$ retained its performance over five regeneration cycles, confirming its excellent thermal stability and reusability, which makes it a promising candidate for sustainable biomass valorization.

Chapter 3 presents a systematic investigation of phosphate-modified niobate catalysts incorporating different alkaline earth metals (Ca, Sr, Ba), revealing how variations in ionic radius and polarization ability affect acidity, basicity, and catalytic behavior. The parent oxides displayed a clear trend in acid–base properties: Lewis acidity

decreased from $CaNb_2O_6$ to $BaNb_2O_6$, while basicity increased correspondingly. Upon phosphate treatment, distinct modifications occurred depending on the metal species. In P-$CaNb_2O_6$, the cleavage of Nb–O–Ca linkages exposed additional Lewis acid sites, significantly enhancing catalytic activity. Conversely, in P-$SrNb_2O_6$ and P-$BaNb_2O_6$, phosphate group occupied both acid and base sites, suppressing strong basicity and thereby improving furfural selectivity by minimizing side reactions. Despite differences in surface properties, all catalysts demonstrated stable performance and reusability over five cycles, with phosphate anchoring remaining intact throughout.

The efficient and selective production of furfural from xylose represents a crucial step in upgrading lignocellulosic biomass into value-added chemicals. Addressing the limitations of conventional homogeneous acid systems, this research focuses on the development of structurally robust and acid-tunable niobium-based solid catalysts. Specifically, this study explores how crystalline complex metal oxides can be systematically engineered to balance catalytic activity, selectivity, and reusability through compositional design and surface functionalization. **Chapters 2 and 3** together present a dual strategy: the use of alkaline earth metal substitution to regulate the structural and chemical environment of niobates, and phosphate surface treatment to fine-tune their acid properties. These chapters reflect a coherent framework for understanding how both bulk lattice composition and surface modification collectively determine catalytic behavior. This approach not only enables the modulation of acidity but also provides insight into the suppression of side reactions and the stabilization of active sites under aqueous conditions. The comparative and systematic nature of the investigation lays a foundation for broader catalyst design strategies applicable to a range of biomass-derived reactions.

Beyond the current findings, future work should focus on rational engineering of crystallographic features to explore synergistic configurations of LAS and BAS. Incorporating multi-element doping strategies or defect engineering may further amplify site cooperation and reaction specificity. Additionally, mechanistic studies using FTIR spectroscopy are warranted to elucidate the dynamic evolution of active sites under real reaction conditions. Integrating these catalysts into continuous-flow biphasic reactor systems could also bridge the gap between laboratory performance and industrial feasibility. Ultimately, combining structural design with process intensification will be crucial in advancing robust, selective, and recyclable solid acid catalysts for scalable biomass conversion.

List of Publications

Journal publications

Zijian Wang, Ryota Osuga, Koichiro Endo, Daniele Padovan, Satoshi Suganuma, Atsushi Fukuoka, Hideki Kato and Kiyotaka Nakajima*; Lewis acid catalysis of phosphate-modified CaNb2O6 for xylose dehydration to furfural. ***Catal. Sci. Technol.*** **2025**. DOI. 10.1039.D5CY00010F.

Conference contributions

Zjian Wang, Daniele Padovan, Ryota Osuga, Satoshi Suganuma, Atsushi Fukuoka, Hideki Kato, Kiyotaka Nakajima. Acid-base catalysis of Nb-based mixed oxides with phosphate group for the dehydration of biomass-derived sugars to furanics. ICAT International Symposium on Catalysis 2023. Institute for Catalysis, Hokkaido University, Sapporo, Japan, July 18–19, 2023. (Poster)

Zijian Wang, Daniele Padovan, Ryota Osuga, Satoshi Suganuma, Atsushi Fukuoka, Hideki Kato, Kiyotaka Nakajima. Acid catalysis of Nb-based mixed oxides for the dehydration of biomass-derived sugars to furanics. 132nd CATSJ meeting, Sapporo, Japan. September 13-15, 2023. (Oral)

Acknowledgement

First and foremost, I would like to express my deepest gratitude to my supervisors, Professor Jun-ya Hasegawa and Professor Atsushi Fukuoka, for their unwavering support, insightful guidance, and constructive feedback throughout my doctoral journey. Their expertise and academic rigor have been instrumental in shaping not only the direction of this research but also my overall growth as a researcher. I am especially thankful for their patience, encouragement, and generosity in sharing their knowledge, which gave me the freedom to explore independently and the mentorship necessary to stay on course.

I would also like to extend my heartfelt thanks to Professor Kiyokata Nakajima, who has served as my de facto supervisor and whose high expectations, academic rigor, and uncompromising standards have had a profound impact on my research. Throughout the course of my doctoral study, he continuously challenged me to refine my thinking, clarify my logic, and pursue scientific excellence. Although the research and writing process faced numerous setbacks and revisions, it was under his strict and thoughtful guidance that I was able to transform preliminary ideas into a more coherent, rigorous, and well-structured academic argument. His insistence on clarity, precision, and scientific integrity ultimately enabled this work to be successfully completed and published. I am deeply grateful for his commitment to mentoring and for pushing me beyond what I believed I was capable of achieving.

I would also like to express my special thanks to Dr. Ryota Osuga, whose deep expertise in FTIR spectroscopy has had a lasting influence on my research and scientific development. Among all the techniques I encountered during my doctoral work, infrared spectroscopy stood out as the most intellectually engaging and rewarding, largely thanks

to his mentorship. Under Dr. Osuga's patient and meticulous guidance, I came to appreciate the subtle yet powerful insights that can be derived from adsorption peaks—how vibrational shifts and spectral details can reveal rich information about catalytic behavior and surface phenomena. His teaching opened my eyes to the depth and nuance of FTIR analysis, and I gradually developed a genuine fascination for the method that has since become a core part of my research identity. Beyond technical training, Dr. Osuga also generously supported me through multiple stages of manuscript preparation and presentation. He was always patient, providing detailed feedback and helping me refine both scientific content and logical structure. We had numerous thoughtful discussions throughout my doctoral work, and while we occasionally held differing views, it was precisely those differences that made our conversations more meaningful. His openness to debate and emphasis on evidence-based reasoning embodied the spirit of true scientific inquiry and I am deeply grateful for the intellectual growth I gained from working with him.

I would like to extend my sincere appreciation to Dr. Daniele Padovan and Dr. Jan J. Wiesfeld for their generous support and guidance during the early stages of my doctoral research. When I first joined the laboratory, it was Daniele and Jan who helped me become familiar with the lab's protocols, safety procedures, and day-to-day operations. Their kindness and patience played a crucial role in helping me transition smoothly into a new research environment. In particular, I am deeply grateful to Daniele for mentoring me through my initial research projects. He took the time to walk me through each experimental step and introduced me to a wide range of analytical instruments and techniques. Thanks to his clear explanations and hands-on training, I was able to build a solid foundation in laboratory practice and data interpretation. His approachable and

encouraging attitude made it easy to ask questions and learn from mistakes, which gave me the confidence to progress independently. I am equally thankful to Jan, whose technical expertise and in-depth knowledge of laboratory equipment were indispensable throughout my time in the lab. Whenever technical issues arose—whether with the GC, IR cell, or vacuum system—Jan always managed to quickly diagnose the problem and find practical solutions, ensuring that experimental workflows were not delayed. His resourcefulness and willingness to help others contributed greatly to the efficient functioning of the lab and made him a constant source of support. I truly appreciate the time and effort both of them invested in helping me grow as a researcher.

I would also like to extend my special thanks to Dr. Zhihao Yu. Although his time in our laboratory was relatively short, he made a lasting impression through our frequent scientific discussions and mutual exchange of academic ideas. We often shared research papers, debated mechanisms, and reflected on experimental results, and I found these conversations to be intellectually stimulating and personally motivating. His curiosity, analytical thinking, and open-mindedness consistently encouraged me to challenge my own assumptions and to explore problems from new perspectives. Through our exchanges, I came to believe even more strongly that scientific research should never be a solitary endeavor. While focused, independent work is essential, the inspiration and clarity that arise from dialogue and collaboration are equally invaluable. As researchers, we must occasionally look up from our workbench—both literally and metaphorically—and seek broader insights. For that perspective and companionship in thought, I am truly grateful.

I would also like to thank the former members of our laboratory—Dr. Shaikh Nazmul Hasan Mohammad Dostagir, Dr. Yayati Naresh Palai, and Dr. Abhijit Shrotri—for their kind support and valuable advice during my early days in the lab. Their guidance

and encouragement helped me quickly adapt to the research environment. I am equally grateful to all current lab members for creating a friendly and collaborative atmosphere, which made my research journey both productive and enjoyable.

I would also like to express my sincere gratitude to Hokkaido University and the Institute for Catalysis (ICAT) for providing generous financial support and access to world-class research facilities, which were essential for the successful completion of my doctoral work. I am especially grateful to my committee members—Prof. Hasegawa, Prof. Fukuoka, Prof. Shimizu, Prof. Nakano, and Prof. Murayama—for their valuable feedback, constructive discussions, and continuous encouragement throughout the course of my research. Their expertise and insights have been instrumental in shaping the direction and quality of this dissertation.Lastly, I would like to express my heartfelt thanks to my family, my friends, and my former teachers, whose unwavering support has accompanied me throughout every stage of this journey. Their encouragement—both past and present—has given me the strength to keep moving forward, especially in moments of doubt and difficulty. I truly could not have come this far without them, and for that, I am deeply and sincerely grateful.

Appendix

Investigation of Phosphate-Modified Nb_2O_5 Catalysts: Insights into Surface Modification in Furfural Production

Abstract

Phosphate-modified niobium oxides (NbOP) were synthesized via a pre-mixing method and systematically compared to phosphate post-treated niobium oxides (P-Nb_2O_5) in terms of structure, surface acidity, and catalytic performance for furfural production from xylose. The previous research has shown that pre-mixing phosphate during synthesis effectively stabilized the metastable TT-phase structure and increased the density of Lewis and Brønsted acid sites. However, catalytic testing revealed that NbOP-1 (Nb:P = 20:1) and post-treated 500P-Nb_2O_5 (TT-phase) exhibited comparable furfural yields, selectivity, and stability, despite differences in activation energies and structural features. These results suggest that phosphate pre-mixing modifies surface properties but does not fundamentally enhance catalytic performance relative to conventional post-treatment methods. This study provides insights into the limitations of structural and acidic property modifications for improving the catalytic efficiency of crystalline niobium oxides.

Introduction

Biomass, as a renewable carbon source, exhibits great potential for replacing fossil fuels.[1] Xylose and glucose, the main monosaccharides produced from biomass hydrolysis, can be converted into furfural and 5-hydroxymethylfurfural (HMF), respectively, through dehydration reactions.[2,3] These compounds are important bio-based platform chemicals that can be further transformed into fuels and high-value-added chemicals. To address issues associated with homogeneous mineral acid-catalyzed dehydration reactions—such as equipment corrosion, difficulties in product separation, and environmental pollution[4–6]—various solid metal oxide catalysts have been applied in the conversion of biomass-derived sugars. For example, phosphotungstic acid ($H_3PW_{12}O_{40}$) supported on silica exhibits excellent catalytic activity.[7,8] Sulfated zirconia (SO_4^{2-}/ZrO_2) shows high selectivity in the conversion of fructose to HMF.[9] Due to their unique structure and acidity, titanate nanotubes have been used for aldol condensation.[10] Additionally, solid acidic ion-exchange resins, heteropoly acids, and layered double hydroxides (LDHs) have also been extensively studied.[11–13]

Among various metal oxides, niobium pentoxide (Nb_2O_5) has attracted widespread attention in fields such as catalysis, optics, electronics, and energy storage due to its unique physicochemical properties.[14–18] In catalysis, Nb_2O_5 is renowned for its strong acidity, enabling excellent performance in acid-catalyzed reactions.[19,20] It has been widely applied in hydrocarbon conversion, esterification, and condensation reactions, particularly in converting biomass-derived sugars into valuable platform chemicals. Specifically, Nb_2O_5 can dehydrate xylose to produce furfural and convert glucose into HMF, serving as key intermediates in the production of bio-based fuels and chemicals.[21,22] However, the practical application of amorphous Nb_2O_5 catalysts is

limited by stability issues, mainly due to the facile deposition of carbonaceous by-products on the catalyst surface during reactions. Such carbon deposition can block active sites, significantly reduce catalytic performance, and shorten the catalyst's service life. To address these issues, amorphous Nb_2O_5 is typically transformed into crystalline form through calcination. Crystallized Nb_2O_5 possesses an ordered lattice structure, exhibiting higher thermal stability and resistance to carbon deposition, thereby improving its catalytic stability and performance.[19,23] Nevertheless, even after crystallization, there remains room for improvement in the activity and selectivity of Nb_2O_5.

To enhance the catalytic performance of Nb_2O_5, various modifications have been explored. For example, doping with transition metals can adjust the acid-base properties of Nb_2O_5,[24–26] while compositing Nb_2O_5 with other metal oxides such as TiO_2 can improve its surface properties and catalytic performance.[27] Previous studies have shown that amorphous Nb_2O_5 possesses good Lewis acid catalytic properties, and the role of Brønsted acid sites is not significant in the conversion of xylose to furfural.[21,22] However, upon crystallization, all Brønsted acid sites in Nb_2O_5 disappear, leaving only a small number of Lewis acid sites, resulting in a significant decrease in catalytic performance.[23] This suggests that crystalline Nb_2O_5 may no longer possess the unique properties of amorphous Nb_2O_5. Conversely, studies have found that when Brønsted acid and Lewis acid catalysts are combined, the selectivity for furfural is higher than when using Lewis acid catalysts alone.[28–30] Therefore, modifying crystalline niobium oxide to endow it with Brønsted acid capabilities can enhance its catalytic performance and improve the selectivity of xylose conversion to furfural.

Previous research has shown that phosphate treatment of catalysts can significantly improve their performance; however, it is difficult to introduce a large number of

Brønsted acid sites through post-treatment methods. In contrast, directly adding phosphoric acid during the synthesis of Nb_2O_5—that is, introducing phosphoric acid at the synthesis stage—can effectively embed phosphate groups into the Nb_2O_5 lattice, forming a uniformly distributed phosphate-doped structure.[31] This pre-mixing is expected to enhance the binding force between phosphate and Nb_2O_5, improving the material's structural stability and surface acidity. Furthermore, pre-mixing may introduce oxygen vacancies and other lattice defects, further regulating the electronic structure and catalytic performance of Nb_2O_5.[26] By comparing the effects of phosphate post-treatment and pre-mixing on the structure, surface properties, and catalytic performance of crystalline Nb_2O_5, a more effective modification strategy can be developed. The effects of these two modification methods on the crystal phase, morphology, surface acidity, and catalytic activity of the material are systematically investigated, and their mechanisms are explored in depth.

Experimental section

Chemical reagent

$NbCl_5$ was purchased from HIGH PURITY CHEMICALS. Hydrogen peroxide (30%~35%), phosphoric acid (>85%), toluene (>99.5%), chloroform (>99.0%), Barium carbonate (>99.0%) were supplied by KANTO CHEMICAL CO., INC. Ammonia solution (28%), L-lactic acid, Calcium nitrate tetrahydrate (99.9%), strontium nitrate (98.0~102.0% mass/mass), D(+)-xylose, pyridine(dehydrated) were obtained FUJIFILM Wako Pure Chemical Corporation. furfural(>98%), chlorobenzene(>98%) were received Tokyo Chemical Industry (TCI).

Catalysts preparation

Pre-mixing niobium pentoxide (NbOP) catalysts were synthesized using the Amorphous Metal Complex (AMC) method.[32,33] First, 25 g of anhydrous $NbCl_5$ was slowly added to 300 mL of distilled water under stirring. The pH of the solution was adjusted to 7 using aqueous ammonia, and the mixture was stirred at 600 rpm for 3 hours. After ensuring the pH remained stable at 7, the precipitate was thoroughly washed with distilled water over 20 cycles to remove Cl^- ions, yielding a white $NbO_x \cdot mH_2O$ precipitate. A portion of this precipitate was calcined at 1000 °C for 10 hours to determine the niobium content.

Next, $Nb(CH_3CH(OH)COO)(CH_3CH(O)COO)_2$, referred to as Nb-La, was prepared by adding 80 mmol of lactic acid and 200 mmol of hydrogen peroxide to 20 mmol of $NbO_x \cdot mH_2O$. The pH was adjusted to 4.5 with aqueous ammonia, and the mixture was stirred at 240 rpm and 60 °C for 1 hour. It was then heated to 90 °C and maintained overnight to obtain a yellow solid, which was dispersed in 50 mL of distilled water to produce Nb-La.

For the synthesis of phosphate pre-mixed niobium oxides (NbOP) catalysts, 5 mmol of Nb-La and varying amounts of phosphoric acid were combined. For Nb:P ratios of 20:1 and 40:1 named NbOP-1 and NbOP-2, 5 mmol of Nb-La was mixed with 0.25 mmol and 0.125 mmol of phosphoric acid, respectively. The mixtures were dried by heating below 100 °C to form powders, then stabilized at 250 °C for 1 hour, heated to 450 °C for 3 hours, and finally calcined at 700 °C for 5 hours in a muffle furnace to obtain NbOP catalysts

TT-phase and T-phase Nb_2O_5 was synthesized following the same procedure without the addition of phosphoric acid: 5 mmol of Nb-La was heated below 100 °C to form a

powder, stabilized at 250 °C for 1 hour, heated to 450 °C for 3 hours, and calcined at 500 and 700 °C for 5 hours, labeled as 500-Nb_2O_5 and 700-Nb_2O_5.

Phosphate post-treatment of Nb_2O_5 involved adding 1 g of the catalyst to 200 mL of a 1 M phosphoric acid solution and stirring at 500 rpm at room temperature for two days. The catalyst was then washed and filtered four times, dried overnight in an oven, and labeled as 500P-Nb_2O_5 and 700P-Nb_2O_5.

Characterization

An Ultima IV Rigaku diffractometer was employed for X-ray diffraction (XRD) measurements, operating at 40 kV and 40 mA with Cu Kα radiation ($\lambda = 1.5418$ Å), scanning over a 2θ range from 10° to 80°. Nitrogen adsorption isotherms were measured at 77 K using a Micromeritics 3-Flex analyzer, after degassing the samples at 150 °C for one hour. The Brunauer–Emmett–Teller (BET) method was used to calculate the surface areas within a relative pressure range of $P/P_0 = 0.05–0.30$. X-ray photoelectron spectroscopy (XPS) was conducted on a JEOL JPS-9010MC spectrometer, and the data were processed using CasaXPS software. Fourier Transform Infrared (FTIR) spectra were acquired using a JASCO FT/IR-4100 spectrometer equipped with a cooled mercury cadmium telluride (MCT) detector. Disks of the catalyst (20 mm diameter, 40–90 mg) were placed in an IR cell connected to a closed-loop circulation system and evacuated under vacuum at 300 °C for one hour before measurement. Pyridine and chloroform were used as probe molecules to evaluate the acidity and basicity of the catalysts, respectively. Temperature-programmed desorption (TPD) analyses were carried out on a MicrotracBEL Belcat II instrument equipped with a thermal conductivity detector (TCD) and a mass spectrometer. Approximately 100 mg of catalyst was loaded into a quartz cell

and degassed at 300 °C for two hours prior to analysis. Ammonia (5% in helium) was used as the probe molecule for acidic sites.

Furfural production from xylose dehydration

Catalytic reactions were carried out in a pressure-resistant spherical glass reactor. Each reaction system consisted of a biphasic mixture containing 75 mg of xylose dissolved in 2 mL of aqueous solution and 8 mL of toluene, combined with 100 mg of catalyst. The reactions were maintained at 120 °C for five hours in an oil bath. Upon completion, the reactor was rapidly cooled in an ice bath, and the reaction mixture was separated by centrifugation. The aqueous phase was analyzed using a Shimadzu LC-2030C Plus high-performance liquid chromatograph equipped with a BIO-RAD Aminex HPX-87H column. A mobile phase of 5 mmol L^{-1} sulfuric acid was used, and detection was performed with a refractive index detector (RID-20A) and an ultraviolet detector set at 245 nm. The organic phase was quantified by adding chlorobenzene as an internal standard and analyzed using a Shimadzu GC-2025AF gas chromatograph equipped with a flame ionization detector (FID). Conversion, yields and selectivity were calculated based on the following equations. In this study, the detectable product is limited only to furfural, meaning that by-products are defined as "humin-type undetectable species".

$$\boldsymbol{Conversion} = \mathbf{100\%} * \frac{\boldsymbol{Moles\ of\ xylose_{initial} - Moles\ of\ sylose_{final}}}{\boldsymbol{Moles\ of\ xylose_{initial}}} \quad \textbf{(1)}$$

$$\boldsymbol{Yield_{fufural}} = \mathbf{100\%} * \frac{\boldsymbol{Moles\ of\ furfural_{final}}}{\boldsymbol{Moles\ of\ xylose_{initial}}} \quad \textbf{(2)}$$

$$\boldsymbol{Yield_{by-products}} = \boldsymbol{Moles\ of\ xylose_{initial} - Yield_{fufural}} \quad \textbf{(3)}$$

$$Selectivity_{furfural} = 100\% * \frac{Yield_{fufural}}{Conversion} \quad (4)$$

Results and Discussion

Crystalline analysis of phosphate-modified niobium oxide based on XRD

Pre-mixing phosphate niobium oxide (NbOP) samples with varying Nb:P ratios were prepared using the AMC method by adjusting the amount of phosphoric acid and calcining at 700 °C. The surface phosphorus content of each sample was determined by XPS, as shown in **Table A1**. The surface phosphorus atomic percentage of NbOP-1 (Nb:P = 20:1) is relatively high, reaching 3.9%. This is comparable to that of 700P-Nb_2O_5. In contrast, NbOP-2 (Nb:P = 40:1) exhibits a lower surface atom percentage of phosphorus (2.1%). Based solely on the Nb to P ratio on the surface, the phosphorus content of NbOP-1 is approximately twice that of NbOP-2. The surface phosphorus atomic percentage of 500P-Nb_2O_5 is 2.8%. The XRD patterns of NbOP-1, NbOP-2, 700P-Nb_2O_5, 500P-Nb_2O_5, and the 100:1 sample are shown in **Figure A1**. Among them, 500P-Nb_2O_5, NbOP-1, and NbOP-2 exhibit the TT-phase, a pseudohexagonal structure. When the phosphate content during pre-mixing is sufficiently low, as in the Nb:P = 100:1 sample, the crystalline phase transitions from TT-phase to T-phase (orthorhombic).[34] The 700P-Nb_2O_5 sample displays a complete T-phase. The TT-phase, characterized by pseudohexagonal symmetry in localized regions, is often embedded within other crystal systems, such as orthorhombic superlattices. This structure typically features open channels and a disordered arrangement of NbO_6 or NbO_7 octahedra, leading to significant variations in bond angles and lengths. As a result, the structure is relatively loose, prone to forming surface defect sites, and rich in crystalline defects.[34]

Table A1. Determining the surface phosphorus content of various niobium oxide Catalysts by XPS.

Sample[a]	Weight(P/Nb%)	Surface P atomic percent (%)	Surface ratio Nb:P
NbOP-1	1.7	3.9	5.4
NbOP-2	<0.1	2.1	10.5
500P-Nb_2O_5	-	2.8	8.3
700P-Nb_2O_5	-	3.9	5.4

[a] NbOP-1 and NbOP-2 are Nb:P ratios of 20:1 and 40:1, respectively. 500P-Nb_2O_5 and 700P-Nb_2O_5 are post-treatment phosphate catalysts calcinated at 500 and 700 °C for 5 hours, respectively.

To further study whether pre-mixing phosphate niobium oxide can form a crystalline phase at lower temperatures, calcination was performed at 600 °C; however, the catalyst remained amorphous (**Figure A2**). Even when the calcination time was extended from five to ten hours, it remained amorphous. Only at 700 °C did it form a crystalline phase, consistent with results reported by others; for instance, the catalysts NbP synthesized by Vieira et al. were amorphous when calcined at 550 °C.[35] Further examination of the crystal structure of NbOP-1 calcined at higher temperatures revealed that NbOP-1 still exhibited the TT-phase at 800 °C. At 900 °C, while the T-phase of Nb_2O_5 was present, characteristic peaks of the H-phase began to form, accompanied by some PO_4 characteristic peaks (012 and 110).[36–39] At 1000 °C, it completely transformed into the H-phase (**Figure A3**).[36] Typically, for niobium oxide, the TT-phase (pseudo-hexagonal) forms at 400–500 °C, the T-phase (orthorhombic) at 700 °C, and the H-phase (monoclinic)

at 900 °C.[23] This suggests that pre-mixing phosphate inhibits the crystallization of Nb_2O_5, delaying the phase transitions. Although the phosphate was introduced during the precursor stage and calcined at 700 °C, the XRD patterns of the resulting catalyst retained the characteristic reflections of the low-temperature Nb_2O_5 phase (TT-pahse), in contrast to the thermodynamically stable T-phase typically formed at this temperature. These domains likely inhibited the rearrangement of NbO_6 octahedra and suppressed the crystallographic transition, thereby stabilizing the metastable phase. The preservation of surface acidity and catalytic performance further supports the conclusion that phosphate molecules function primarily as surface modifiers, exerting both chemical and structural control without entering the bulk lattice.

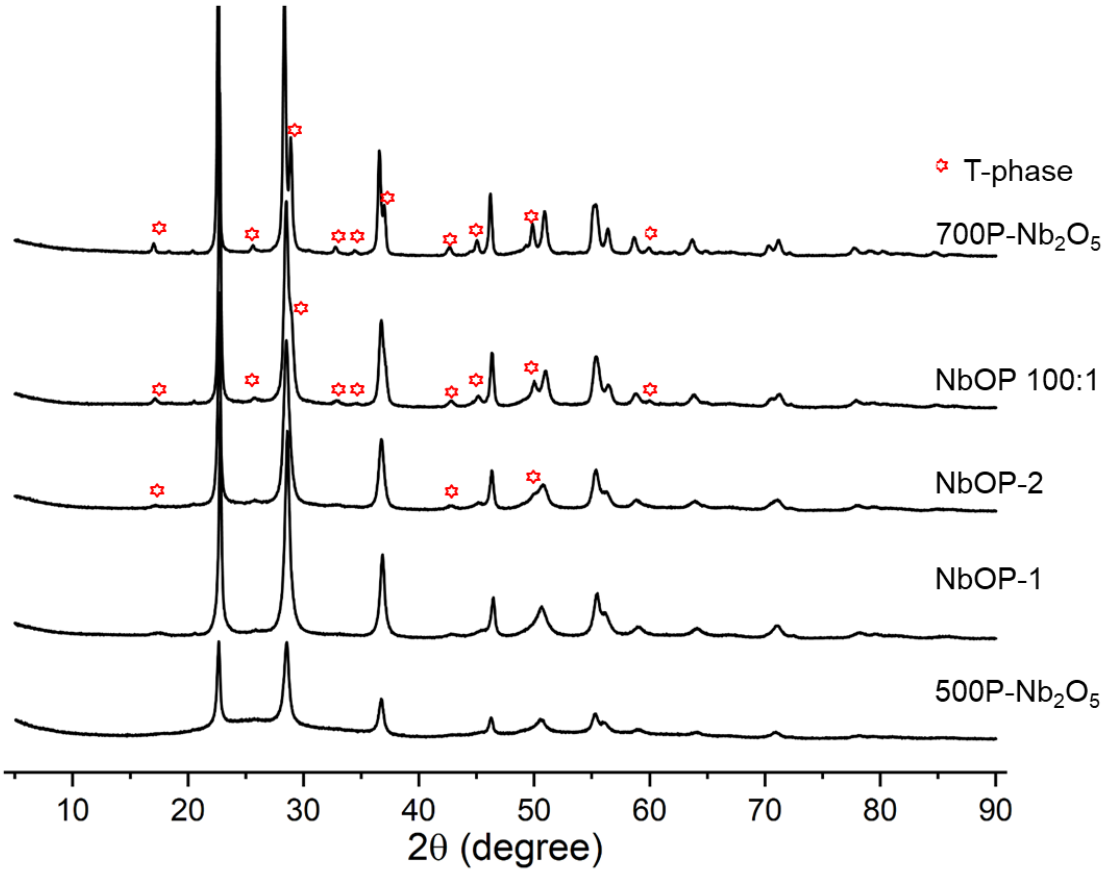

Figure A1. XRD pattern of the niobium catalysts in different Nb:P ratio.

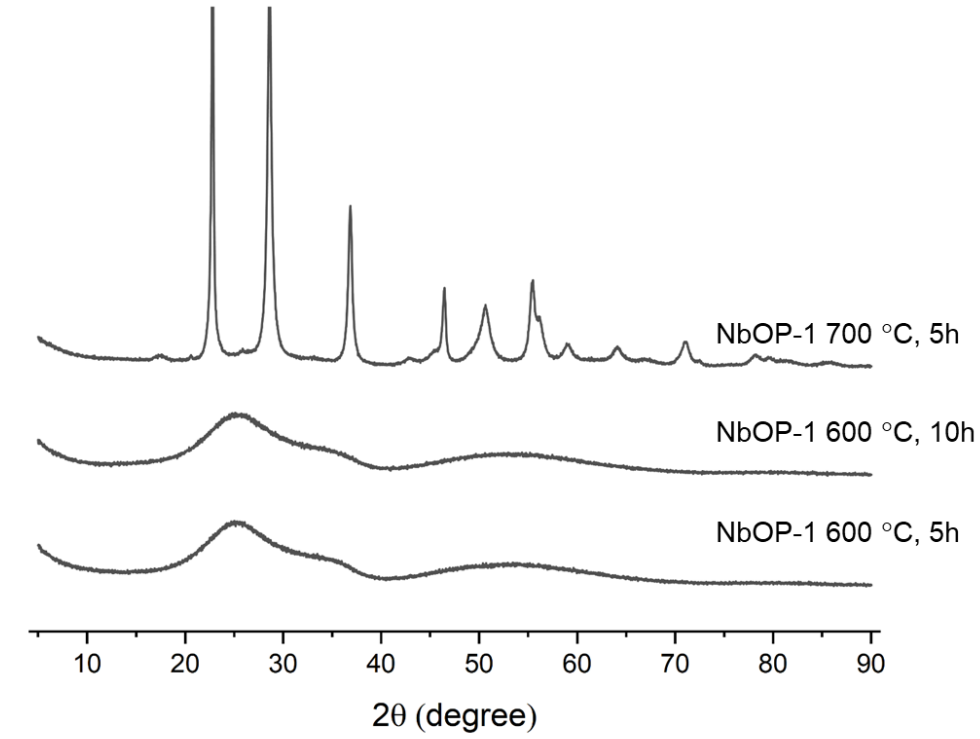

Figure A2. XRD pattern of NbOP 20:1 in 600 °C calcination temperature check.

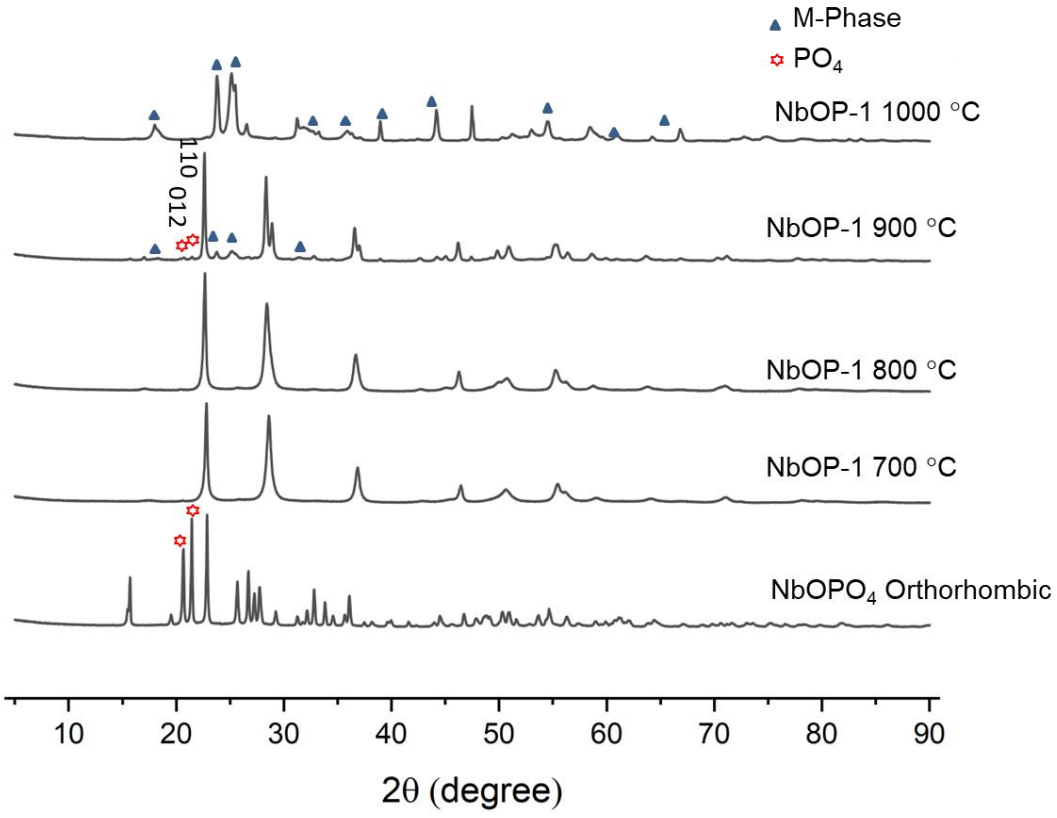

Figure A3. XRD pattern of NbOP 20:1 in different higher temperatures.

Acidic properties of mixed metal oxides catalysts

The types and amounts of surface acid sites on the catalysts were determined using pyridine infrared spectroscopy (pyridine-IR). The absorption bands at 1540 and 1635 cm^{-1} are attributed to pyridine protonated on Brønsted acid sites (BAS), while those at 1446 and 1606 cm^{-1} correspond to pyridine adsorbed on Lewis acid sites (LAS). The band at 1489 cm^{-1} is assigned to pyridine adsorbed on both LAS and BAS.[40,41] According to **Figure A4**, 700P-Nb_2O_5 exhibits almost no BAS, and the sharp peak at 1606 cm^{-1} indicates only a small amount of LAS. In contrast, phosphate-doped niobium oxides NbOP-1 and NbOP-2 display relatively high and similar LAS contents of 58 μmol g^{-1} and 51 μmol g^{-1}, respectively (**Table A2**). NbOP-2 has almost no BAS, whereas NbOP-1 possesses a considerable amount of BAS (30 μmol g^{-1}) compared to the other catalysts. The above results indicate that calcination at 700 °C does not significantly enhance the acidity of Nb_2O_5, even after phosphate post-treatment. This is attributed to the fact that Nb_2O_5 at 700 °C forms a well-crystallized orthorhombic T-phase with a dense and highly ordered structure, containing few defects. Consequently, both the Lewis acid sites (LAS) and Brønsted acid sites (BAS) of 700P-Nb_2O_5 remain low. In contrast, 500P-Nb_2O_5 exhibits LAS and Lewis base site (LBS) concentrations nearly identical to those of NbOP-1, measured at 63 μmol g^{-1} and 33 μmol g^{-1}, respectively. Nitrogen physisorption measurements also show nearly identical specific surface areas, suggesting that their acid site densities are similarly comparable. Infrared spectroscopy cannot distinguish significant structural differences between 500P-Nb_2O_5 and NbOP-1. Both catalysts adopt the TT-phase, characterized by a pseudohexagonal structure embedded within orthorhombic superlattices. The TT-phase features a tunnel-like arrangement along the b-axis with a spacing of approximately 4 Å, which facilitates ion diffusion, induces high

strain and dislocation density, and favors defect accommodation. These structural characteristics account for the higher LAS and BAS densities observed in the TT-phase compared to the T-phase.

The acid strength of the catalysts was determined by NH_3-temperature-programmed desorption (NH_3-TPD) analysis. **Figure A5** presents the NH_3-TPD profiles of NbOP-1, NbOP-2, 500P-Nb_2O_5 and 700P-Nb_2O_5. All samples exhibit similar acid strengths, with two desorption peaks at 50–300 °C and 300–550 °C, suggesting that the acid sites across all samples possess similar strength distributions. Compared with NbOP-2 and 700P-Nb_2O_5, which display significantly lower desorption intensities, NbOP-1 and 500P-Nb_2O_5 show notably higher signals, indicative of a higher total acid amount. However, it should be noted that pyridine-adsorbed FTIR results reveal that the densities of Lewis and Brønsted acid sites for NbOP-1 and 500P-Nb_2O_5 are nearly identical. Given the higher sensitivity of NH_3 to weakly bound surface species and non-specific adsorption sites, the slight difference observed in the NH_3-TPD profiles can be attributed to experimental variability or overestimation of low-strength adsorption. Therefore, considering both the FTIR and catalytic performance results, it can be reasonably concluded that NbOP-1 and 500P-Nb_2O_5 possess comparable acid site properties in terms of both strength and quantity, with no substantial difference in their acid functionalities.

Table A2. properties of surface area, Lewis acid amount and Brønsted acid amount measured by BET and FTIR-pyridine adsorption.

Sample	Surface area (m^2 g^{-1})[a]	Lewis acid sites (μmol g^{-1})[b]	Brønsted acid sites (μmol g^{-1})[b]
NbOP-1	53	58	30
NbOP-2	34	51	<10
500P-Nb_2O_5	55	63	33
700P-Nb_2O_5	9	<10	<10

Determined by [a] N_2 adsorption, [b] FTIR-pyridine adsorption

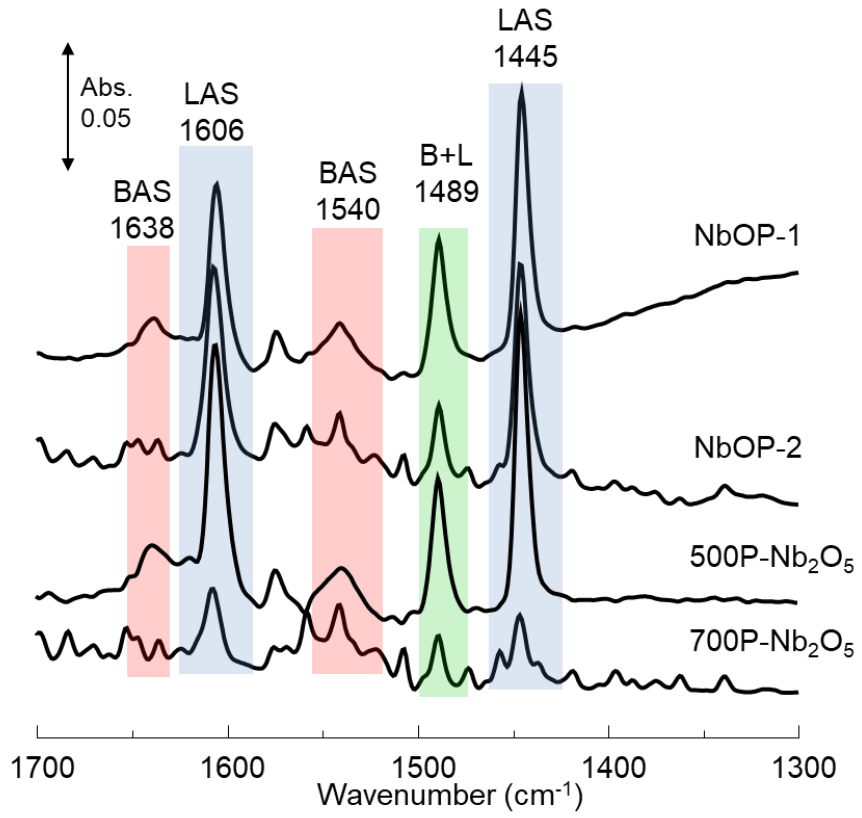

Figure A4. Difference IR spectra adsorbed pyridine molecules on each catalyst at 150 °C.

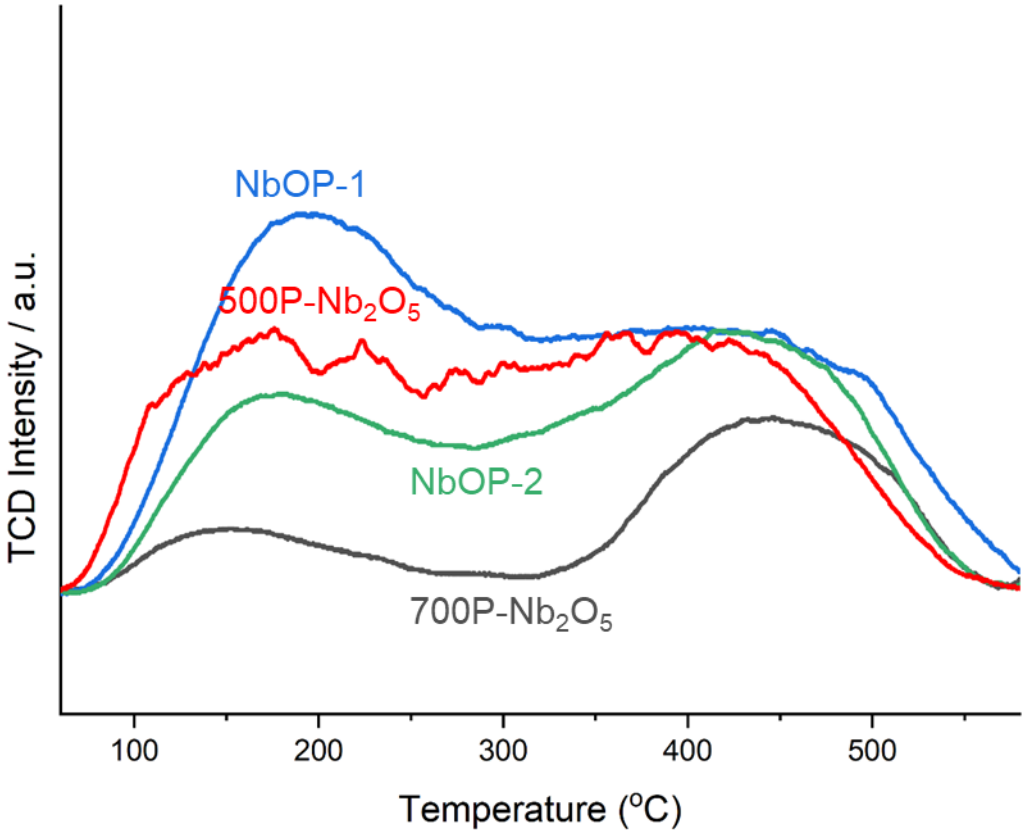

Figure A5. NH_3-TPD of NbOP-1, NbOP-2, 500P-Nb_2O_5 and 700P-Nb_2O_5.

Catalytic performance for furfural production and kinetic study

The conversion of xylose to furfural was conducted in a glass round-bottom reactor containing an aqueous phase and a toluene organic phase. **Figure A6** shows the xylose conversion, furfural yield, and selectivity after a five-hour reaction at 120 °C. Nb_2O_5 calcined at 700 °C exhibits very low catalytic activity, with a conversion rate of only 30%. Even after post-treatment with phosphate modification, no significant improvement was observed. Additionally, when P-Nb_2O_5 was mixed with H_3PO_4 and the amount of solid catalyst was increased to 300 mg, the catalytic performance remained poor. Possible reasons include the formation of a phosphoric acid film on the Nb_2O_5 surface during the reaction, physically blocking reactants from accessing the catalyst's active sites, or competitive adsorption between phosphoric acid and reactants on the Nb_2O_5 surface. Due

to its strong acidity and polarity, phosphoric acid may preferentially adsorb onto the catalyst surface, hindering reactant adsorption and activation, thereby decreasing the reaction rate. Compared to NbOP-2, the furfural yield of NbOP-1 significantly increased from 32% to 50%. FTIR analysis of acid sites revealed that NbOP-2 and NbOP-1 exhibit nearly identical Lewis acid site (LAS) concentrations; however, NbOP-2 possesses almost no Brønsted acid sites (BAS). This demonstrates that the synergistic effect between LAS and BAS contributes to the effective conversion of xylose to furfural. On the other hand, the catalytic performance between NbOP-1 and 500P-Nb_2O_5 shows minimal difference. Based on FTIR and NH_3-TPD characterization, it is difficult to distinguish between the two catalysts, as both exhibit nearly identical acid site densities and acid strength profiles.

To further investigate the differences between the two catalysts, the reaction kinetics of NbOP-1 and 500P-Nb_2O_5 were studied. Figure 4.10(A) presents the time-course curves at 120 °C for both catalysts. The curves show that both catalysts reached a deactivated state within five hours, and extending the reaction time did not significantly improve the conversion rate. The time-course profiles of NbOP-1 and 500P-Nb_2O_5 are nearly identical. Furfural formation and the apparent activation energy were studied in the temperature range of 393–413 K. The reaction was treated as a first-order process, and the reaction rate constant (k) was calculated using the first-order kinetic equation (**Eq. 5**). Based on the experimental data, the reaction rate constants at each temperature were determined, and the apparent activation energies were calculated using the Arrhenius equation (**Eq. 6**). T**able A3** summarizes the apparent activation energies, catalysts, and reaction systems for the conversion of xylose to furfural reported in other studies.[22,42–45] It was found that NbOP-1 exhibited an apparent activation energy of 66.88 kJ mol^{-1}, whereas 500P-Nb_2O_5

exhibited a higher value of 87.66 kJ mol^{-1}. Compared with other catalysts reported in the literature, NbOP-1 appears to offer better catalytic efficiency. Given the very similar catalytic activities of NbOP-1 and 500P-Nb_2O_5 under the studied conditions, altering the reaction parameters, such as increasing the substrate concentration, might be necessary to observe clearer differences. However, since the two catalysts are almost identical in both structure and active site characteristics, their intrinsic catalytic properties are essentially the same, with only minimal differences.

$$\boldsymbol{ln(Cxyl) = -kt + ln(Cxyl0)} \textbf{ (5)}$$

$$\boldsymbol{ln(k) = \frac{-Ea}{R}\left(\frac{1}{T}\right) + ln(A)} \textbf{(6)}$$

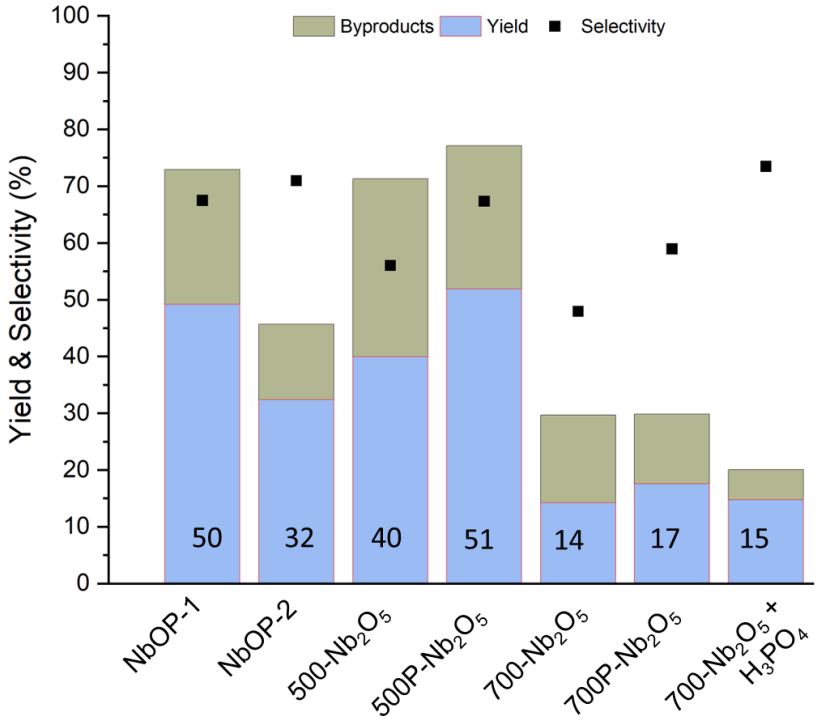

Figure A6. Catalytic performance in the dehydration of xylose to furfural. Reaction conditions: 100 mg of catalyst, 75 mg of xylose, 2 mL of aqueous phase, 8 mL of toluene at 120 °C for 5 hours. 700-Nb_2O_5 + H_3PO_4 is 300 mg solid catalyst amount with 70% mole ratio to xylose

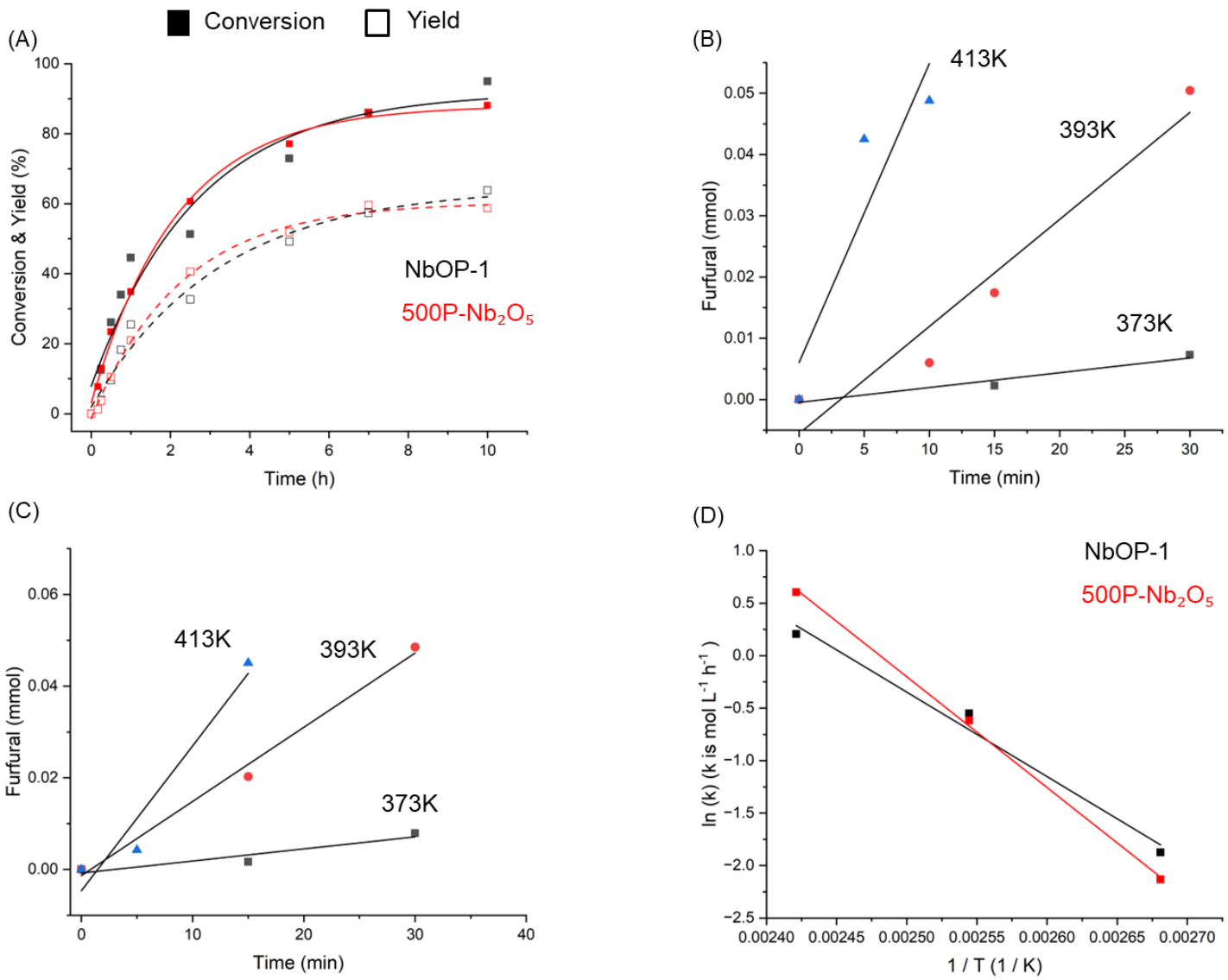

Figure A7. Kinetic study of NbOP-1 and 500P-Nb_2O_5. (A)Time-course result under 120 °C. (B) and (C) are time courses of furfural formation during the initial stage of reaction. (D) Arrhenius plots based on the reaction rate constants.

Table A3. Apparent activation energy barrier comparison of this work in the litterature

Catalyst	Solvent system	Reactor	Ea (kJ mol^{-1})	ref
NbOP-1	Water/Toluene	Batch	66.88	This work
500P-Nb_2O_5	Water/Toluene	Batch	87.66	This work
No cat	High temperature water	Batch	123.27	[42]
$AlCl_3$ + fomic acid	Water	Batch	67.20	[43]
TPA-TiO_2	Water+MIBK	Batch	75.81	[44]
HCl	Water-MIBK	Batch	123.91	[45]
Amorphous Nb_2O_5	Water	Batch	83	[22]

Stability of catalysts

To evaluate the stability of NbOP-1 and 500P-Nb_2O_5, five consecutive reaction cycles were performed, as shown in **Figure A8**. The reactions were conducted under identical conditions: 75 mg of xylose and 300 mg of catalyst in 2 mL of aqueous phase and 8 mL of toluene organic phase at 120 °C. After each cycle, the catalysts were filtered, dried, and calcined at 500 °C before reuse. The results indicated that both the xylose conversion and furfural selectivity for NbOP-1 and 500P-Nb_2O_5 remained stable throughout the cycles, confirming that both catalysts possess good thermal stability and reusability.

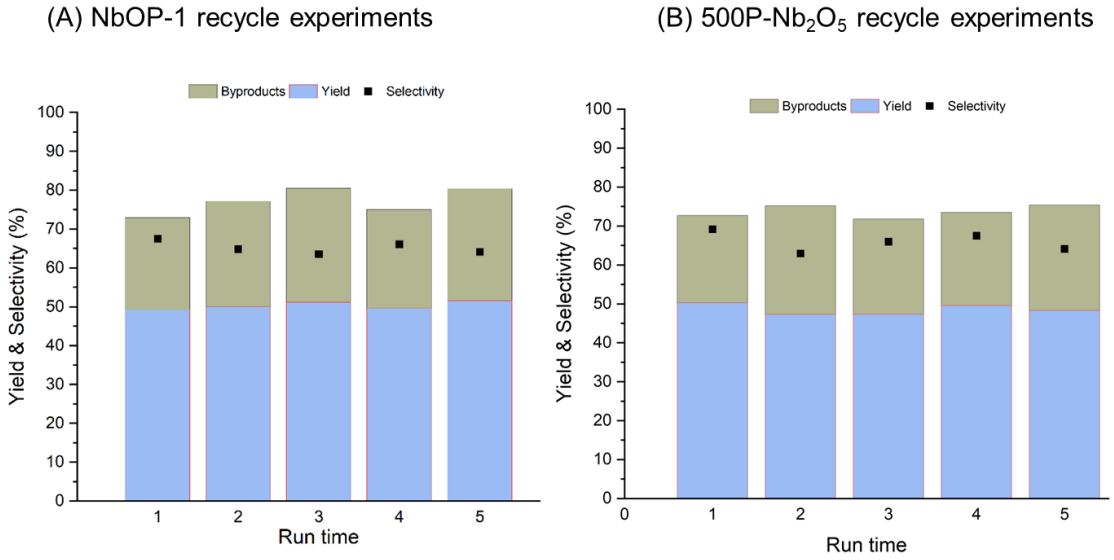

Figure A8. Stability experiments of NbOP-1 and 500P-Nb_2O_5.

Conclusions

In this study, phosphate pre-mixing was employed to modify niobium oxide catalysts, resulting in the stabilization of the TT-phase structure and increased surface acidity compared to conventional phosphate post-treatment. Structural and surface analyses indicated successful incorporation of phosphate molecules and the formation of additional Lewis and Brønsted acid sites. However, despite these modifications, catalytic evaluation showed that the performance of NbOP-1 in xylose dehydration to furfural was largely comparable to that of 500P-Nb_2O_5. Both catalysts demonstrated similar furfural yields, selectivities, and reusability under the tested conditions. Kinetic studies further revealed that, although the apparent activation energies differed, the overall catalytic activities remained similar. These findings highlight that while phosphate pre-mixing improves certain physicochemical properties, it does not lead to a substantial enhancement in catalytic performance, emphasizing the challenge of achieving significant functional improvements through surface modification alone. Furthermore, the comparison between lattice-embedded and surface-anchored phosphate modification approaches revealed

limited improvement in catalytic efficiency. Therefore, future research should focus on more effective modifications of TT-phase Nb_2O_5 aimed at increasing the density of cooperative Lewis–Brønsted acid pair sites to enhance synergistic catalysis.

References

[1] A. J. Ragauskas, C. K. Williams, B. H. Davison, G. Britovsek, J. Cairney, C. A. Eckert, W. J. Frederick, J. P. Hallett, D. J. Leak, C. L. Liotta, J. R. Mielenz, R. Murphy, R. Templer, T. Tschaplinski, *Science* **2006**, *311*, 484–489.

[2] C. M. Cai, T. Zhang, R. Kumar, C. E. Wyman, *J of Chemical Tech & Biotech* **2014**, *89*, 2–10.

[3] F. Cherubini, *Energy Conversion and Management* **2010**, *51*, 1412–1421.

[4] M. Al-Naji, F. Brandi, M. Drieß, F. Rosowski, *Chemie Ingenieur Technik* **2022**, *94*, 1611–1627.

[5] A. Pundir, M. Singh Thakur, S. Prakash, N. Kumari, N. Sharma, Z. He, S. Nam, S. Dhumal, K. Sharma, S. Saxena, S. Kumar, S. V. Deshmukh, M. Kumar, *Heliyon* **2024**, *10*, e35077.

[6] G. Contreras-Zarazúa, M. Martin-Martin, E. Sánchez-Ramirez, J. G. Segovia-Hernández, *Chemical Engineering and Processing - Process Intensification* **2022**, *171*, 108569.

[7] M. J. Da Silva, N. P. G. Lopes, A. A. Rodrigues, *Energies* **2023**, *16*, 1332.

[8] J. A. Dias, E. Caliman, S. C. L. Dias, M. Paulo, A. T. C. P. De Souza, *Catalysis Today* **2003**, *85*, 39–48.

[9] X. Qi, M. Watanabe, T. M. Aida, R. L. Smith, *Catalysis Communications* **2009**, *10*, 1771–1775.

[10] M. Sluban, B. Cojocaru, V. I. Parvulescu, J. Iskra, R. Cerc Korošec, P. Umek, *Journal of Catalysis* **2017**, *346*, 161–169.

[11] I. Agirrezabal-Telleria, A. Larreategui, J. Requies, M. B. Güemez, P. L. Arias, *Bioresource Technology* **2011**, *102*, 7478–7485.

[12] K. Lu, Y. Wang, C. Jin, R. Liao, W. Tan, J. Ye, L. Zhu, S. Wang, *Energy Fuels* **2022**, *36*, 7599–7607.

[13] S.-L. Hu, H. Cheng, R.-Y. Xu, J.-S. Huang, P.-J. Zhang, J.-N. Qin, *Molecular Catalysis* **2023**, *538*, 113009.

[14] K. Skrodczky, M. M. Antunes, X. Han, S. Santangelo, G. Scholz, A. A. Valente, N. Pinna, P. A. Russo, *Commun Chem* **2019**, *2*, 129.

[15] T. Li, F. Krumeich, L. K. Ono, T. Guo, R. Morimoto, C. Ding, Z. Xu, M. Liu, Y. Qi, *Materials Science and Engineering: R: Reports* **2025**, *162*, 100887.

[16] N. Usha, R. Sivakumar, C. Sanjeeviraja, M. Arivanandhan, *Optik - International Journal for Light and Electron Optics* **2015**, *126*, 1945–1950.

[17] R. Sultana, K. Islam, S. Chakraborty, *Trans. Electr. Electron. Mater.* **2024**, DOI 10.1007/s42341-024-00572-x.

[18] H. Liu, S. Wang, J. Ma, Y. Dong, L. Liang, C. Li, Y. Fan, Y. Lei, K. Cao, *Journal of Energy Storage* **2024**, *103*, 114206.

[19] A. P. D. M. Guedes, D. L. R. T. D. Miranda, A. D. Gondim, C. G. Lima Junior, *J. Eng. Exact Sci.* **2024**, *10*, 19766.

[20] F. Huang, T. Jiang, H. Dai, X. Xu, S. Jiang, L. Chen, Z. Fei, P. J. Dyson, *Catal Lett* **2020**, *150*, 2599–2606.

[21] K. Nakajima, Y. Baba, R. Noma, M. Kitano, J. N. Kondo, S. Hayashi, M. Hara, *J. Am. Chem. Soc.* **2011**, *133*, 4224–4227.

[22] N. K. Gupta, A. Fukuoka, K. Nakajima, *ACS Catal.* **2017**, *7*, 2430–2436.

[23] S. M. A. H. Siddiki, Md. N. Rashed, Md. A. Ali, T. Toyao, P. Hirunsit, M. Ehara, K. Shimizu, *ChemCatChem* **2019**, *11*, 383–396.

[24] D. Padovan, K. Endo, T. Matsumoto, T. Yokoi, A. Fukuoka, H. Kato, K. Nakajima, *Small Structures* **2023**, *4*, 2200224.

[25] M. Kim, S. Ronchetti, B. Onida, N. Ichikuni, A. Fukuoka, H. Kato, K. Nakajima, *ChemCatChem* **2020**, *12*, 350–359.

[26] Z. Wang, R. Osuga, K. Endo, D. Padovan, S. Suganuma, A. Fukuoka, H. Kato, K. Nakajima, *Catal. Sci. Technol.* **2025**, 10.1039.D5CY00010F.

[27] N. Alias, Z. Hussain, W. K. Tan, G. Kawamura, A. Matsuda, Z. Lockman, **2024**, DOI 10.2139/ssrn.4976156.

[28] V. Choudhary, S. I. Sandler, D. G. Vlachos, *ACS Catal.* **2012**, *2*, 2022–2028.

[29] K. Wang, C. Liang, Q. Zhang, F. Zhang, *ACS Omega* **2019**, *4*, 1053–1059.

[30] H. Zhang, X. Liu, M. Lu, X. Hu, L. Lu, X. Tian, J. Ji, *Bioresource Technology* **2014**, *169*, 800–803.

[31] W. Guo, T. Kortenbach, W. Qi, E. Hensen, H. Jan Heeres, J. Yue, *Applied Catalysis B: Environmental* **2022**, *301*, 120800.

[32] D. Dey, V. Petrykin, S. Sasaki, M. Kakihana, *J. Ceram. Soc. Japan* **2007**, *115*, 808–812.

[33] M. Kakihana, M. Kobayashi, K. Tomita, V. Petrykin, *Bulletin of the Chemical Society of Japan* **2010**, *83*, 1285–1308.

[34] G. H. M. Gomes, N. D. S. Mohallem, *Materials Letters* **2022**, *318*, 132136.

[35] J. L. Vieira, G. Paul, G. D. Iga, N. M. Cabral, J. M. C. Bueno, C. Bisio, J. M. R. Gallo, *Applied Catalysis A: General* **2021**, *617*, 118099.

[36] G. H. D. M. Gomes, R. R. D. Andrade, N. D. S. Mohallem, *Micron* **2021**, *148*, 103112.

[37] J. C. G. Da Silva, M. D. Vieira, W. D. O. Andrade, A. C. B. D. Santos, *J Mater Sci* **2005**, *40*, 4455–4460.

[38] D. L. Serra, S. J. Hwu, *Acta Crystallogr C Cryst Struct Commun* **1992**, *48*, 733–735.

[39] T. G. Amos, A. W. Sleight, *Journal of Solid State Chemistry* **2001**, *160*, 230–238.

[40] M. Tamura, K. Shimizu, A. Satsuma, *Applied Catalysis A: General* **2012**, *433–434*, 135–145.

[41] M. I. Zaki, M. A. Hasan, F. A. Al-Sagheer, L. Pasupulety, *Colloids and Surfaces A: Physicochemical and Engineering Aspects* **2001**, *190*, 261–274.

[42] Q. Jing, X. Lü, *Chinese Journal of Chemical Engineering* **2007**, *15*, 666–669.

[43] M. Lopes, K. Dussan, J. J. Leahy, *Chemical Engineering Journal* **2017**, *323*, 278–286.

[44] K. Lu, Y. Wang, C. Jin, R. Liao, W. Tan, J. Ye, L. Zhu, S. Wang, *Energy Fuels* **2022**, *36*, 7599–7607.

[45] R. Weingarten, J. Cho, Wm. C. Conner, Jr., G. W. Huber, *Green Chem.* **2010**, *12*, 1423.